

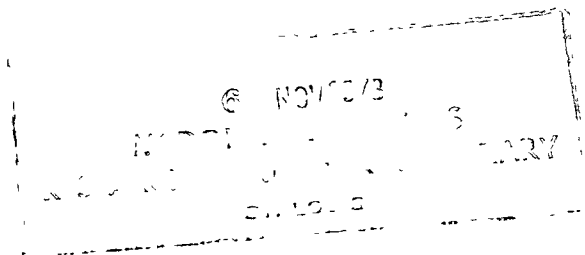
1
NASA Technical Memorandum 58184

100-100000-100000
100-100000-100000

Severe Storm Environments A Skylab EREP Final Report

David E. Pitts, Yoshikazu Sasaki, and J. T. Lee

AUGUST 1978



NASA

M78-18456

NASA Technical Memorandum 58184

Severe Storm Environments A Skylab EREP Final Report

David E. Pitts

Lyndon B. Johnson Space Center, Houston, Texas

Yoshikazu Sasaki

University of Oklahoma, Norman, Oklahoma

J. T. Lee

National Severe Storms Laboratory, Norman, Oklahoma



National Aeronautics
and Space Administration

**Scientific and Technical
Information Office**

1978

CONTENTS

Section	Page
1. SEVERE STORM EXPERIMENT SUMMARY David E. Pitts	1-1
2. DERIVED WATER TEMPERATURES USING S191 and S192 DATA David E. Pitts and W. Johnson	2-1
3. INVERSION OF S191 DATA INTO TEMPERATURE AND WATER VAPOR PROFILES David E. Pitts and A. E. Dillinger	3-1
4. THE VARIATIONAL ANALYSIS OF JUNE 11, 1973, METEOROLOGICAL DATA J. T. Lee and Yoshikazu Sasaki	4-1
5. THE CORRELATION OF SKYLAB L-BAND BRIGHTNESS TEMPERATURES WITH ANTECEDENT PRECIPITATION Marshall J. McFarland	5-1
6. SOIL MOISTURE STUDY USING THE S193 RADIOMETER Bob E. Stucky	6-1
7. S193 SCATTEROMETER CORRELATION WITH SOIL MOISTURE Bob E. Stucky	7-1
8. RECTIFICATION OF A WHOLE-SKY PHOTOGRAPH AS A TOOL FOR DETERMINING SPATIAL POSITIONING OF CUMULUS CLOUDS Bob E. Stucky	8-1
9. SEVERE STORM CLOUD-TOP CHARACTERISTICS David E. Pitts, J. T. Lee, and W. Johnson	9-1
10. REMOTE SENSING OF ATMOSPHERIC WATER VAPOR David E. Pitts, J. T. Lee, and W. Johnson	10-1

1. SEVERE STORM EXPERIMENT SUMMARY

David E. Pitts^a

EXPERIMENT DESCRIPTION

The severe storm environment experiment was designed to measure the effects of the environment on the genesis of severe storms, their maturation, and their properties and also to identify storm cloud characteristics that can determine the future evolution of the storm. The data for this study were derived from the Skylab Earth resources experiments package (EREP), which consisted of the following sensors: multispectral photographic facility (S190A), Earth terrain camera (S190B), infrared spectrometer (S191), multispectral scanner (S192), radiometer/scatterometer and altimeter (S193), and L-band radiometer (S194). The specific data sources were as follows.

1. Photographs from the S190A and S190B cameras were used to map the cloud and land features and to determine the altitude of the clouds. The S190A facility consisted of six high-resolution cameras with matched optical systems to photograph the same scene in six spectral ranges from visible to near infrared. The S190B single-lens Earth terrain camera was designed to obtain photographs of a smaller area as an aid to photointerpretation.

2. Data from the S191 spectrometer were used to determine the spectral properties of cloud and ground targets. The spectrometer consisted of a telescope and plane mirror optical system, a filter-wheel spectrometer, and a boresighted viewfinder tracking system (VTS).

3. The S192 scanner data were used to map, classify, and determine the temperatures of selected cloud features and ground target types. This multispectral scanner collected radiant energy for 13 wavelengths from the visible to the infrared portion of the spectrum.

4. The S193 K-band radiometer/scatterometer data and the S194 L-band radiometer data were used to determine the soil moisture and the effects of clouds on the determination of soil moisture.

The Skylab 2 pass of June 11, 1973, covered the area from the Panhandle of Texas to extreme southeast Texas (groundtrack 48, fig. 1-1) a few hours before a squall line passage. On this pass, S190 and S192 data were collected across a region of known ground truth (the National Severe Storms Laboratory (NSSL) subsynoptic network) where moisture advection was occurring. The S191 data were collected over the target lakes but not over the squall line. No

^aNASA Lyndon B. Johnson Space Center, Houston, Texas.

S192 data were collected over the squall line. However, S193 and S194 data were collected from the Panhandle of Texas, over the squall line, and into the Gulf of Mexico. The S193 was in the alongtrack contiguous mode, which provided replications and therefore good statistical confidence in the analysis. This mode, however, did not allow the calculation of soil moisture maps that the crosstrack contiguous mode would have allowed.

The Skylab 3 pass on August 8, 1973 (groundtrack 34), was parallel to and west of the June 11 pass (fig. 1-1). A mature thunderstorm approximately 190 kilometers south of Beaumont, Texas, was imaged by S190 and S192, but only sporadic S191 data were acquired over the storm. The S194 data were correlated to soil moisture, and the S192 and S191 temperatures were correlated to cloud-top altitude.

During Skylab 4, numerous EREP data were acquired; however, no severe storms were imaged by S190 or S192. Data from two cloud towers were acquired by S191 on December 14 and 15 in Indonesia, but the clouds were not near meteorological stations and were outside the field of view of S190 and S192. The S194 data from all these passes were analyzed, but no significant results were found. The S192 and S191 data for all these passes were perused, and much of the S190 data was cloud contoured to determine the altitude of the clouds. In addition, S190 and S192 data were analyzed over a large area of towering cumulus near Borneo on December 9, 1973. The data acquisitions made for this experiment are detailed in table 1-I.

SIGNIFICANT CONCLUSIONS

Conclusions of the severe storm environment experiment can be summarized as follows:

1. The S194 L-band radiometer is well suited for the remote sensing of synoptic soil moisture over large areas under a wide variety of weather and terrain conditions.
2. The S193 K-band radiometer is well suited for remote sensing of soil moisture at near-nadir look angles but is more sensitive to the deleterious effects of surface roughness, vegetation coverage, and cloud cover.
3. The S193 K-band scatterometer has a high correlation with soil moisture for near-nadir look angles but exhibits no advantage over the passive measurements.
4. Cloud-street orientation may be used in areas lacking radiosonde and surface meteorological observations as an indicator of low-level windflow (ref. 1-1). This may be an important tool for future weather observers on-board Space Shuttle and space station missions.
5. Cirrus clouds cause atmospheric effects on remote sensing of the Earth surface in the visible, near-infrared, and thermal-infrared spectral

regions. At times, these effects dominate both aerosol particulate scattering and gaseous absorption and re-emission effects.

6. Shock-type atmospheric waves observed by the Skylab 4 crew (ref. 1-1) are similar to a phenomenon observed by Mariner 9 in the atmosphere of Mars. Both conditions were caused by high winds flowing over mountain peaks.

7. Sensor data output 21 (SDO 21, 9.7 to 13.0 micrometers) and SDO 11 (1.45 to 1.85 micrometers) are important channels for distinguishing between water-droplet clouds and cirrus clouds. Furthermore, the ratio of SDO 11 to SDO 9 (multiplied by a constant) is even better for separating the two classes of clouds than is SDO 11 alone. Whereas SDO 21 distinguishes between cirrus and liquid-water clouds because they usually occur at different altitudes, SDO 11 and the ratio of SDO 11 to SDO 9 use the inherent physical characteristics of the clouds.

8. The relationship of relief in cloud tops to equivalent black-body temperature was investigated. The use of the S192 thermal band underestimated the high cloud tops, and medium-level clouds (3500 to 7000 meters) were overestimated. This is consistent with what one would expect because atmospheric gaseous absorption makes low clouds appear colder, and the vertical gradient of temperature in the stratosphere is so low as to give large errors in altitude as the result of small errors in the temperature of high clouds.

RECOMMENDATIONS

In the future, mission planning should allow more real-time data acquisition for finding candidate severe storms. Over the United States, it is possible to make a good 8- to 24-hour forecast; however, gathering data in other areas requires real-time support from meteorological satellites and forward viewing and experiment control by the crew.

REFERENCE

1. Pitts, David E.; Lee, J. T.; et al.: Mesoscale Cloud Features Observed From Skylab. Skylab Explores the Earth, NASA SP-380, 1977, pp. 479-501.

TABLE 1-I.- DATA ACQUISITIONS

Skylab mission	EREP pass	Date of acquisition	Area
2	8	June 11, 1973	United States
3	16	Aug. 8, 1973	United States
4	54	Nov. 30, 1973	Brazil
4	55	Dec. 1, 1973	Brazil
4	62	Dec. 7, 1973	Caribbean
4	64	Dec. 9, 1973	Indonesia
4	65	Dec. 14 and 15, 1973	Indonesia
4	71	Jan. 1, 1974	Liberia

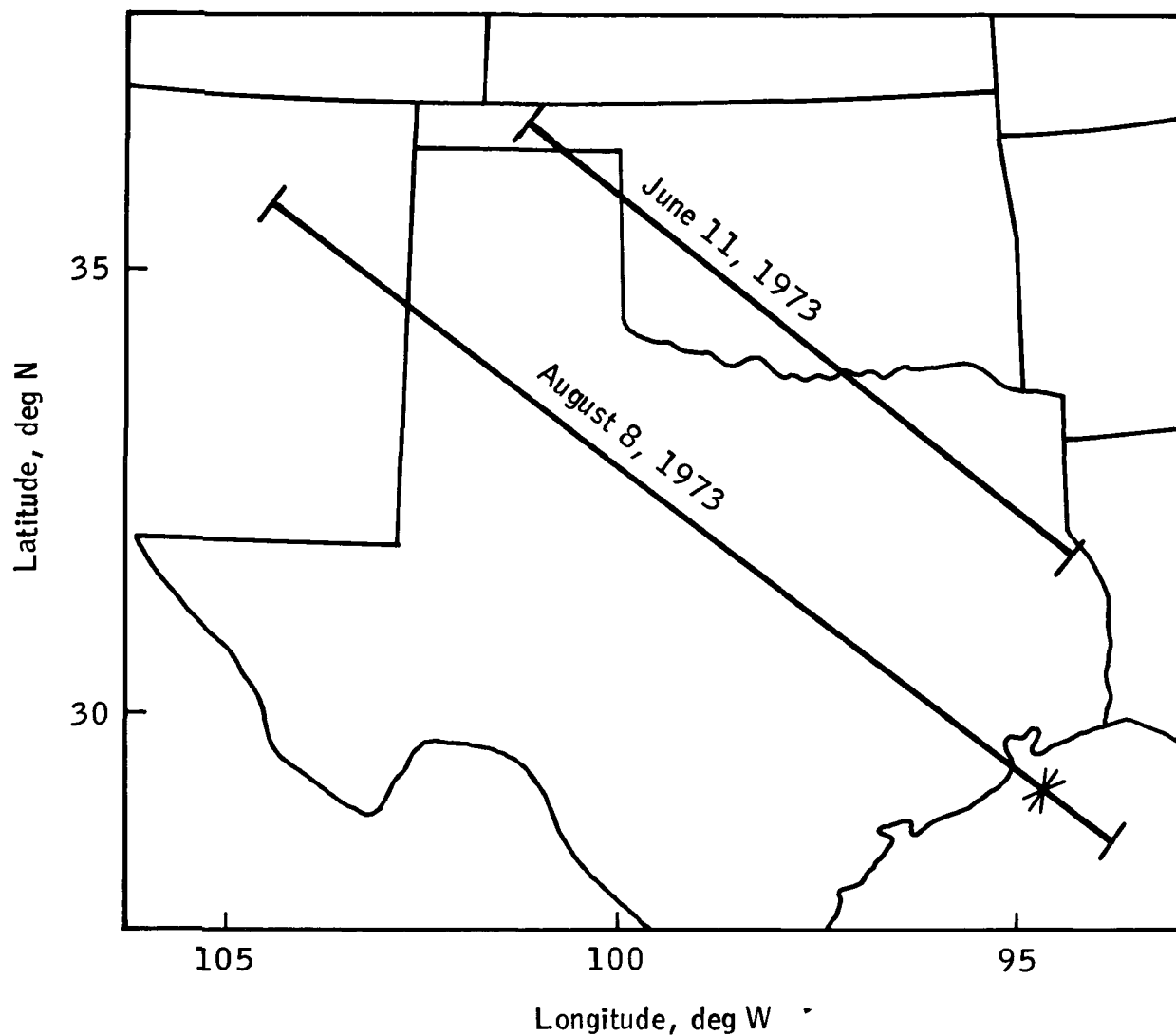


Figure 1-1.- Location of the Skylab groundtracks for the data described in this report. The asterisk in the Gulf of Mexico indicates the location of a severe storm.

2. DERIVED WATER TEMPERATURES USING S191 AND S192 DATA

David E. Pitts^a and W. Johnson^b

DATA ACQUISITION

On June 11, 1973, the Skylab crew gathered data on an Earth resources experiments package (EREP) pass on track 48 over Oklahoma and Texas. As a result of the heatshield problems that occurred during the launch of the orbital workshop (OWS) and the subsequent delayed manning of the vehicle, the groundtrack was approximately 90 kilometers to the west of nominal. Therefore, all the planned primary lake targets (Overholzer, Hefner, Fort Cobb, and Thunderbird) were near the left limits of the S191 spectrometer viewfinder tracking system (VTS) for a descending pass, such as groundtrack 48. Before the pass, it was not obvious whether the primary targets would be identifiable within the crosstrack range of the S191 VTS, so two alternate lakes (Altus and Lawtonka) closer to the groundtrack were added. To check the calibration of the S192 and to verify atmospheric environmental conditions, ground-truth teams were deployed to the primary lake targets, the agricultural test site, and the two alternate lakes. The Skylab 2 crewmembers had flown many T-38 aircraft training missions over the four primary lake targets and therefore were able to recognize these targets at orbital altitude in rapid order with the S191 VTS. When Skylab passed over this area, data on all the primary targets (fig. 2-1) and the agricultural test site were acquired by the pilot, who was the S191 operator. Only Lake Altus was within the scanning swath of the S192 multispectral scanner. On the ground, "bucket" temperatures of the lake waters and other environmental parameters were recorded by the ground-truth teams. The National Severe Storms Laboratory (NSSL) also had its surface and upper air networks in operation. Concurrently, precision radiometric measurements of the water temperatures were made at Lake Overholzer.

RESULTS

Because of evaporative cooling at the top of the water surface, the equivalent black-body temperature is normally less than the bucket temperature. Even though there was a strong breeze from the south on June 11, the equivalent black-body temperature of Lake Overholzer was found to be only 0.5 K cooler than the bucket temperature. Therefore, it is assumed that the bucket temperatures at the other sites can be used as a close approximation to the equivalent black-body temperature.

^aNASA Lyndon B. Johnson Space Center, Houston, Texas.

^bLockheed Electronics Company, Houston, Texas.

The data analysis station was used to prepare a histogram of the S192 thermal channel over a cloud-free area of Lake Altus. The equivalent black-body temperature determined by using the sensor data output (SDO) 21 thermal band was 285 ± 2.3 K compared to the bucket temperature of 297 ± 2 K. The quality assurance¹ performed on the S192 data indicated all bands were of good quality. To understand whether atmospheric absorption and re-emission could cause such a 12-K deficit, the 10:17 a.m. central daylight time (c.d.t.) radi-sonde data (from the NSSL upper air network) from Fort Sill (approximately 90 kilometers east of Lake Altus) were used in the Calfee-Pitts (CP) atmospheric transmission computer program (ref. 2-1). This calculation, using the spectral bandpass for SDO 21 given by Williams (ref. 2-2), showed that 4.5 K of this difference was attributable to atmospheric absorption and re-emission by atmospheric gaseous constituents. However, ubiquitous cirrus was evident to the ground teams, some of which is visible in the S190 photographic images. It is suspected that the majority of the deficit is due to the cirrus, as discussed later in this section.

The cirrus layer also influences the radiances recorded on the other 12 bands of the S192. Studies of energies recorded over water areas with and without cirrus indicate that the albedo differences are quite large, especially in the near-infrared bands. This is shown in figure 2-2, where spectral profiles of a geometric albedo are shown for the Lake Altus data and for a reservoir in New Mexico, from another pass, where no cirrus layer was noted. In the region from 1 to 2.5 micrometers, the albedo of the New Mexico reservoir is near 2.5 percent, whereas the albedo over Lake Altus (with cirrus) is 6 to 8 percent.

The S191 data are plotted in figure 2-3 as a function of time for the period in which the lake targets were acquired. The equivalent black-body temperature for each S191 scan was determined by fitting a Planck function to the S191 radiances over the 10.3- to 13.3-micrometer region, using the technique of Staufferik (ref. 2-3). This technique has previously been used by Pitts et al. (ref. 2-4) in analyzing aircraft spectrometer data. Atmospheric gases were found to absorb and re-emit sufficiently to account for 4.5 K of this difference (fig. 2-4). The gaseous atmospheric effects would be expected to diminish as the zenith angle decreases; however, that is not the case, as seen in figure 2-3.

A special "raw digital tape" of S191 voltages was also acquired and was analyzed by using a computer program (ref. 2-5) that recalibrates the radiances by using the heated and ambient S191 calibration sources. This routine averaged several scans over each target (fig. 2-3), but the results showed that the average was not significantly different from the fit to the individual S191-derived temperatures. Thus, the remainder of the difference between the bucket temperature and the S191-derived temperatures must be attributable to another source. The temperature difference for each target is shown in table 2-I.

¹Work described in the EREP S192 Data Quality Monitoring Report for June 11, 1973 (Rept-159-02-08, Jan. 28, 1975).

Significant cirrus banding over Oklahoma on June 11 could account for the remaining discrepancy. Figure 2-5 shows that the extinction coefficient of ice crystals in the thermal-infrared band has a minimum at approximately 10.0 micrometers. Thus, when cirrus lies between the target and the spacecraft, it will decrease the radiance more at 6.0- and 15.0-micrometer wavelengths than at 10.0 micrometers. This is exactly the type of spectral shape observed for the June 11 data (fig. 2-4). To verify whether the S191 data could be reproduced by adding cirrus to the upwelling radiance predicted by the CP computer model, an extinction curve for the Deirmendjian model (ref. 2-5) was used for a 10-meter-thick layer of ice crystals with 100 particles/cm³. The distribution has a peak at 5 micrometers, which is small for ice crystals. Figure 2-4 shows that this causes slightly more absorption than was observed but does illustrate that cirrus can be the cause of such an effect.

A backup check of the procedures was performed when an S191 data set for Monroe Reservoir near Bloomington, Indiana, was compared with predictions from the CP program and with the Anding atmospheric transmission computer program² (fig. 2-6). At the 11-micrometer wavelength, the CP radiance was approximately 2 K higher than the Anding and S191 radiances. At 13 micrometers, the CP radiance was higher and the Anding radiance lower than the S191 radiance, the maximum temperature difference being about 5 K. This comparison shows that the CP may be slightly high and indicates that on June 11 some of the 10-K temperature difference observed at 13 micrometers was due to the cirrus clouds.

Off-band radiation could also be important in contributing to an error (ref. 2-6) but would be of opposite sign to the observed effect. Kenney (ref. 2-7) indicated that the S191 instrument was operating well on June 11 and that alinement error was 0.1 milliradian forward and 0.55 milliradian³ left, which would give an absolute error of approximately 0.24 kilometer or approximately half the field of view of the S191 spectrometer. He points out that sizable errors were evident in the S191 system because of (1) unknown dichroic temperature, (2) unknown VTS mirror temperatures, and (3) off-band radiation. In addition, the authors have become aware that during a recent inspection of the S191 backup unit, which is being used on a helicopter to support the large-area crop inventory experiment (LACIE), the dichroics were found to be delaminating. Whether any of these errors could have resulted from delamination of the flight unit is subject to debate.

In summary, there is evidence that the cirrus clouds in the June 11 EREP data had a significant effect on both the S191 and S192 visible and infrared data. For S191 data, the cirrus clouds appear to cause a 4- to 10-K decrease in equivalent black-body temperature for wavelengths from 10.3 to

²Private communication, David Anding, Science Associates, Inc., Ann Arbor, Michigan, 1973.

³No crosstrack alinement error was measured for Skylab 2; this value is for Skylab 3.

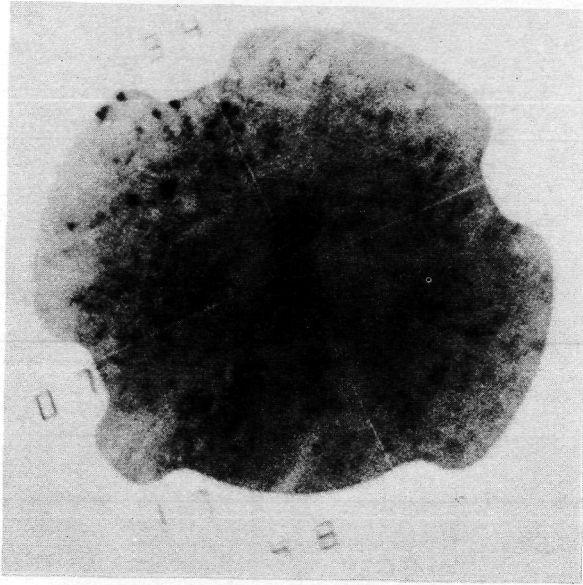
13 micrometers. A secondary observation is also apparent. Within the relatively small view of a satellite sensor, the error variability is approximately 7 K. This emphasizes that the variability of the absorbing medium is so great that no amount of radiosonde observation could predict it accurately. Even ground-operated sensors would be of limited value in defining the four-dimensional variability of the cirrus layers, except in a highly instrumented experimental situation.

REFERENCES

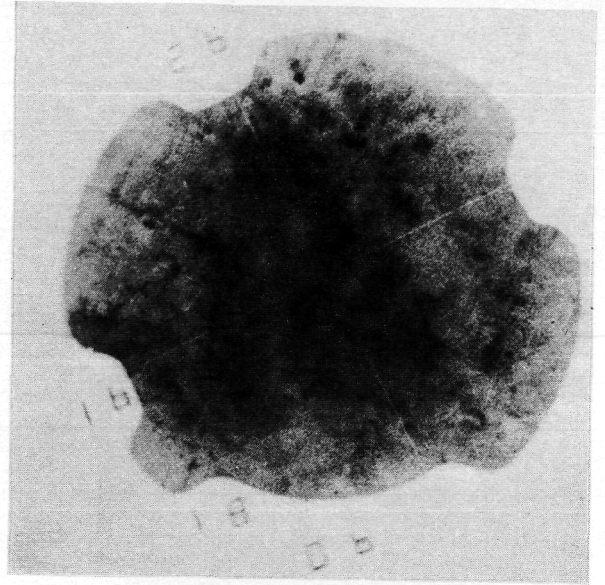
- 2-1. Pitts, D. E.; Barnett, T. L.; et al.: Atmospheric Transmission Computer Program CP. NASA TM X-58137, 1974.
- 2-2. Williams, C. K.: Sensor Performance Report, Volume III (S192) - Engineering Baseline and SL2 Evaluation. NASA CR-141446, 1973.
- 2-3. Staufurik, J. W.: An Algorithm To Aid in Determining Target Temperature From Filter-Wheel Spectrometer Data. LEC/HASD Tech. Rep. 649D.21018, Lockheed Electronics Co., 1970.
- 2-4. Pitts, David E.; Reeser, Warner K.; and Mendlowitz, Maury A.: Equivalent Blackbody Temperature of the Top of a Severe Storm. J. Appl. Meteorol., vol. 14, no. 4, June 1975, pp. 609-618.
- 2-5. Deirmendjian, D.: Electromagnetic Scattering of Spherical Polydispersions. Elsevier, 1969, pp. 77-83.
- 2-6. Hughes, C. L.: S191 Sensor Performance Evaluation Report. LEC-5778, Lockheed Electronics Co., 1975.
- 2-7. Kenney, Gerald P.: Skylab Program Earth Resources Experiment Package Sensor Performance Evaluation Final Report, Volume II (S191). NASA CR-141735, 1975.

TABLE 2-1.- DIFFERENCE BETWEEN BUCKET AND S191 TEMPERATURES

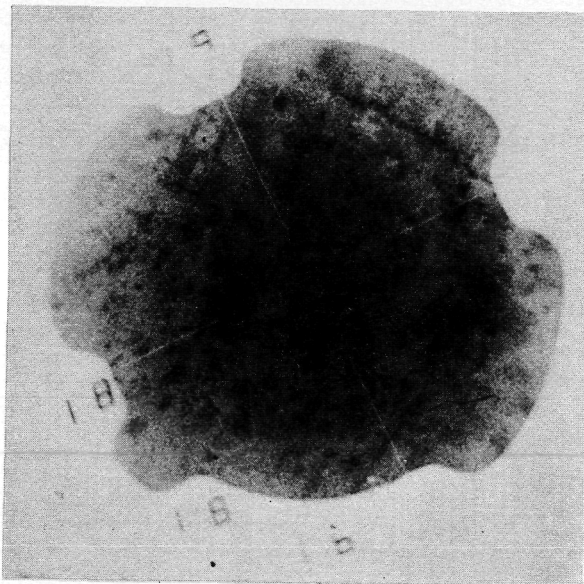
Target	Temperature difference, K
Fort Cobb Reservoir	6
Lake Overholzer	5
Lake Hefner	10.5
Lake Thunderbird	12
Agricultural fields	8



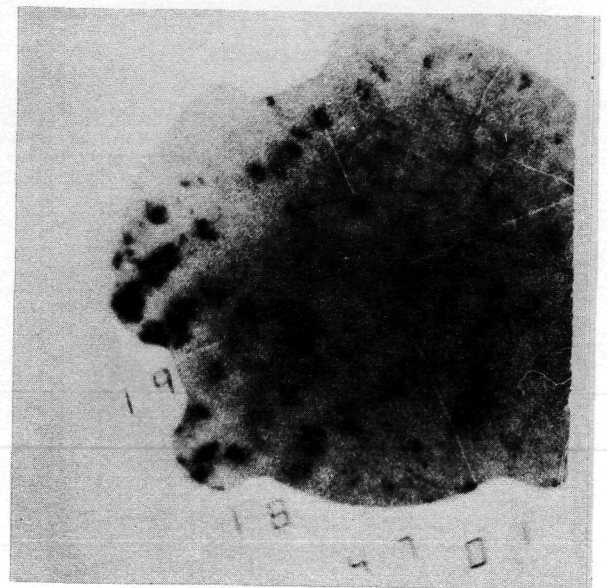
(a) Fort Cobb Reservoir.



(b) Lake Overholzer.



(c) Lake Hefner.



(d) Lake Thunderbird.

Figure 2-1.- Photographs of the four target lakes made using the S191 VTS.

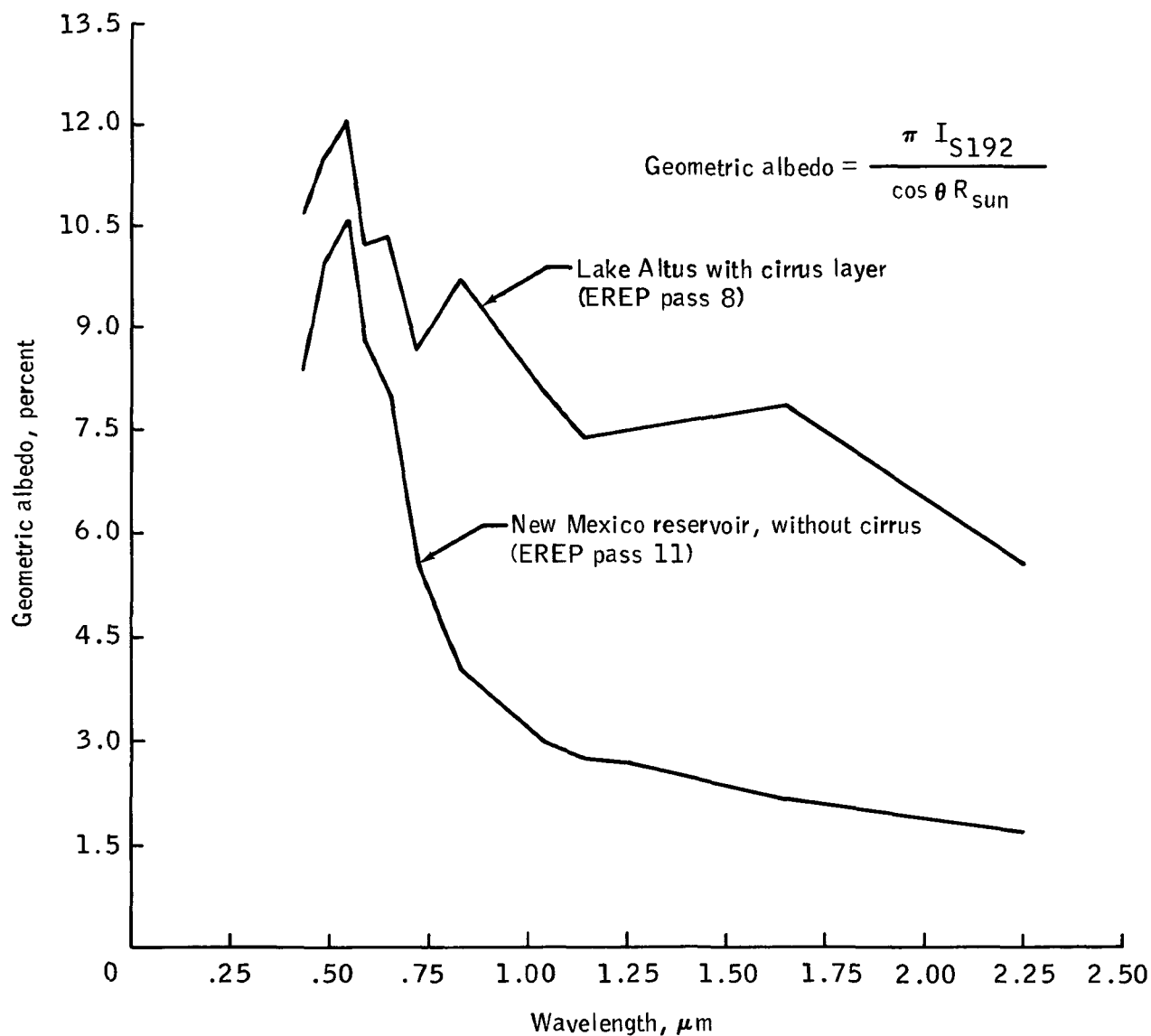


Figure 2-2.- Skylab S192 spectral profiles of Lake Altus, Oklahoma, and a deepwater reservoir near White Sands, New Mexico. In the formula for geometric albedo, I_{S192} is the intensity from a Skylab S192 band in $W/(cm^2 \cdot \mu m \cdot sr)$, θ is the solar zenith angle, and R_{sun} is the intensity from the Sun in $W/(cm^2 \cdot \mu m \cdot sr)$.

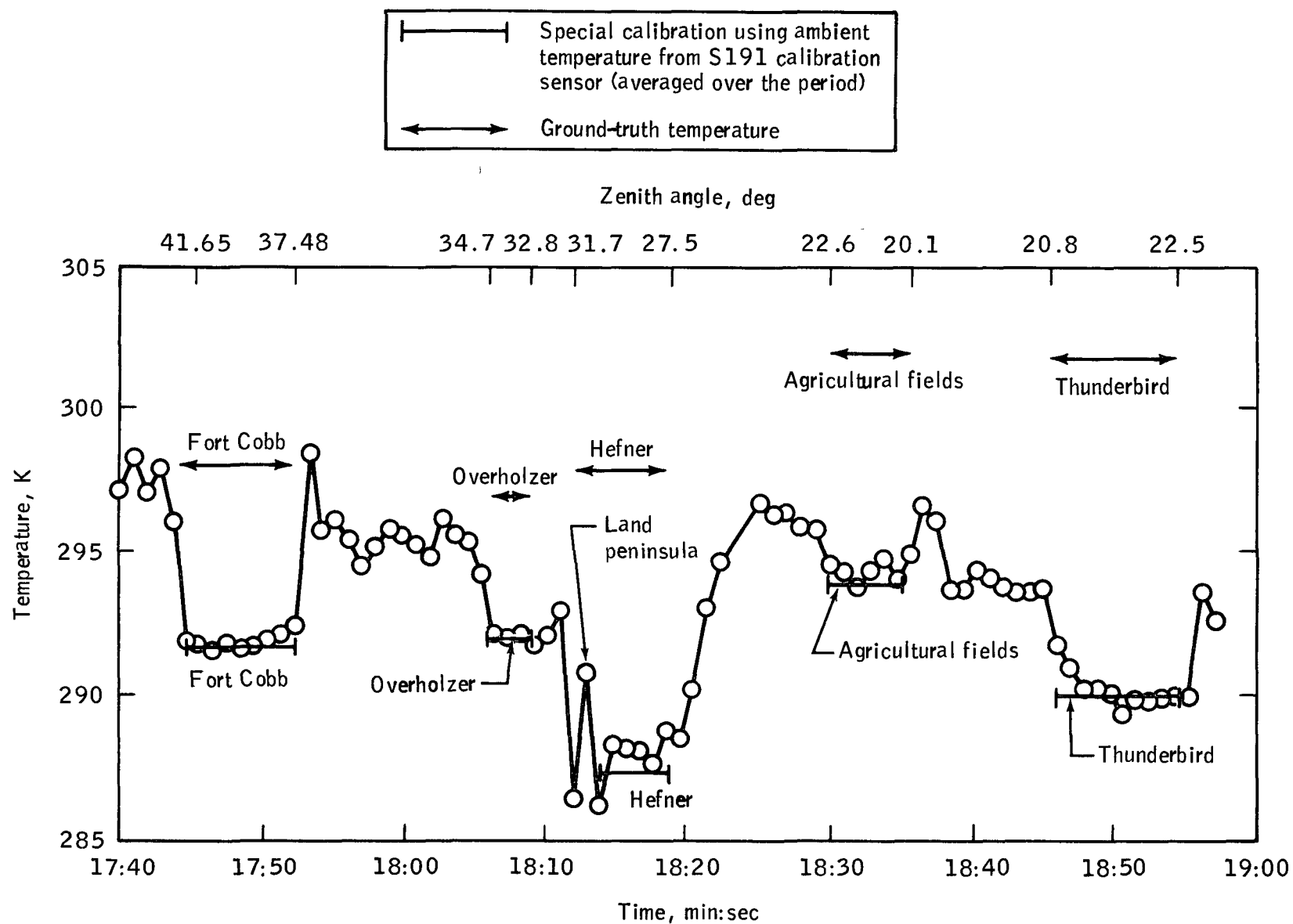


Figure 2-3.- Albedo data from S191 plotted as a function of time.

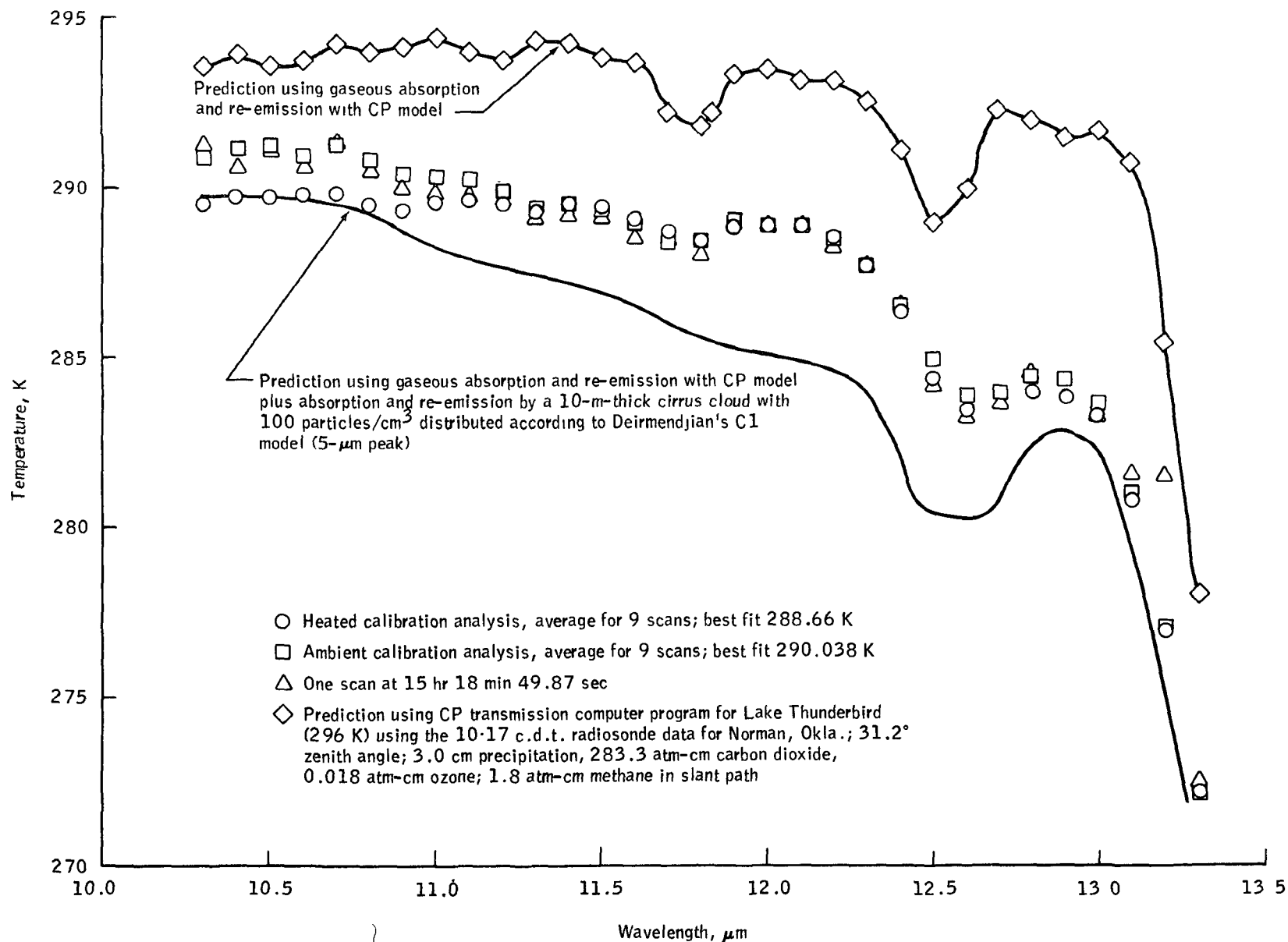


Figure 2-4.- Data from S191 compared to prediction for June 11, 1973, over Lake Thunderbird.

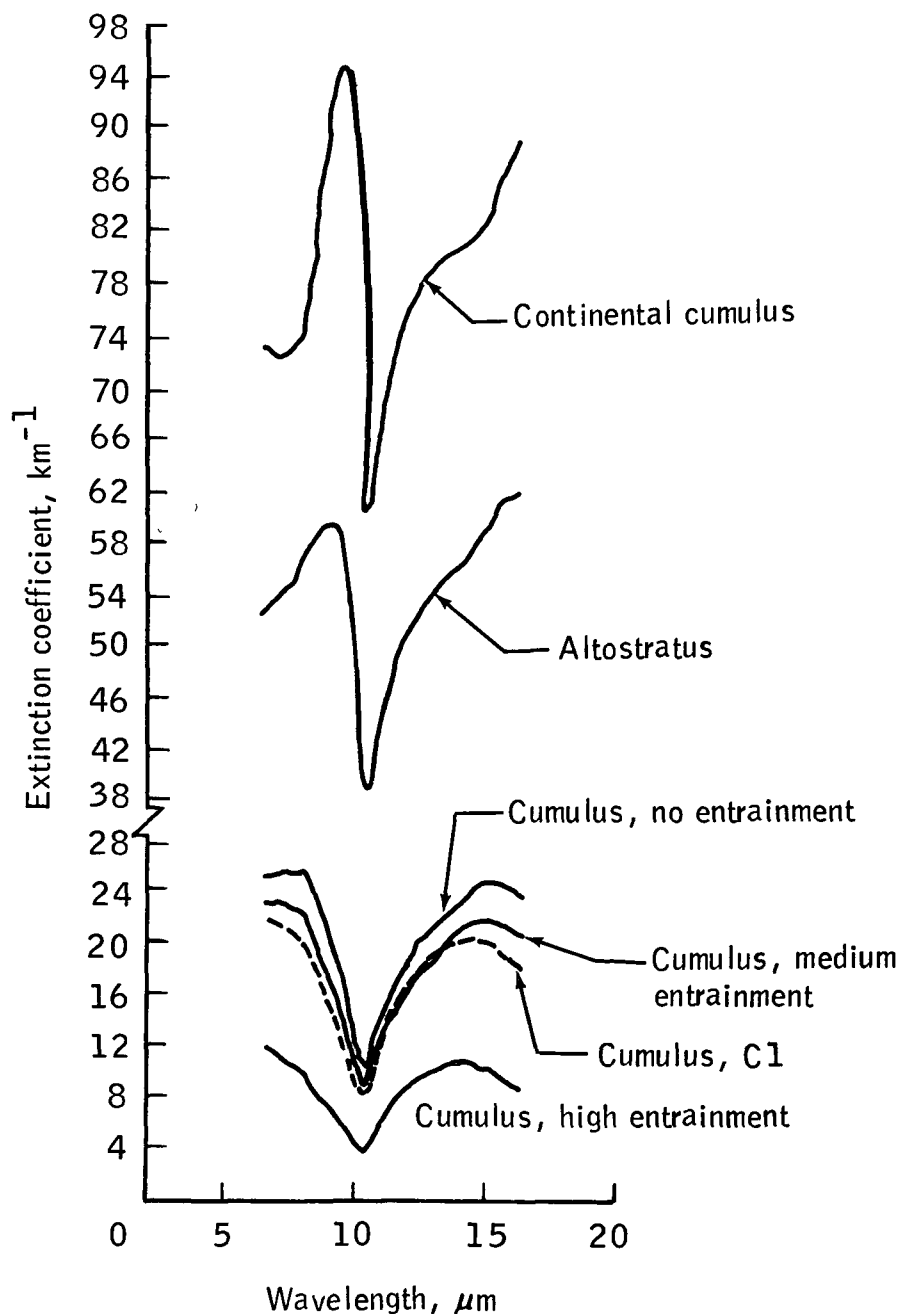


Figure 2-5.- A comparison of the spectral extinction coefficients for several log-normal distributions of ice spheres and Deirmendjian's C1 cloud model (ref. 2-5). All distributions are normalized for 100 particles/ cm^3 . Details on computation of the extinction coefficient and the origin of the various curves shown are given in reference 2-4.

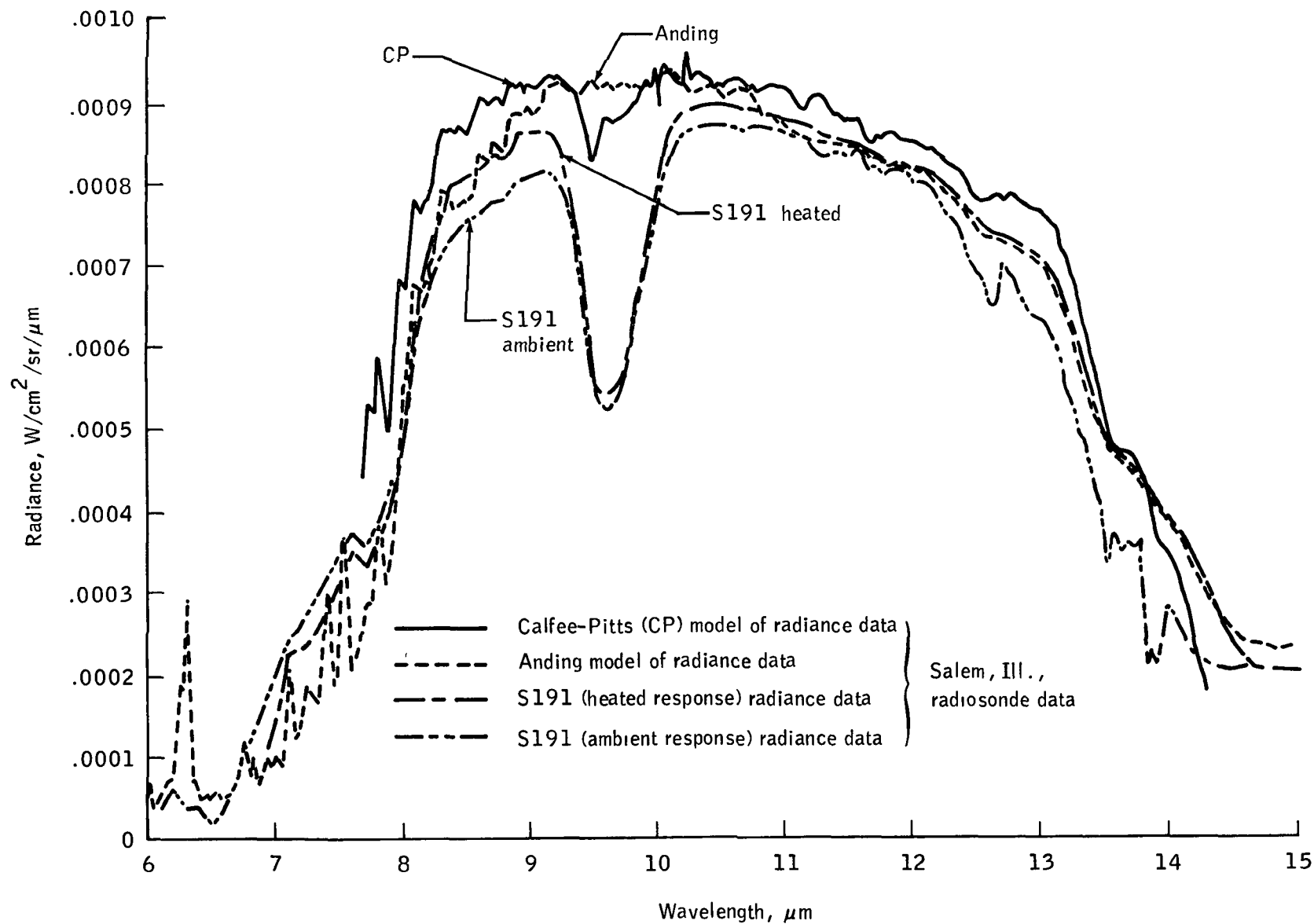


Figure 2-6.- Comparison of S191 radiance data on Monroe Reservoir and radiance predictions by the Calfee-Pitts and Anding atmospheric models.

3. INVERSION OF S191 DATA INTO TEMPERATURE

AND WATER VAPOR PROFILES

David E. Pitts^a and A. E. Dillinger^b

On June 11, 1973, the Skylab viewfinder tracking system (VTS) operator acquired five targets (the four primary target lakes and the agricultural test site) to verify the S191 infrared spectrometer calibration (as determined in the previous section) and to determine whether temperature and water profiles can be measured at mesoscale distances by remote methods. As shown in section 2, each of the targets was acquired for several seconds, thus allowing the radiances to be averaged to reduce system noise. The Backus-Gilbert inversion scheme (ref. 3-1) was used with weighting functions computed by an arbitrary temperature and water vapor profile that was provided before the Skylab launch by Westwater and Strand.

The atmosphere from the surface to 40 kilopascals (400 millibars) was well known because a radiosonde was launched within 100 kilometers and a few minutes of all the target acquisitions. Inversions were attempted using the 669, 678, 687, 696, 705, 714, 723, 741, and 750 cm^{-1} bands of S191. Actual target equivalent black-body temperature from ground truth was used for the surface conditions input to the program. The profile obtained for Fort Cobb is shown in figure 3-1. When the program was run, it was necessary to impose certain physical constraints on the profiles: (1) temperature gradients must be smaller than superadiabatic and (2) supersaturation cannot occur. Both conditions occurred between 80 and 50 kilopascals (800 and 500 millibars) in the uncorrected profiles. In the predicted profiles, the surface predictions of both water vapor and temperature appear reasonable; however, above the surface, a temperature inversion is predicted that did not occur. Above 50 kilopascals (500 millibars), the predicted temperature is higher than the actual temperature by 10 K or more. Temperature profiles and water vapor profiles for other targets exhibited the same difficulties.

Parametric studies indicated that incorrect viewing angles or incorrect surface temperatures would not, by themselves, cause these errors. The problem is evidently either instrument related or caused by the cirrus reducing the intensity received by the S191. The latter factor can explain the 7- to 8- and the 13- to 14-micrometer regions as shown in figure 3-2. However, from 14 to 15 micrometers (not discussed in the previous section), it appears as if the off-band radiance were contributing to a higher stratospheric temperature. Therefore, even if the instrument had been working perfectly, the cirrus would

^aNASA Lyndon B. Johnson Space Center, Houston, Texas.

^bLockheed Electronics Company, Houston, Texas.

have caused some difficulty with the temperature profile and would have caused major problems with the inversion of the water vapor profile.

REFERENCE

- 3-1. Westwater, E. R.; and Strand, O. N.: A Generalized Inversion Program: Internal Equations and Iterative Solutions. NOAA Environmental Research Laboratory 309-WPL 34, COM-75-50159/3, 1974.

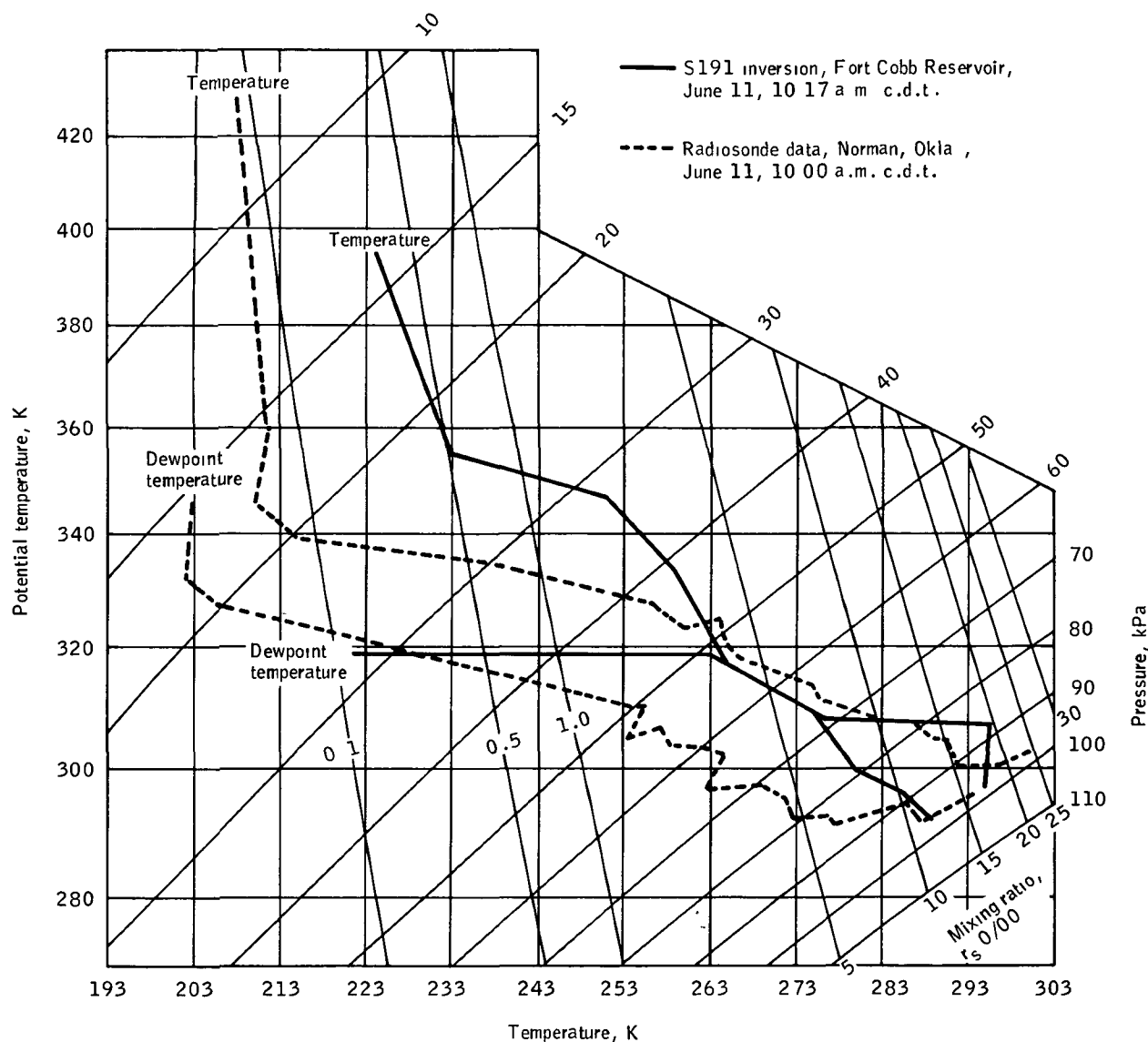


Figure 3-1.- Fort Cobb Reservoir temperature and water vapor profiles from S191. The profiles used in the weighting functions and the actual profile were determined by a nearby radiosonde.

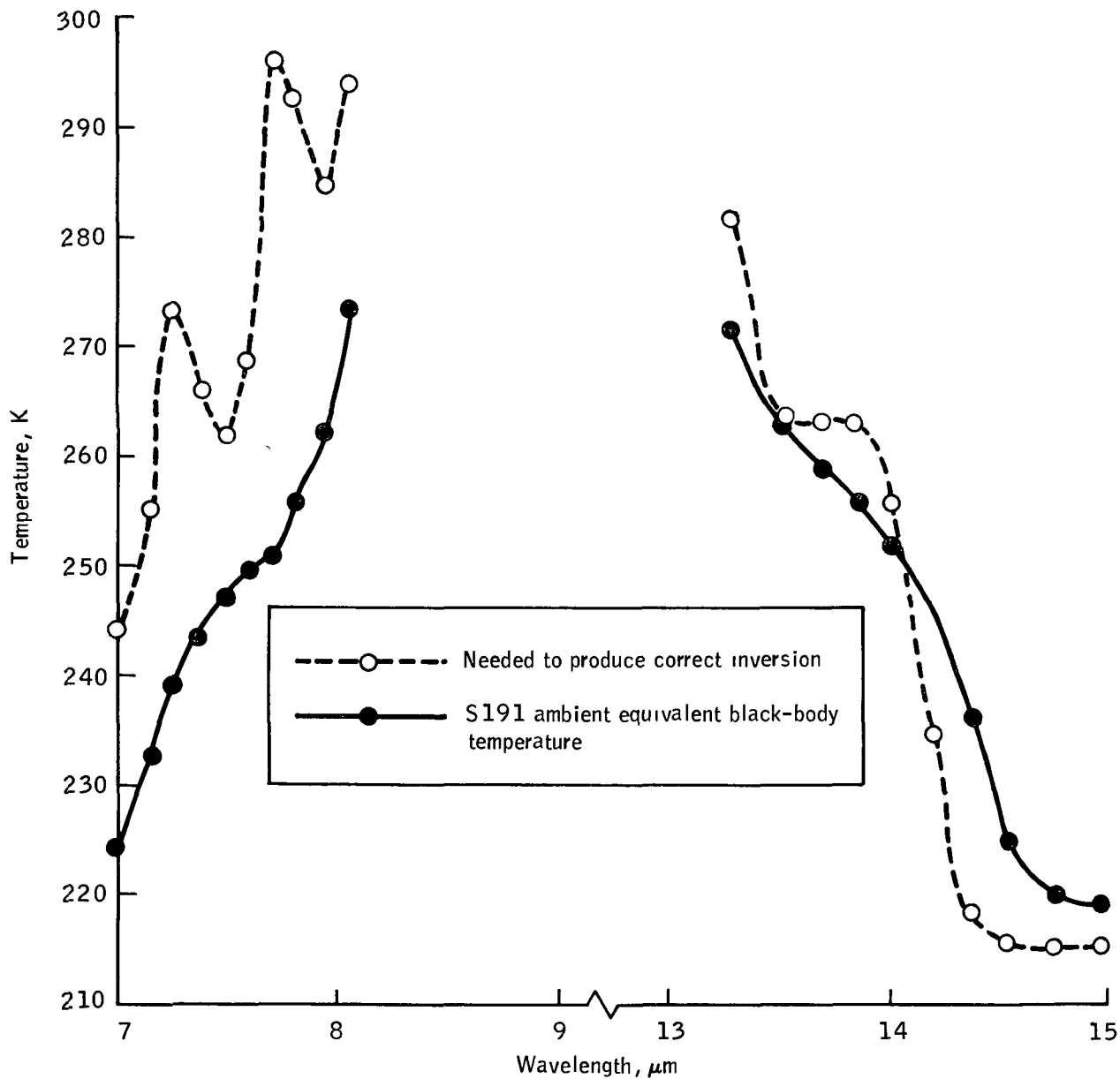


Figure 3-2.- Skylab S191 radiance data for Fort Cobb Reservoir and the S191 radiance needed to produce the correct temperature and water profiles.

4. THE VARIATIONAL ANALYSIS OF JUNE 11, 1973, METEOROLOGICAL DATA

By J. T. Lee^a and Yoshikazu Sasaki^b

VARIATIONAL FILTER

The assigned fields of temperature, dewpoint, pressure, and horizontal wind components require additional filtering to suppress nonresolvable spatial and temporal frequencies. The major requirement for filtering arises from the noise or error contained in the observed data and from the method of initializing the data fields on the computational grid, which has a grid spacing of 63.5 kilometers horizontally and 1 hour temporally. Because the average station spacing (excluding the National Severe Storms Laboratory (NSSL) mesoscale network) is near 200 kilometers, the minimum resolvable wavelength is 400 kilometers or 6Δs, under optimal conditions. In time, observations are available once each hour, so that waves with a period less than 2 hours are not resolvable. Consequently, any information less than six horizontal grid units and two time units should be suppressed.

A filter based on Sasaki's variational analysis technique (refs. 4-1 to 4-4) is used because the filter characteristics may be specified individually in the horizontal and temporal directions and applied simultaneously. The filtering functional is

$$J = \iiint_{x y t} \left\{ \tilde{\alpha} (\phi - \tilde{\phi})^2 + \alpha_s \left[\left(\frac{\partial \phi}{\partial x} \right)^2 + \left(\frac{\partial \phi}{\partial y} \right)^2 \right] + \alpha_t \left[\left(\frac{\partial \phi}{\partial t} \right)^2 \right] + \beta_s \left[\left(\frac{\partial^2 \phi}{\partial x^2} \right)^2 + \left(\frac{\partial^2 \phi}{\partial y^2} \right)^2 \right] + \beta_t \left[\left(\frac{\partial^2 \phi}{\partial t^2} \right)^2 \right] \right\} dt dx dy \quad (4-1)$$

where J is the functional; $\tilde{\alpha}$, α_s , α_t , β_s , β_t are the specified weak constraint weights; and ϕ is any observed or calculated quantity. The first term is the universal requirement for minimizing the difference between the analyzed and observed values. The second and third terms suppress the amplitudes in the higher frequencies in the analysis. The last two terms provide additional constraints on the "curvature" of the analyzed fields. As shown by

^aNational Severe Storms Laboratory, Norman, Okla.

^bUniversity of Oklahoma, Norman, Okla.

Wagner (ref. 4-4), the addition of the second derivative constraints will result in a more rapid decrease in the response function for high frequencies than with first derivative constraints alone. Recently, Sasaki has shown that an n th order derivative low-pass filter allows continuity of all derivatives up to the $2n$ th order derivative except the $(2n - 1)$ th order derivative. These results were derived for the case in which the analysis equations were applied to sparse observed data fields. An equivalent situation exists when the observed data fields contain discontinuities although covering the entire computational grid. These results imply that quantities derived from the analyzed fields (for example, vorticity and divergence) may be discontinuous if only first derivative constraints are placed on the analysis while second derivative constraints yield continuous first, second, and fourth derivatives, but not continuous third derivatives.

The first variation of equation (4-1), represented by δ , when equated to zero, gives the Euler-Lagrange or analysis equation

$$\tilde{\alpha}(\phi - \tilde{\phi}) - \alpha_s \left[\frac{\partial^2 \phi}{\partial x^2} + \frac{\partial^2 \phi}{\partial y^2} \right] - \alpha_t \left[\frac{\partial^2 \phi}{\partial t^2} \right] + \beta_s \left[\frac{\partial^4 \phi}{\partial x^4} + \frac{\partial^4 \phi}{\partial y^4} \right] + \beta_t \left[\frac{\partial^4 \phi}{\partial t^4} \right] = 0 \quad (4-2)$$

plus the boundary conditions

$$\int_x \int_y \left[\left(\alpha_t \frac{\partial \phi}{\partial t} - \beta_t \frac{\partial^3 \phi}{\partial t^3} \right) \delta \phi + \beta_t \frac{\partial^2 \phi}{\partial t^2} \frac{\partial \delta \phi}{\partial t} \right]_{t_1}^{t_2} dy dx = 0 \quad (4-3)$$

and

$$\int_x \int_t \left[\left(\alpha_s \frac{\partial \phi}{\partial y} - \beta_s \frac{\partial^3 \phi}{\partial y^3} \right) \delta \phi + \beta_s \frac{\partial^2 \phi}{\partial y^2} \frac{\partial \delta \phi}{\partial y} \right]_{y_1}^{y_2} dt dx = 0 \quad (4-4)$$

and

$$\int_y \int_t \left[\left(\alpha_s \frac{\partial \phi}{\partial x} - \beta_s \frac{\partial^3 \phi}{\partial x^3} \right) \delta \phi + \beta_s \frac{\partial^2 \phi}{\partial x^2} \frac{\partial \delta \phi}{\partial x} \right]_{x_1}^{x_2} dt dy = 0 \quad (4-5)$$

For the results of this case study, the values of the quantity were specified on the x_1 , x_2 , y_1 , y_2 , and t_1 boundaries, i.e., $\delta\phi = 0$; at the t_2 boundary, the natural boundary conditions were imposed, i.e.,

$$\alpha \frac{\partial \phi}{s \partial t} - \beta \frac{\partial^3 \phi}{t \partial t^3} = 0 \quad (4-6)$$

and

$$\beta \frac{\partial^2 \phi}{t \partial t^2} = 0 \quad (4-7)$$

To investigate the filtering characteristic, the continuous differential operators in equation (4-2) are replaced by centered-space/time finite difference operators. Equation (4-2) becomes

$$\tilde{\alpha}(\phi - \tilde{\phi}) - \frac{\alpha_s}{\Delta s^2} \left(\Delta_x^2 \phi + \Delta_y^2 \phi \right) - \frac{\alpha_t}{\Delta t^2} \Delta_t^2 \phi + \frac{\beta_s}{\Delta s^4} \left(\Delta_x^4 \phi + \Delta_y^4 \phi \right) + \frac{\beta_t}{\Delta t^4} \Delta_t^4 \phi = 0 \quad (4-8)$$

where $\Delta s = \Delta x = \Delta y$ is the horizontal grid spacing and Δt is the temporal grid spacing. The difference operators are of the form

$$\Delta_x^2 \phi = \phi(i+1, j, k) + \phi(i-1, j, k) - 2\phi(i, j, k) \quad (4-9)$$

and

$$\begin{aligned} \Delta_x^4 \phi = & \phi(i+2, j, k) + \phi(i-2, j, k) \\ & - 4[\phi(i+1, j, k) + \phi(i-1, j, k)] + 6\phi(i, j, k) \end{aligned} \quad (4-10)$$

The i , j , k are grid indices in the x , y , and t directions, respectively. Similar operators exist for the y and t derivatives.

Equation (4-8) can be made nondimensional by letting the weak constraint weights be a product of a scale factor and a nondimensional weight, for example, $\alpha = \alpha_s^* \alpha'_s$. The scale factors are defined as

$$\alpha_s^* = \Delta s^2$$

$$\alpha_t^* = \Delta t^2$$

$$\beta_t^* = \Delta t^4$$

$$\beta_s^* = \Delta s^4$$

With these definitions, equation (4-8) is rewritten in nondimensional form, dropping the primes

$$\tilde{\alpha}(\phi - \tilde{\phi}) - \alpha_s \left(\Delta_x^2 \phi + \Delta_y^2 \phi \right) - \alpha_t \Delta_t^2 \phi + \beta_s \left(\Delta_x^4 \phi + \Delta_y^4 \phi \right) + \beta_t \Delta_t^4 \phi = 0 \quad (4-11)$$

The analytical response function, which is defined as the ratio of the analyzed wave amplitude to the initial or observed wave amplitude, is determined by assuming that ϕ and $\tilde{\phi}$ have the analytic form

$$\begin{bmatrix} \tilde{\phi} \\ \phi \end{bmatrix} = \begin{bmatrix} \tilde{A} \\ A \end{bmatrix} e^{i(kr\Delta x + ms\Delta y + np\Delta t)} \quad (4-12)$$

where r , s , and p are integers, $k = \frac{2\pi}{L_x}$, $m = \frac{2\pi}{L_y}$, and $n = \frac{2\pi}{L_t}$ are wave-numbers in the x , y , and t directions, respectively. Substituting equation (4-12) into equation (4-11) and simplifying, one obtains

$$\begin{aligned} & \tilde{\alpha}(A - \tilde{A}) - A\alpha_s \left(e^{ik\Delta x} + e^{-ik\Delta x} - 2 + e^{im\Delta y} + e^{-im\Delta y} - 2 \right) \\ & - A\alpha_t \left(e^{in\Delta t} + e^{-in\Delta t} - 2 \right) \\ & + A\beta_s \left[e^{i2k\Delta x} + e^{-i2k\Delta x} - 4 \left(e^{ik\Delta x} + e^{-ik\Delta x} \right) + 6 \right. \\ & \quad \left. + e^{i2m\Delta y} + e^{-i2m\Delta y} - 4 \left(e^{im\Delta y} + e^{-im\Delta y} \right) + 6 \right] \\ & + A\beta_t \left[e^{i2n\Delta t} + e^{-i2n\Delta t} - 4 \left(e^{in\Delta t} + e^{-in\Delta t} \right) + 6 \right] = 0 \end{aligned} \quad (4-13)$$

Use of the standard trigonometric identities produces

$$\begin{aligned} & \tilde{\alpha}(A - \tilde{A}) + 4A\alpha_s \left[\sin^2 \left(\frac{k \Delta x}{2} \right) + \sin^2 \left(\frac{m \Delta y}{2} \right) \right] + 4A\alpha_t \left[\sin^2 \left(\frac{n \Delta t}{2} \right) \right] \\ & + 4A\beta_s \left\{ \left[4 \sin^2 \left(\frac{k \Delta x}{2} \right) - \sin^2 (k \Delta x) \right] + \left[4 \sin^2 \left(\frac{m \Delta y}{2} \right) - \sin^2 (m \Delta y) \right] \right\} \\ & + 4A\beta_t \left[4 \sin^2 \left(\frac{n \Delta t}{2} \right) - \sin^2 (n \Delta t) \right] = 0 \end{aligned} \quad (4-14)$$

Thus, the response function R for equation (4-8) is

$$R = \frac{\tilde{\alpha}}{\left\{ \tilde{\alpha} + (4\alpha_s + 16\beta_s) \left[\sin^2 \left(\frac{\pi}{e} \right) + \sin^2 \left(\frac{\pi}{f} \right) \right] + (4\alpha_t + 16\beta_t) \sin^2 \left(\frac{\pi}{g} \right) - 4\beta_s \left[\sin^2 \left(\frac{2\pi}{e} \right) + \sin^2 \left(\frac{2\pi}{f} \right) \right] - 4\beta_t \sin^2 \left(\frac{2\pi}{g} \right) \right\}} \quad (4-15)$$

Equation (4-15) can be further simplified by substituting for the wave numbers k , m , and n , giving

$$\begin{aligned} R & \equiv \frac{\tilde{A}}{\tilde{A}} \\ & = \frac{\tilde{\alpha}}{\left\{ \tilde{\alpha} + (4\alpha_s + 16\beta_s) \left[\sin^2 \left(\frac{k \Delta x}{2} \right) + \sin^2 \left(\frac{m \Delta y}{2} \right) \right] + (4\alpha_t + 16\beta_t) \sin^2 \left(\frac{n \Delta t}{2} \right) - 4\beta_s \left[\sin^2 (k \Delta x) + \sin^2 (m \Delta y) \right] - 4\beta_t \sin^2 (n \Delta t) \right\}} \end{aligned} \quad (4-16)$$

where the horizontal grid intervals are equal and e , f , and g are wavelengths in terms of grid intervals in the x , y , and t directions, respectively. This analysis uses the weight for $\alpha_s = \alpha_t = 0.01$, $\beta_s = \beta_t = 0.1$.

Equation (4-8) is solved as a boundary value problem using the Liebmann relaxation technique. In this iterative approach, the values of ϕ , at the central grid point and at the v th iteration are modified so that equation (4-8) is identically satisfied on the $(v + 1)$ st iteration. The reduction formula is

$$\phi^{v+1} = \phi^v - \frac{\text{Res}^v}{B} \quad (4-17)$$

where Res^v is the nonsatisfaction of equation (4-8) when ϕ^v is substituted into it, and

$$B = \tilde{\alpha} + 2\left(\frac{\alpha_t}{\Delta t^2} + \frac{\alpha_s}{\Delta x^2} + \frac{\alpha_s}{\Delta y^2}\right) + 6\left(\frac{\beta_t}{\Delta t^4} + \frac{\beta_s}{\Delta x^4} + \frac{\beta_s}{\Delta t^4}\right) \quad (4-18)$$

The selection of the natural boundary conditions and finite difference operator requires that values in two rows of grid points on each side of the grid, except the t_2 side, be held constant during the computations. The finite-difference forms of equations (4-6) and (4-7) may be combined to produce

$$\phi(t_2 + 1) = \frac{D\phi(t_2) - \frac{\beta_t}{2 \Delta t^3} \phi(t_2 - 1)}{C} \quad (4-19)$$

and

$$\phi(t_2 + 2) = \frac{D\phi(t_2 + 1) - \frac{\beta_t}{2 \Delta t^3} \phi(t_2)}{C} \quad (4-20)$$

where

$$C = \frac{\alpha_t}{\Delta t} + \frac{\beta_t}{2 \Delta t^3}$$

and

$$D = \frac{\alpha_t}{\Delta t} + \frac{\beta_t}{\Delta t^3}$$

The values of $\phi(t_2 + 1)$ and $\phi(t_2 + 2)$ are recalculated during each relaxation iteration using the above equations. The relaxation process continues until a predetermined tolerance criterion for the largest residual is met or a specific number of iterations is obtained.

Equations (4-19) and (4-20) may also be used to produce short-range forecast values of ϕ after the relaxation process.

SYNOPTIC SITUATION

On June 6, 1973, an upper-level major full-latitude short wave trough moved into the central United States (figs. 4-1 and 4-2). This trough was associated with a surface cold front stretching from James Bay in Canada to Brownsville, Texas. By June 7, this trough sheared and a cutoff closed low began to form in eastern Texas. This closed 50-kilopascal (500 millibar) low continued to develop and on June 8 was centered southeast of Corpus Christi, Texas. Twenty-four hours later the low had drifted westward into the Big Bend country of Texas. A 101.6-kilopascal (1016 millibar) surface low and occasional thundershower activity were evident in the Corpus Christi-Brownsville area.

The major polar jetstream was along the northern United States border. On June 10, however, the pattern began to change as a second major short wave approached the west coast. In response to this short wave, the 50-kilopascal (500 millibar) closed low in Texas began to move northward and scattered thunderstorms increased over southern Texas. Occasional heavy amounts of rain (≥ 7.6 centimeters (3.00 inches) in 24 hours) were recorded as far north as Houston, Texas. Thus, on the morning of June 11, there was a northward-moving closed 50-kilopascal (500 millibar) low centered in central Texas (fig. 4-3) producing scattered thunderstorms from Dallas, Texas, southward. The short wave trough, which had entered the west coast on June 10, sheared; and the northern portion moved east of the Rockies. The associated Pacific front was located at 7 a.m. central daylight time (c.d.t.) along a line from Sault

St. Marie to Denver, Colorado, then westward to Salt Lake City, Utah (fig. 4-4). The center of the surface moist tongue extended from Houston to Dallas, Texas. The airmass over Oklahoma under the Skylab track at 10:20 a.m. c.d.t. was characterized by a low-level temperature and moisture inversion near 90 kilopascals (900 millibars) with higher level moist layers near 75, 65, and 50 kilopascals (750, 650, and 500 millibars) (fig. 4-5(a)). The latter layer was associated with thin cirrus clouds occasionally recognizable in the Skylab photographs in the visible spectral bands and seen in other weather satellite images taken a short time later. This cirrus cloud deck, which was reported as "thin," is probably one of the most important factors in preventing acquisition of successful temperature and moisture inversions using the S191 spectrometer data. The situation also points to a present major limitation to infrared use. The airmass was potentially unstable, and during the day the thunderstorm activity in Texas moved slowly northward in accord with the 50-kilopascal (500 millibar) system. Thunderstorms spread into the Oklahoma City area by 4 p.m. c.d.t. The major change in the airmass, as reflected in the rawinsonde observations, was an increase in the depth of the moist layer from 95 to 70 kilopascals (950 to 700 millibars) with the mean mixing ratio increasing from 7g/kg at 7:40 a.m. c.d.t. to near 10g/kg by afternoon (fig. 4-5(b)). Surface changes are considered in the following discussion.

HOURLY SURFACE DATA ANALYSIS

The hourly surface pressure, temperature, moisture, and wind data collected on June 11, 1973, of Skylab passage were analyzed by the variational method described in the preceding section. The analysis area was chosen to include the Skylab passage track and the ground-truth sites in Oklahoma (fig. 4-6). The hourly fields of various parameters (figs. 4-7 to 4-12) cover the period of 9:00 a.m. to 5:00 p.m. c.d.t., June 11, 1973. The Skylab passage was approximately 10:20 c.d.t. on that date.

FINE MESH ANALYSIS

The surface hourly data were analyzed using a fine mesh grid with the mesh size of a half degree of latitude (fig. 4-6). The analyzed hourly patterns of pressure, temperature, dewpoint temperature, windspeed, wind direction convergence, and dewpoint temperature convergence are shown in figures 4-7 to 4-12. As a geographical reference, the state border lines are also shown in each figure. Within the 8-hour period between 9:00 a.m. and 5:00 p.m. c.d.t., the pressure slightly deepened at the rate of approximately 0.01 kPa/hr (0.1 mb/hr) almost everywhere, as shown in figure 4-7. This slight variation is a reflection of a low that was located over New Mexico and moving slowly eastward. The pressure was deepening more rapidly in the southern half of the area. The isobars, oriented in the southwest-northeast direction, became more and more aligned in the south-north direction. Some perturbations of the isobars are also observed in the southern half of the area.

The hourly temperature values (fig. 4-8) show, in general, the diurnal variation of temperature in the entire area. However, in the southeastern quadrant, beginning about 1:00 p.m. c.d.t., cooler air moved from the southeastern corner of the area toward the northwest. This cooler airmass is likely associated with the rain-cooled outflow from the old complex thunderstorms developed in north-northeastern Texas during the previous day. The dewpoint patterns (fig. 4-9) also demonstrate the northwestward spread of the rain-cooled air, although in a somewhat complicated manner. Relatively moist air appeared in two major areas in the southeastern quadrant of the area.

The wind fields also support the theory of thunderstorm outflow. Although the isotach patterns (fig. 4-10) do not show much of the outflow, the isogon patterns (fig. 4-11) demonstrate clearly the outflow. The wind direction changed rapidly more to the east after 1 p.m. c.d.t. in the southeast quadrant where the thunderstorm outflow seemed to pass through. Also, from figures 4-10 and 4-11, it is apparent that a front was approaching from the northwest corner of the maps.

The hourly dewpoint convergence ($K \text{ sec}^{-1} \times 10^{-5}$) patterns (fig. 4-12) also support the existence of the two major activities: a cold front and thunderstorm outflow. The dewpoint convergence is associated with developing convective activities such as thunderstorms and cumulus clouds. The dewpoint convergence associated with the cold front is parallel to the frontal zone and has advanced with the front monotonically. The dewpoint convergence is also associated with the old thunderstorm outflow, which may lift the moist air to form new thunderstorms. However, the magnitude of the dewpoint convergence associated with the thunderstorm outflow is weak. It was systematic until about 1 p.m. c.d.t., then became disperse and irregular. The secondary dewpoint convergence appeared in the southwestern area of figure 4-12. This seems to be associated with the advancing and expanding trough activity.

The weather along the Skylab track in the map area during the late morning of June 11, 1973, was primarily scattered cumulus as a result of the solar heating in the morning hours. The convective activity seemed to appear in the area between the old thunderstorm outflow and the cold front, supported by the weak dewpoint convergence shown in figure 4-12. The ground-truth observations made on that day by several groups support the preceding analysis.

REFERENCES

- 4-1. Sasaki, Yoshikazu: Some Basic Formalisms in Numerical Variational Analysis. Monthly Weather Rev., vol. 98, no. 12, Dec. 1970, pp. 875-883.
- 4-2. Sasaki, Yoshikazu: Numerical Variational Analysis With Weak Constraint and Application to Surface Analysis of Severe Storm Gust. Monthly Weather Rev., vol. 98, no. 12, Dec. 1970, pp. 899-910.
- 4-3. Sasaki, Yoshikazu: A Theoretical Interpretation of Anisotropically Weighted Smoothing on the Basis of Numerical Variational Analysis. Monthly Weather Rev., vol. 99, no. 7, Aug. 1971, pp. 698-707.
- 4-4. Wagner, K. K.: Variational Analysis Using Observational and Low-Pass Filtering Constraints. M.S. Thesis, Univ. of Okla., 1971.

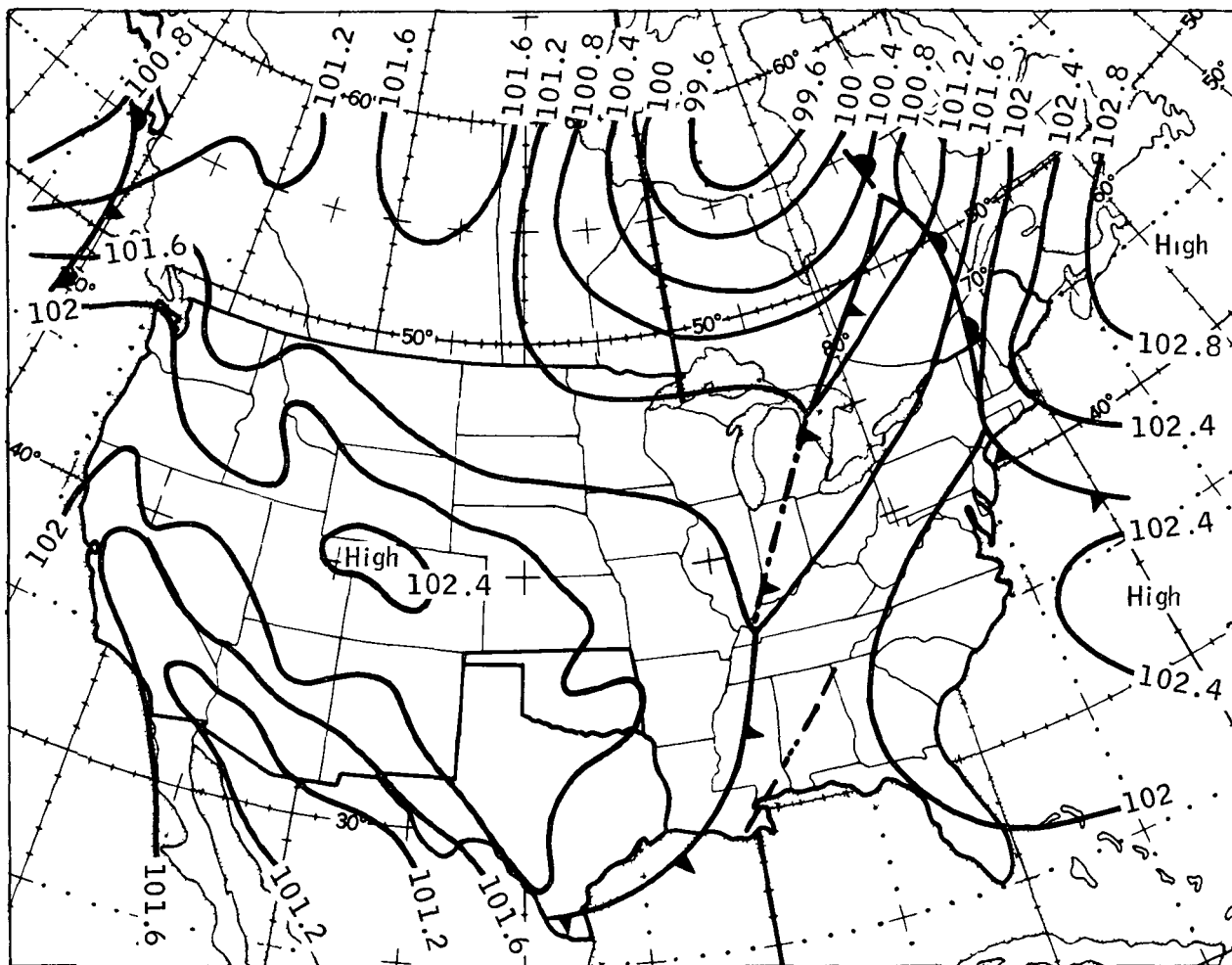


Figure 4-1.- Pressure contours for June 6, 1973, showing a front across the eastern third of the United States. Pressures are in kilopascals.

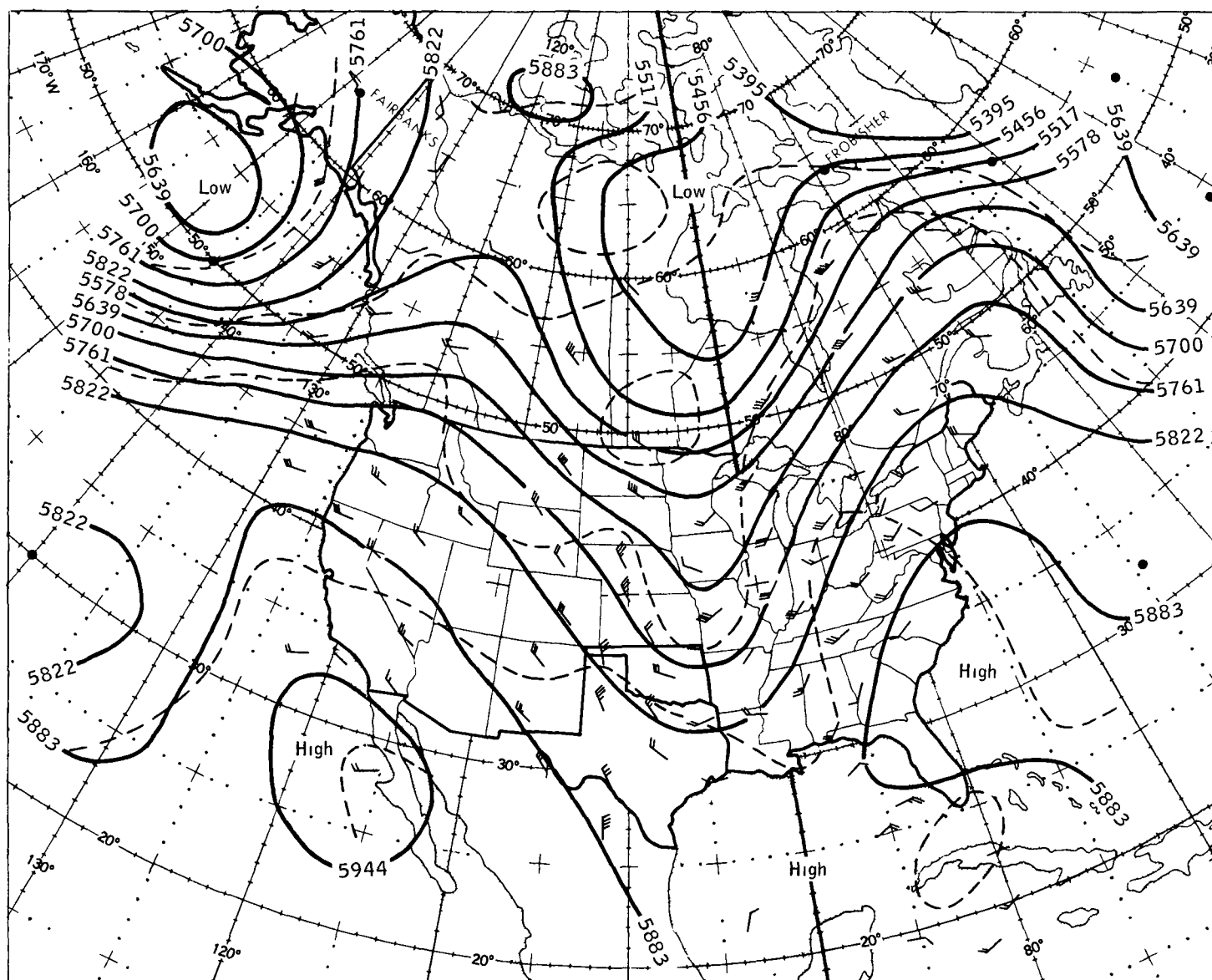


Figure 4-2.- Height contours for June 6, 1973, at 7 a.m. c.d.t. Heights, shown in meters, are at the 50-kilopascal level.

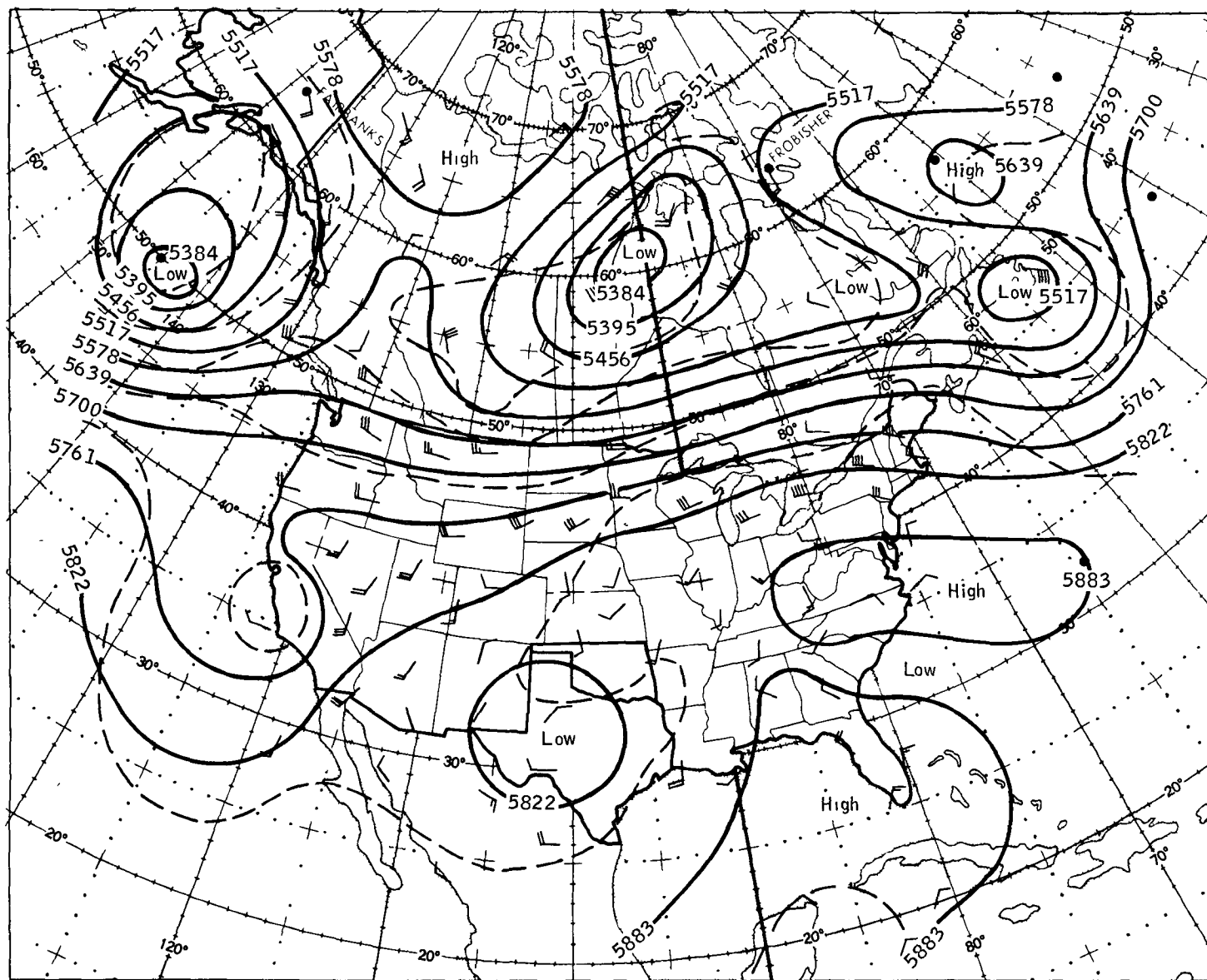


Figure 4-3.- June 11, 1973, height contours, in meters, at the 50-kilopascal pressure level. The time was 7 a.m. c.d.t.

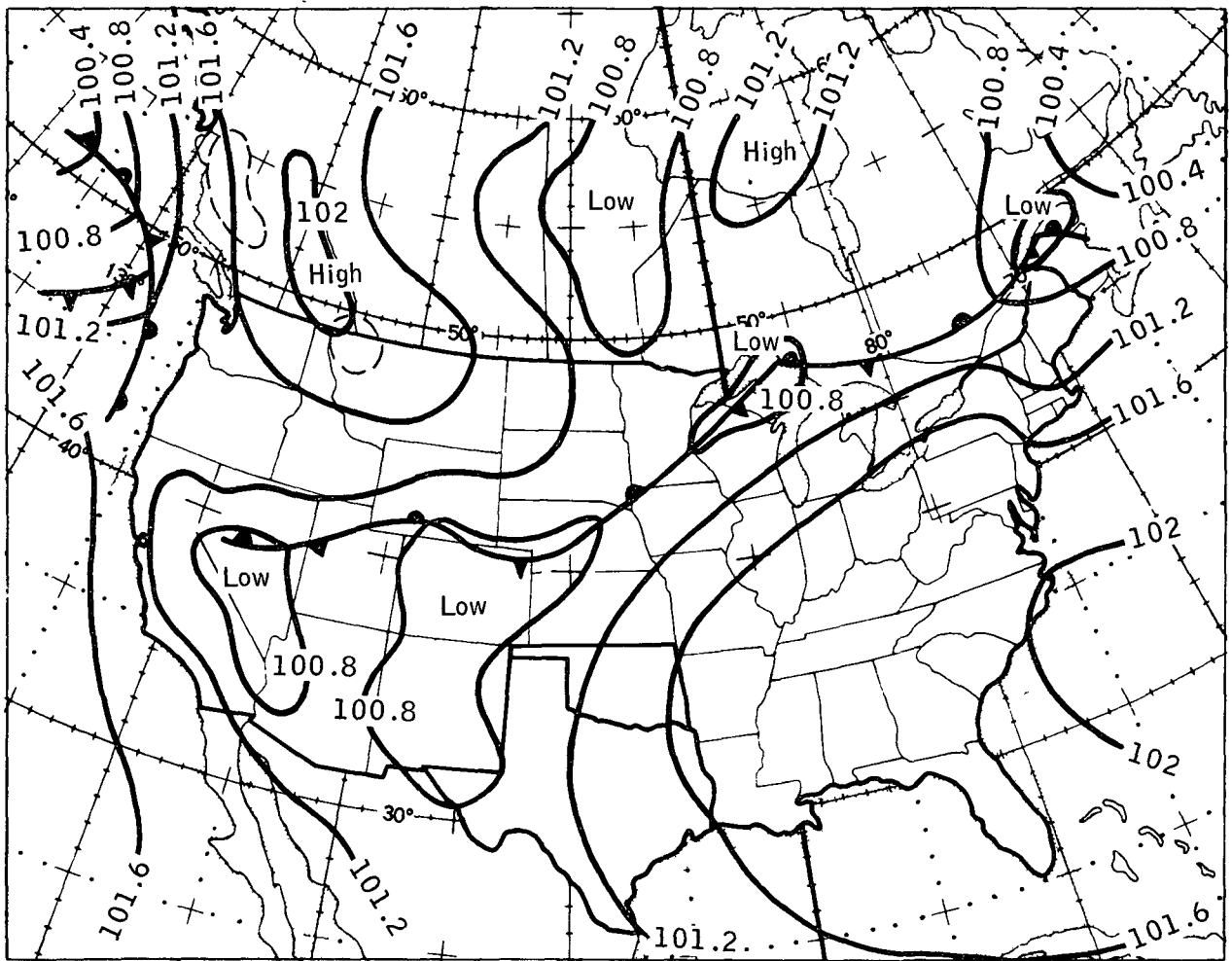
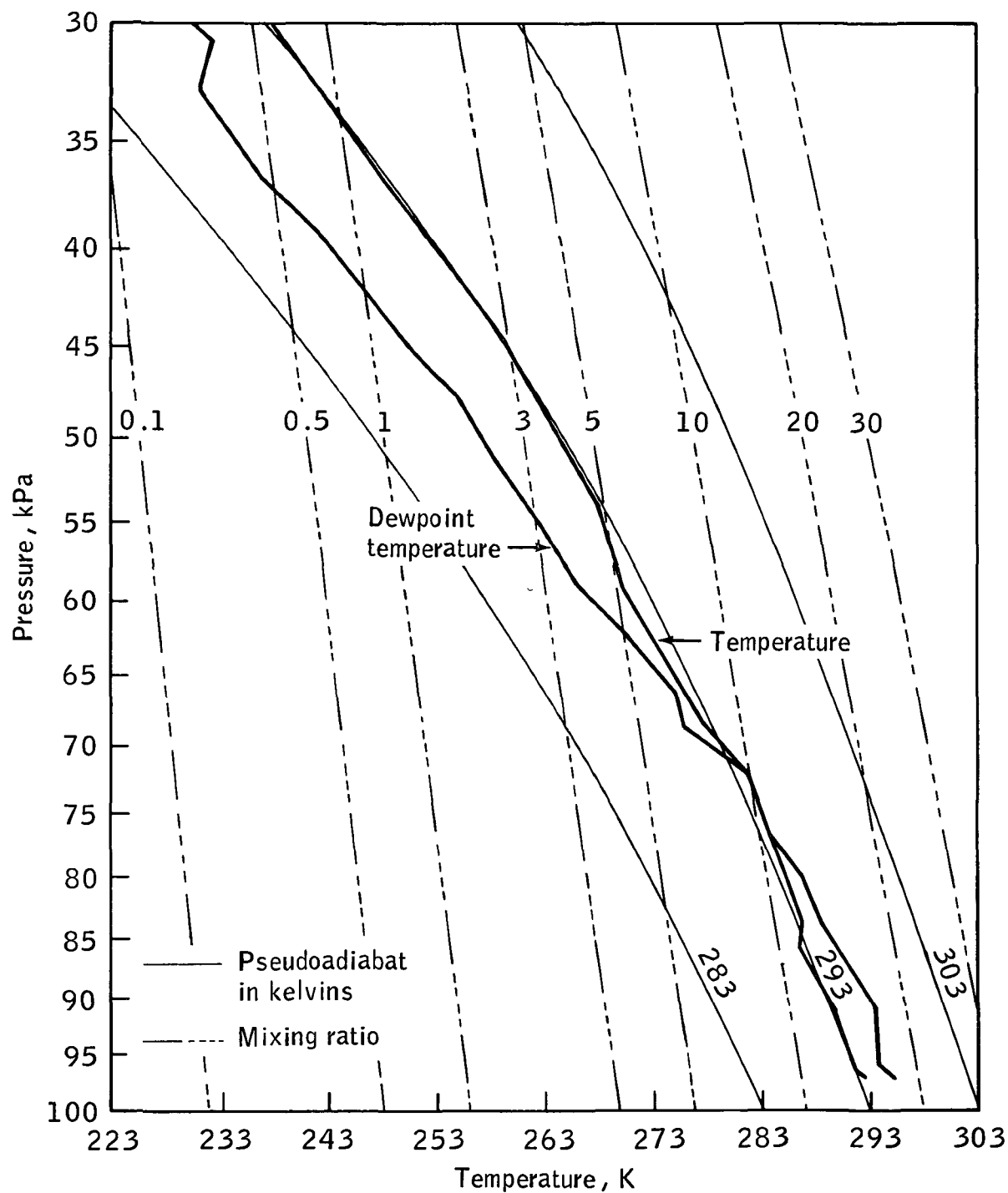
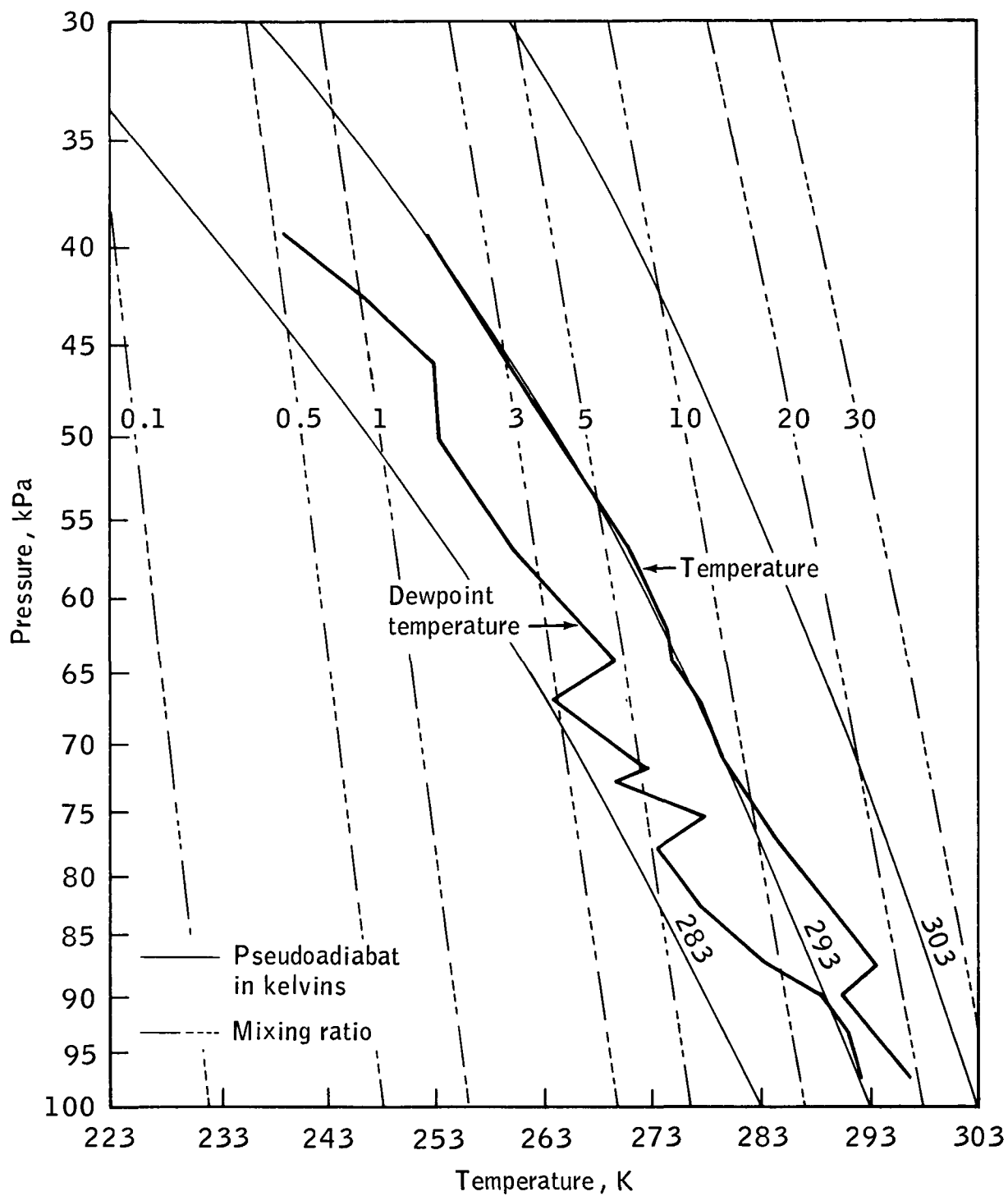


Figure 4-4.- Surface weather map for the same time as figure 4-3, with pressures in kilopascals.



(a) Fort Sill, Oklahoma, at 10:17 a.m. c.d.t.

Figure 4-5.- Radiosonde data for June 11, 1973.



(b) Tinker Air Force Base, Oklahoma, at 5 p.m. c.d.t.

Figure 4-5.- Concluded.

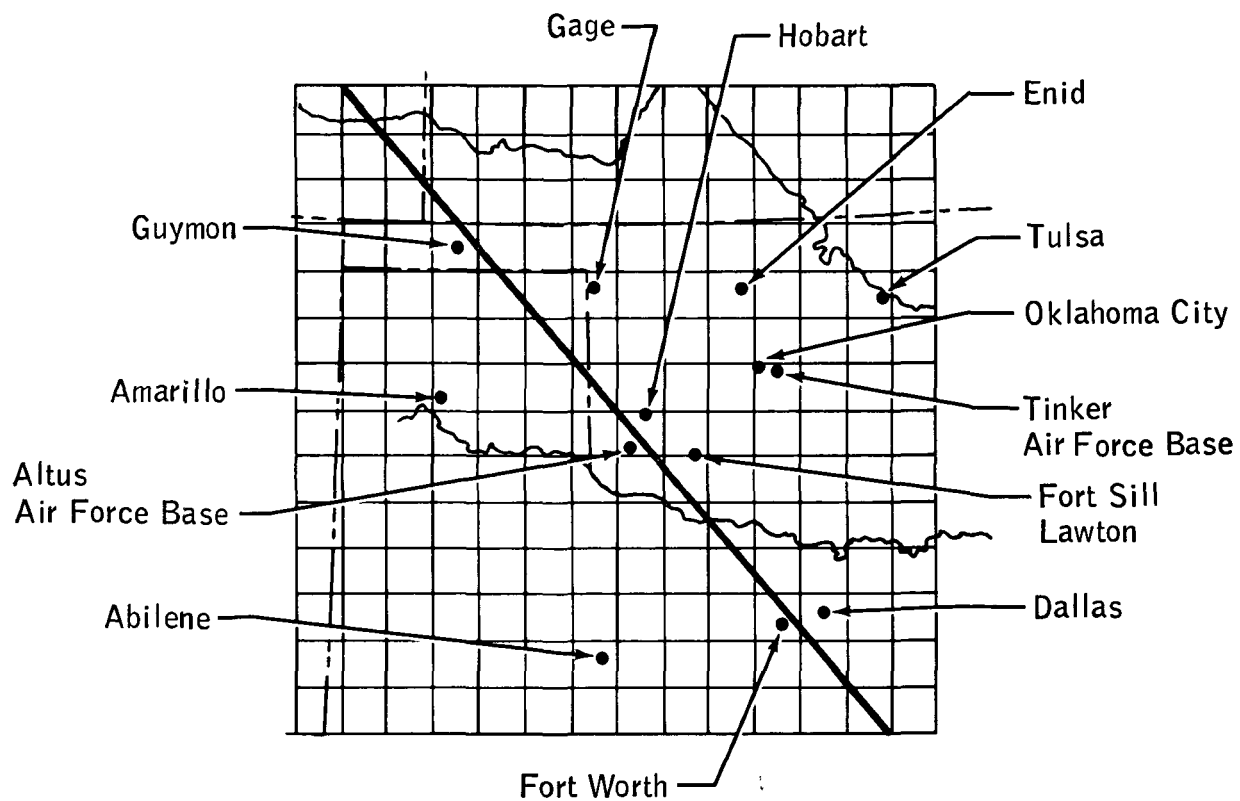
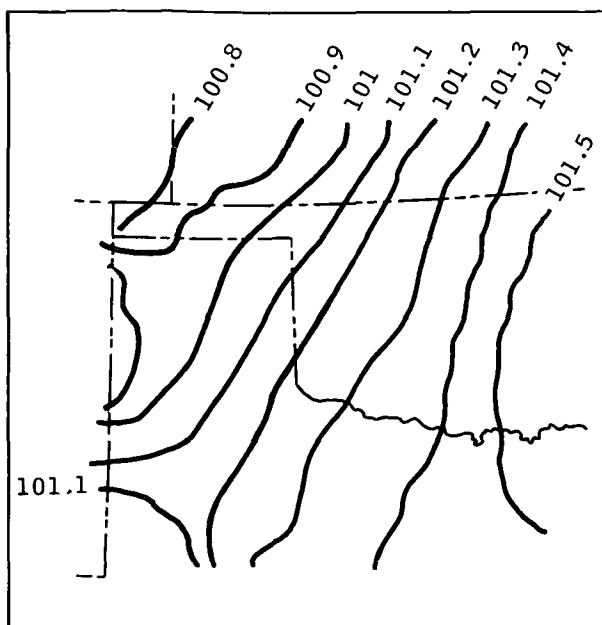
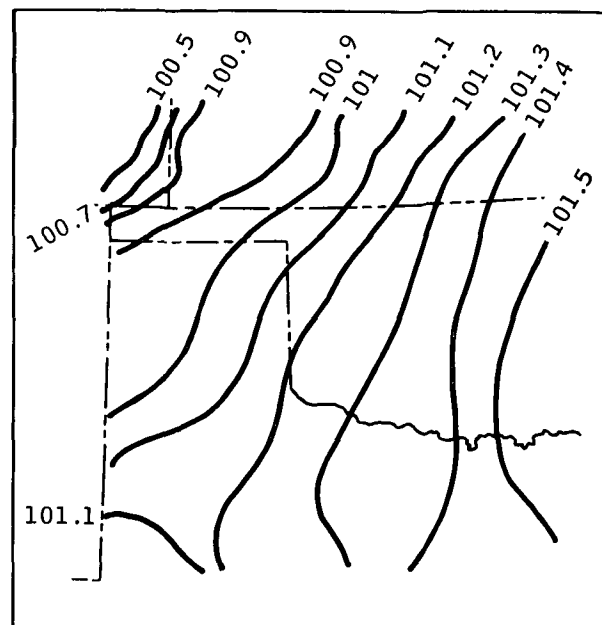


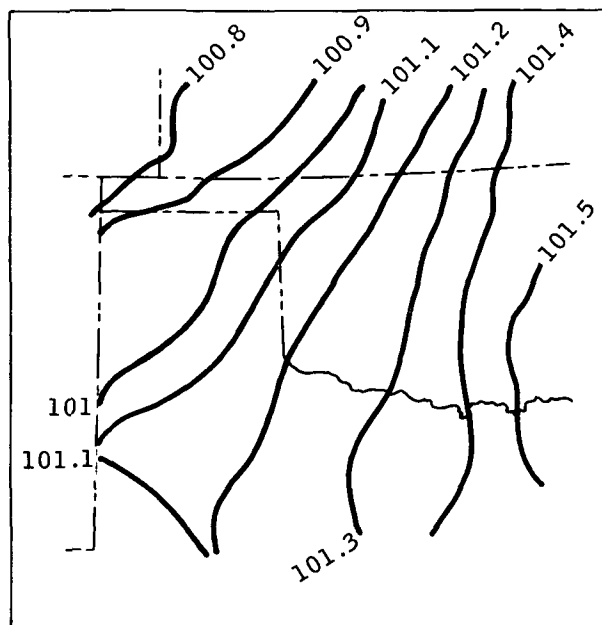
Figure 4-6.- Analysis area in Oklahoma and northern Texas, overlaid with a half-degree grid. Dashed lines indicate state boundaries. The heavy solid line is the location of the Skylab groundtrack.



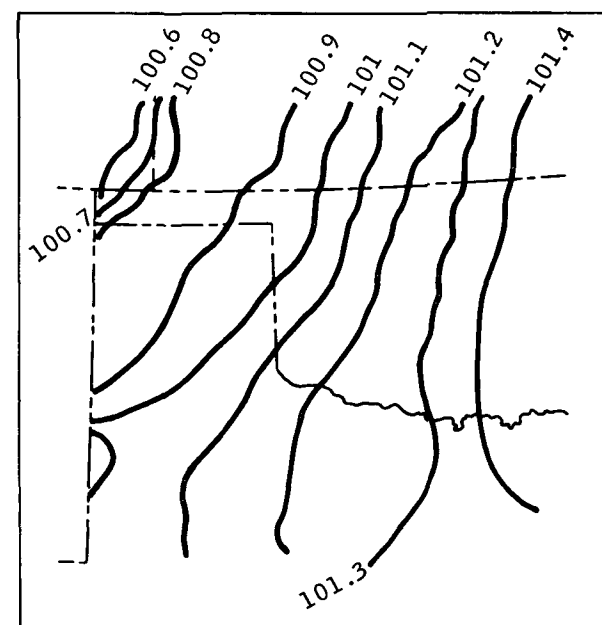
(a) 9 a.m. c.d.t.



(b) 10 a.m. c.d.t.

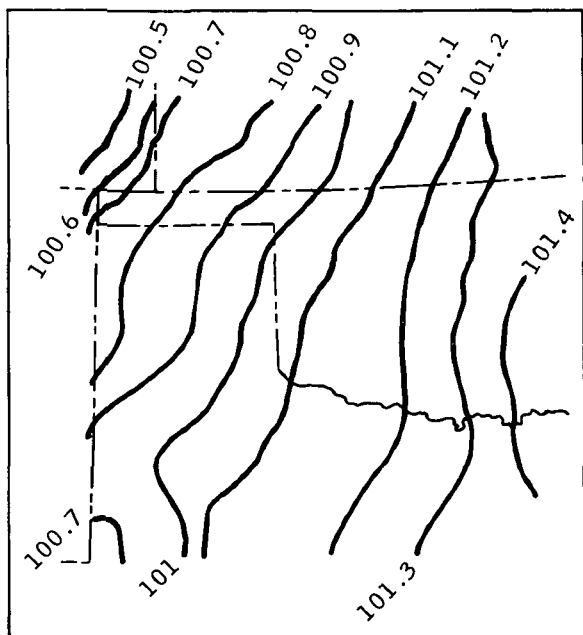


(c) 11 a.m. c.d.t.

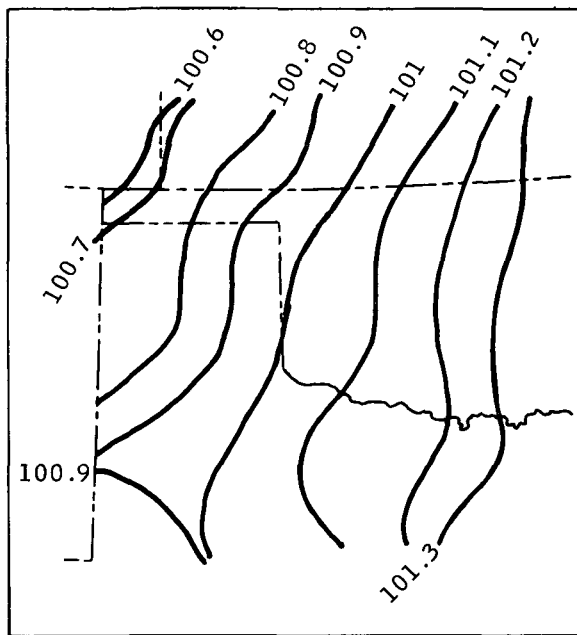


(d) 12 m. c.d.t.

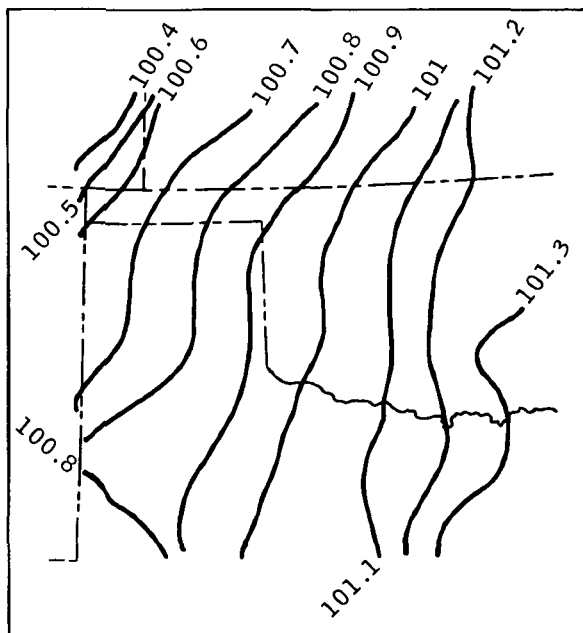
Figure 4-7.- Hourly surface pressure patterns on June 11, 1973. Pressure is shown in kilopascals.



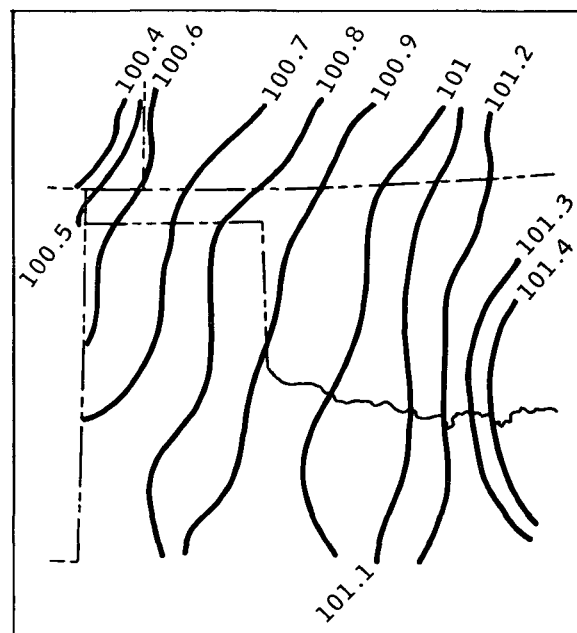
(e) 1 p.m. c.d.t.



(f) 2 p.m. c.d.t.

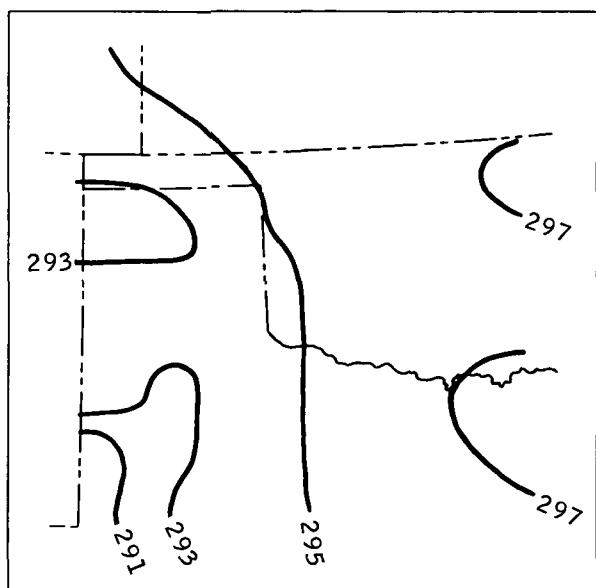


(g) 3 p.m. c.d.t.

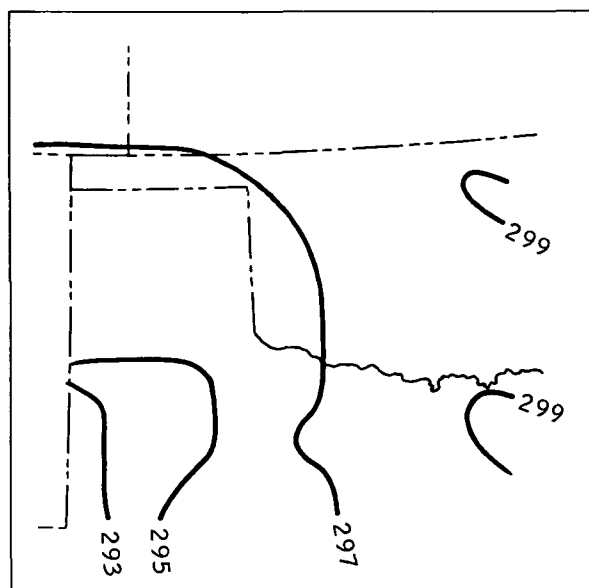


(h) 4 p.m. c.d.t.

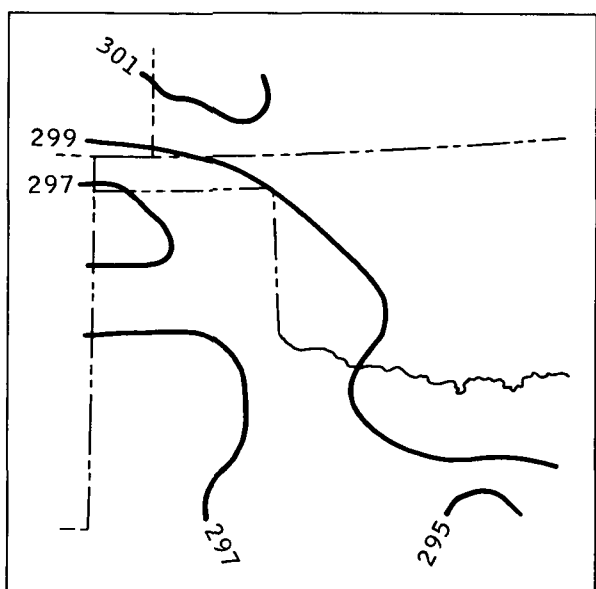
Figure 4-7.- Concluded.



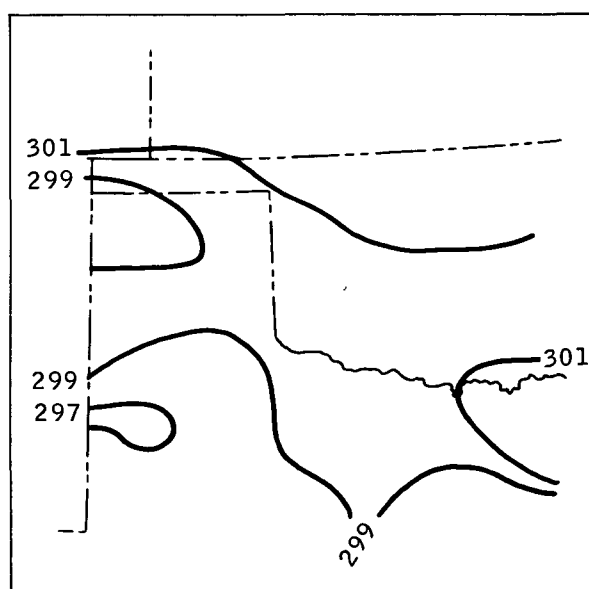
(a) 9 a.m. c.d.t.



(b) 10 a.m. c.d.t.

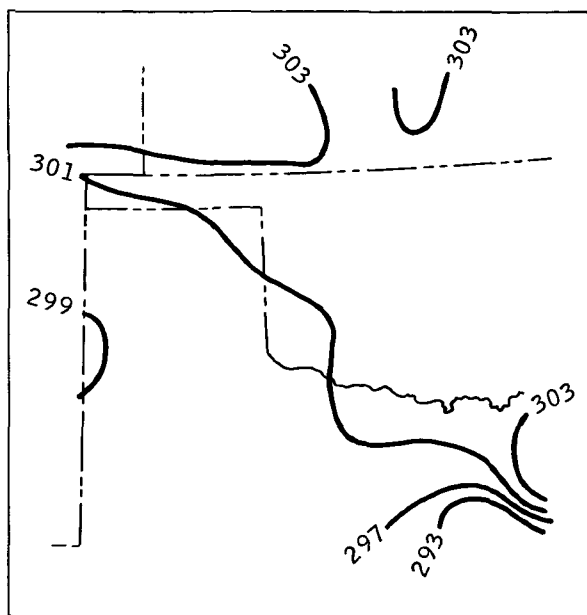


(c) 11 a.m. c.d.t.

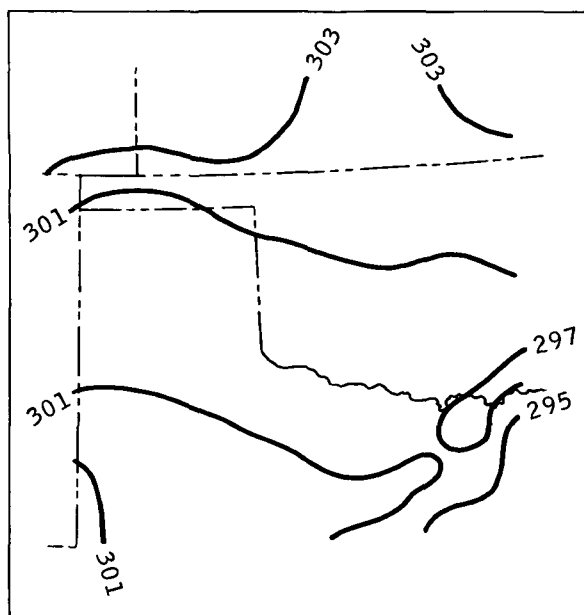


(d) 12 m. c.d.t.

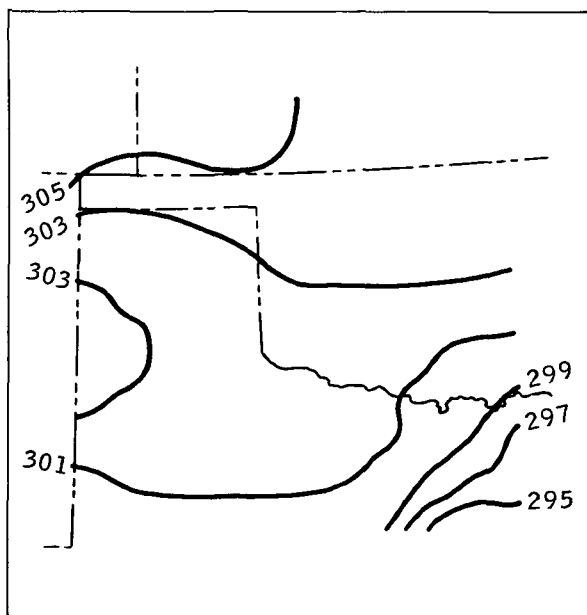
Figure 4-8.- Hourly surface temperature patterns on June 11, 1973. Temperatures are shown in kelvin.



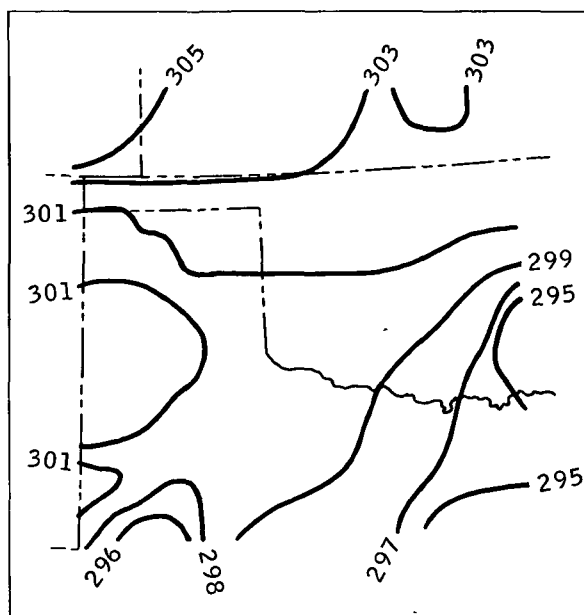
(e) 1 p.m. c.d.t.



(f) 2 p.m. c.d.t.

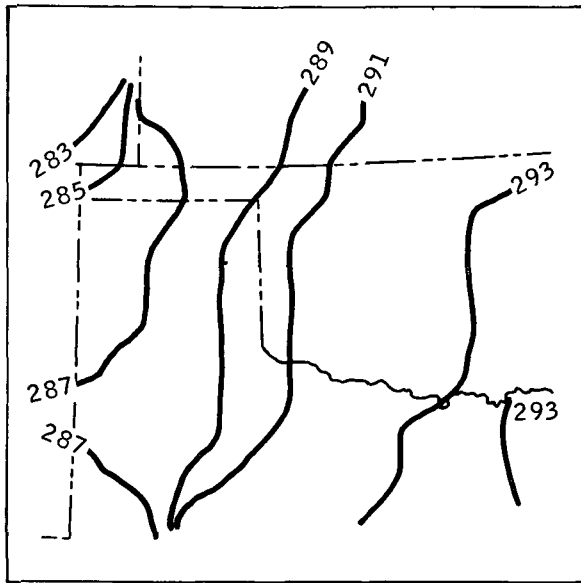


(g) 3 p.m. c.d.t.

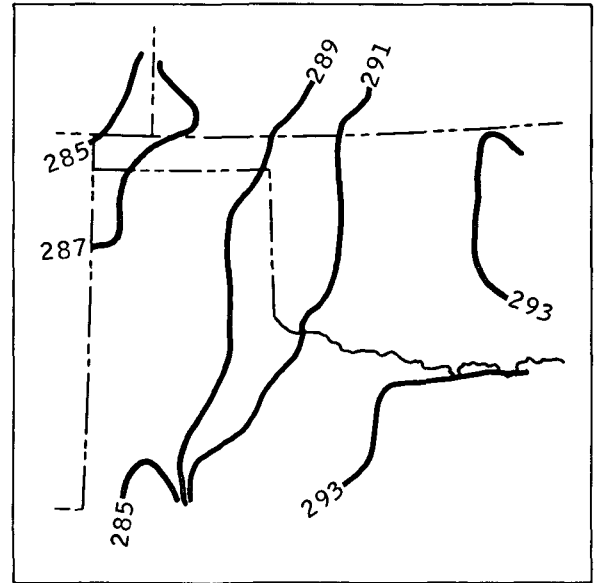


(h) 4 p.m. c.d.t.

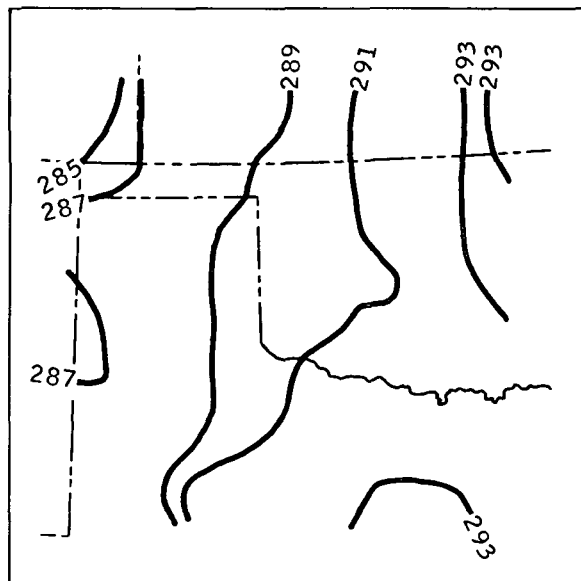
Figure 4-8.- Concluded.



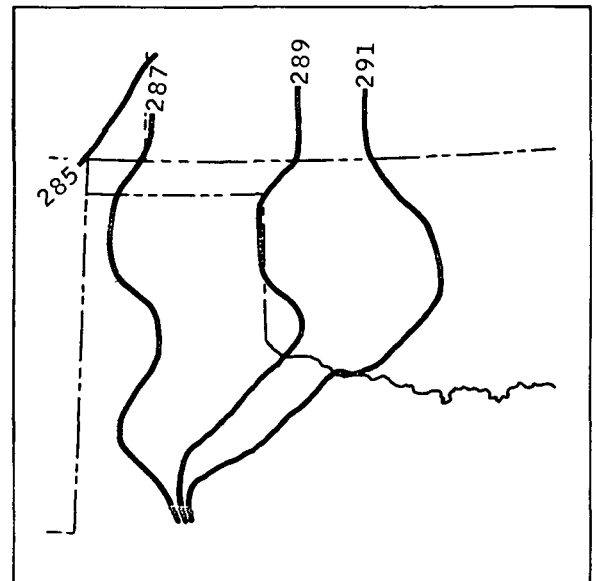
(a) 9 a.m. c.d.t.



(b) 10 a.m. c.d.t.

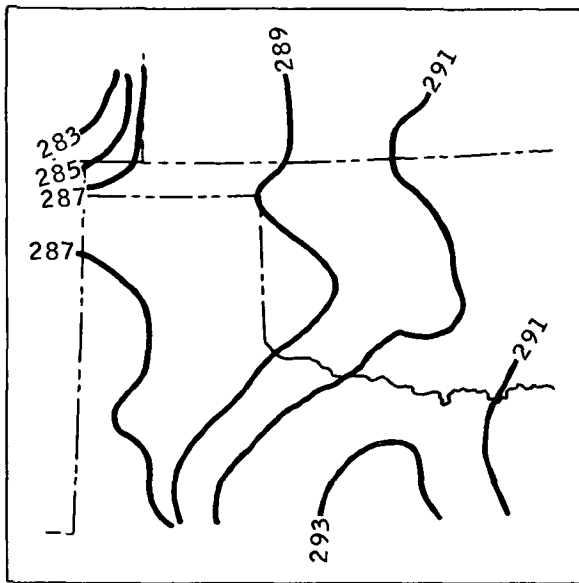


(c) 11 a.m. c.d.t.

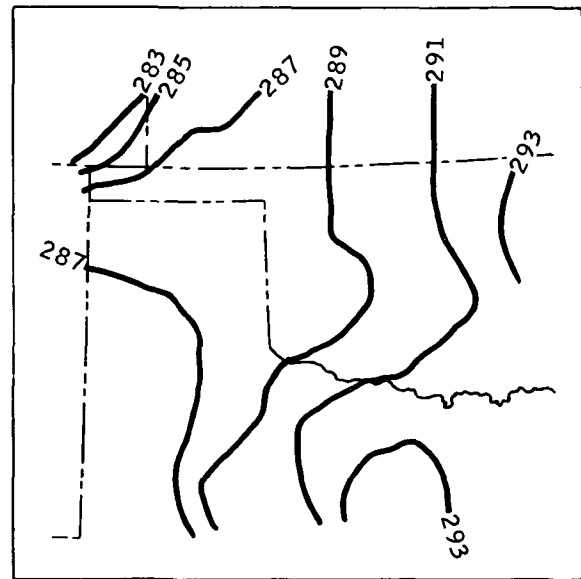


(d) 12 m. c.d.t.

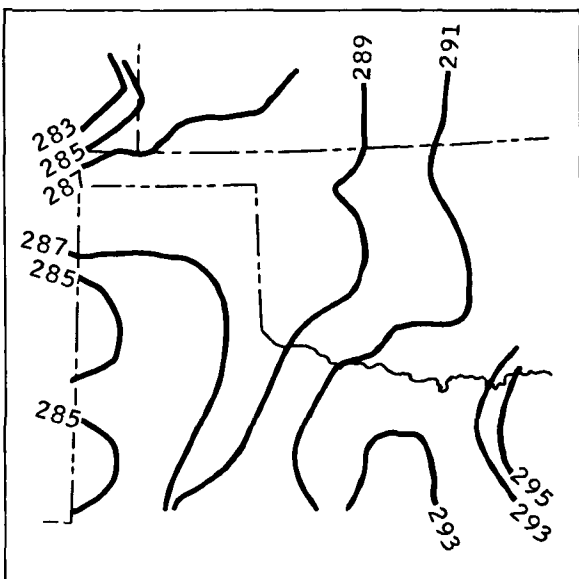
Figure 4-9.- Dewpoint temperatures for June 11, 1973, shown in kelvin.



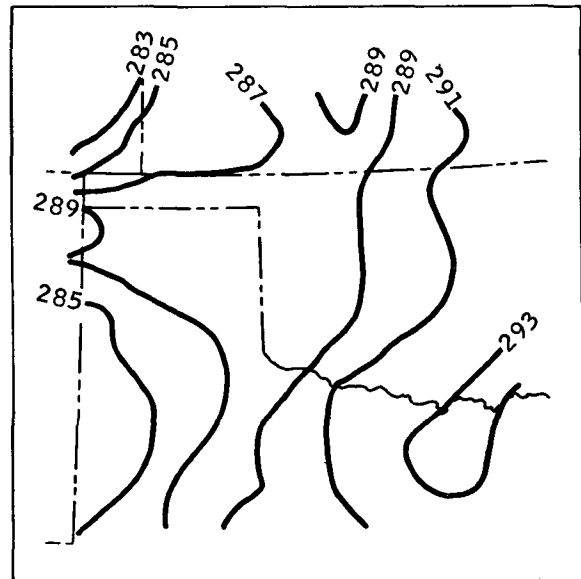
(e) 1 p.m. c.d.t.



(f) 2 p.m. c.d.t.

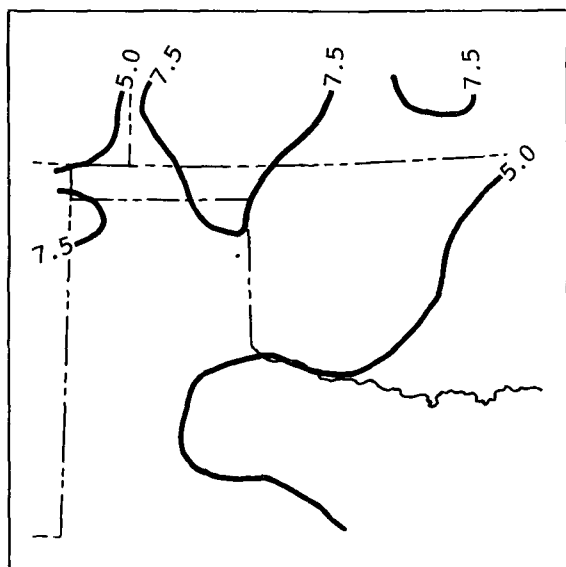


(g) 3 p.m. c.d.t.

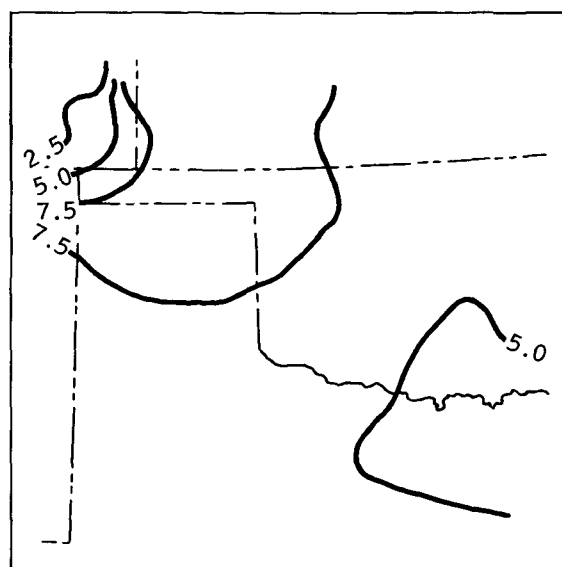


(h) 4 p.m. c.d.t.

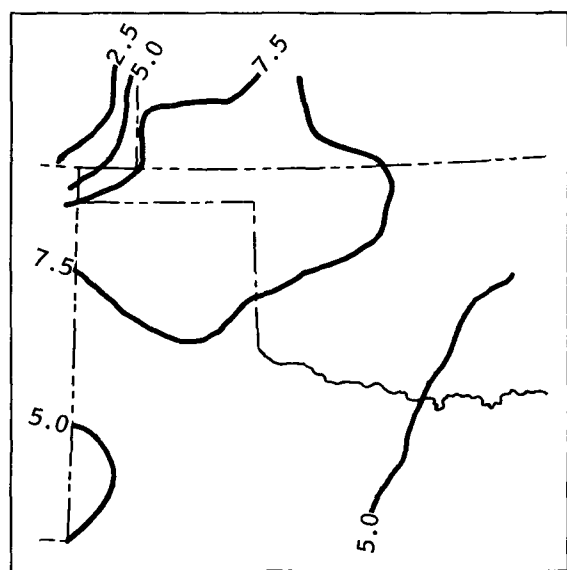
Figure 4-9.- Concluded.



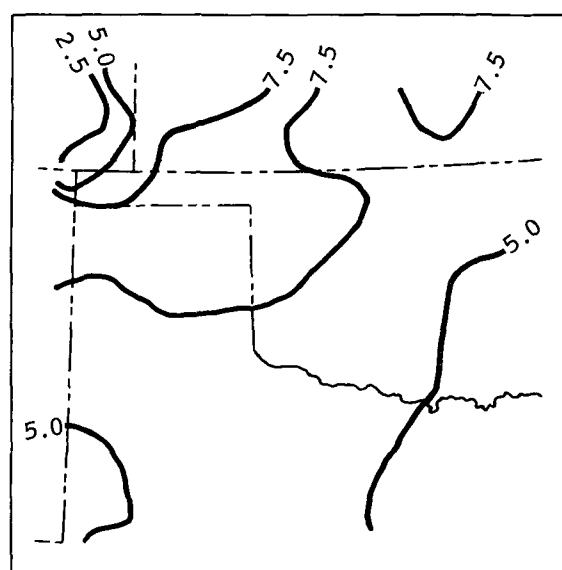
(a) 9 a.m. c.d.t.



(b) 10 a.m. c.d.t.

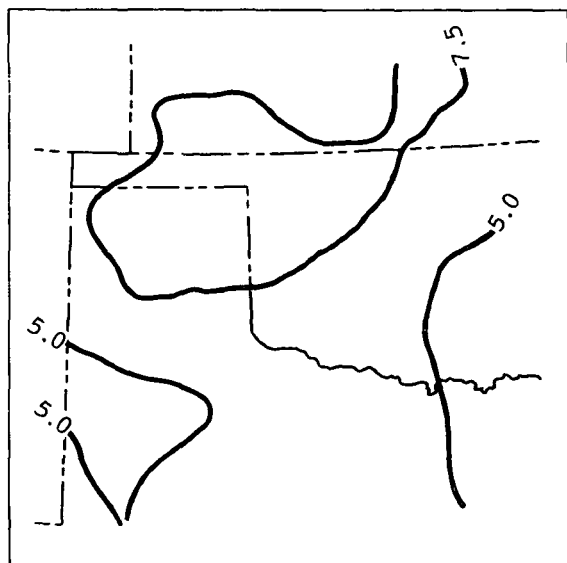


(c) 11 a.m. c.d.t.

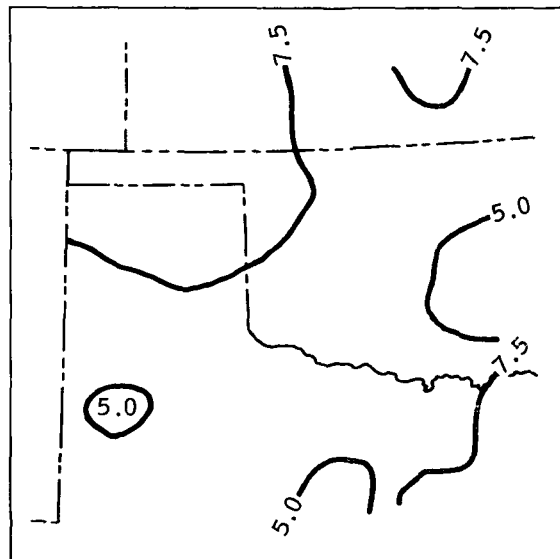


(d) 12 m. c.d.t.

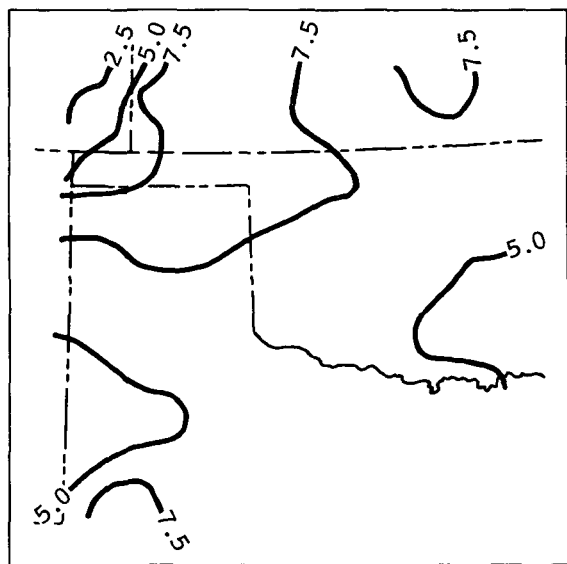
Figure 4-10.- Hourly surface isotach patterns for June 11, 1973. Windspeed is shown in meters per second.



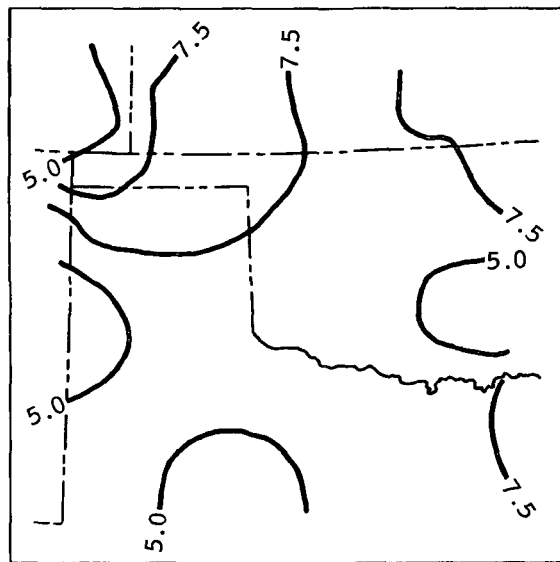
(e) 1 p.m. c.d.t.



(f) 2 p.m. c.d.t.

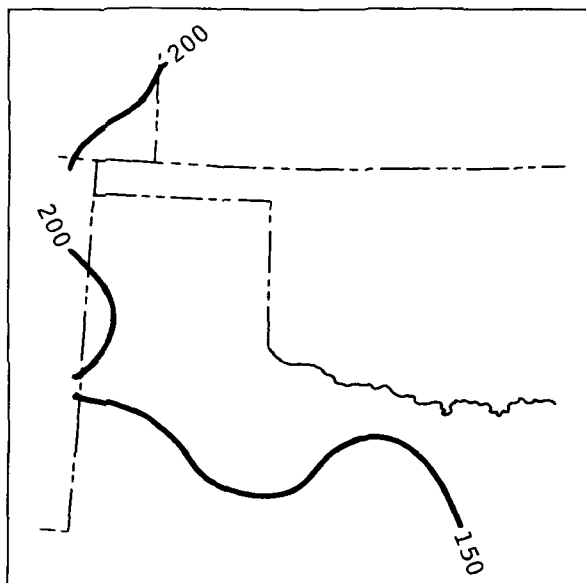


(g) 3 p.m. c.d.t.

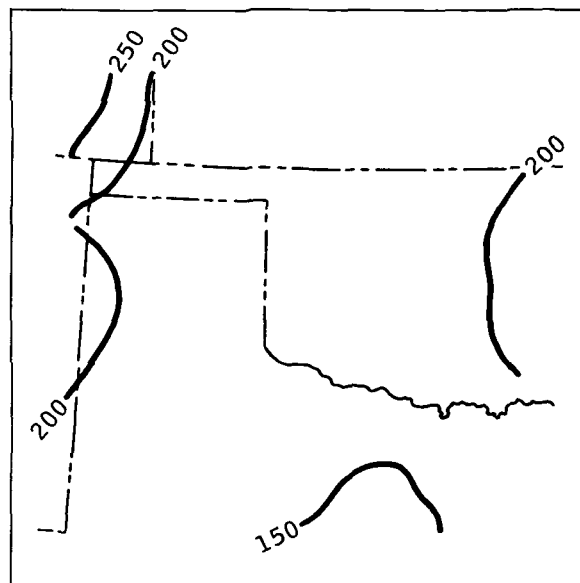


(h) 4 p.m. c.d.t.

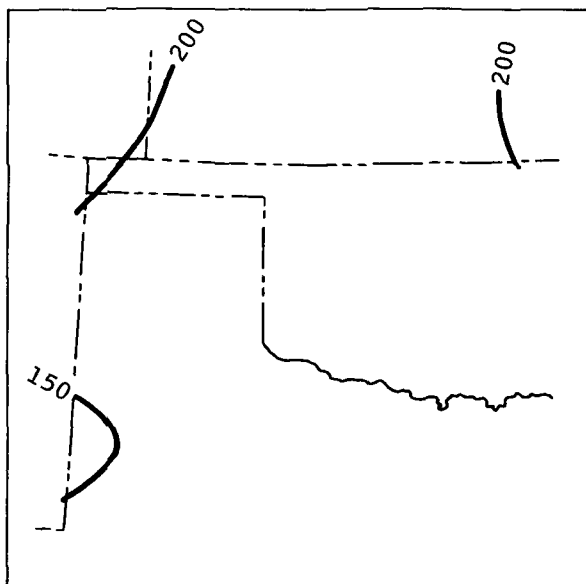
Figure 4-10.- Concluded.



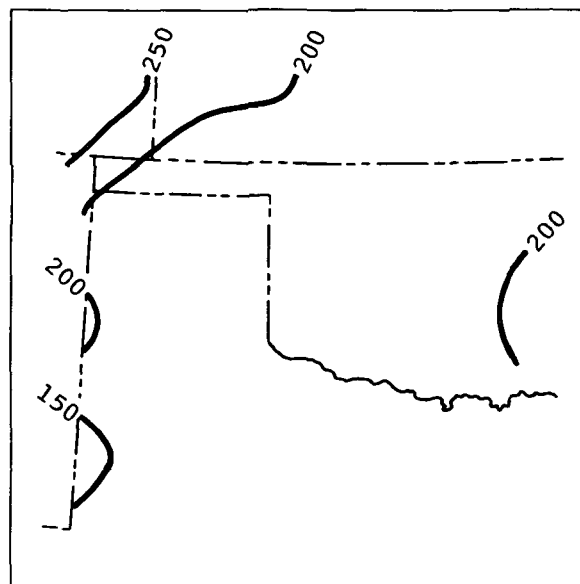
(a) 9 a.m. c.d.t.



(b) 10 a.m. c.d.t.

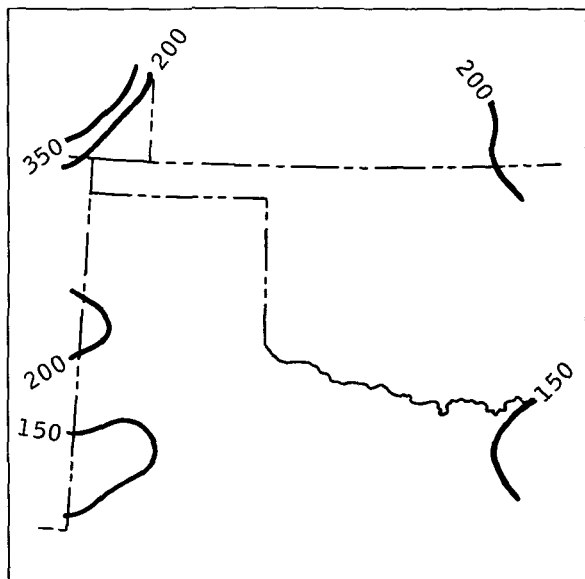


(c) 11 a.m. c.d.t.

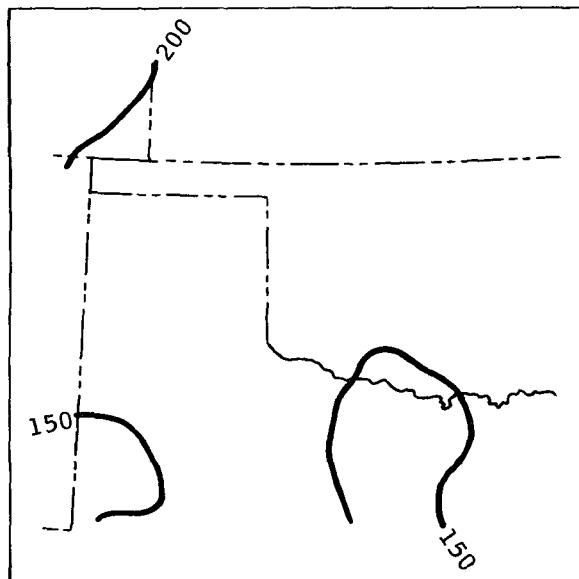


(d) 12 m. c.d.t.

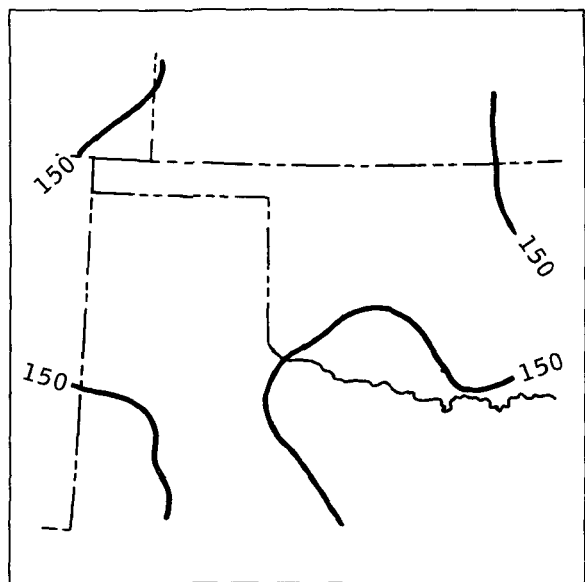
Figure 4-11.- Surface isogon patterns for June 11, 1973, showing azimuth degrees from which the wind was blowing.



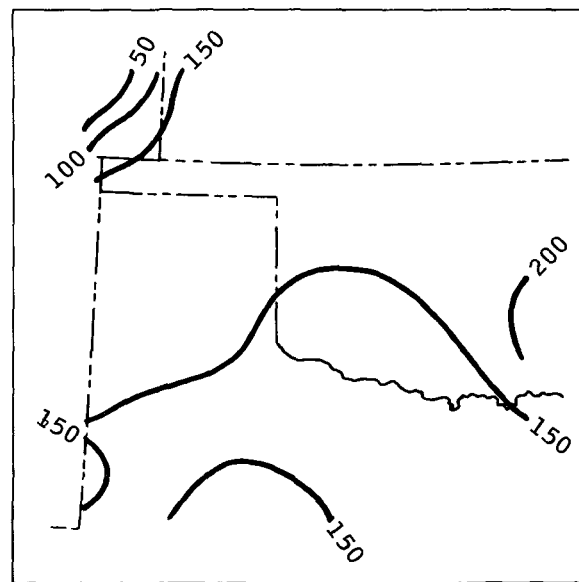
(e) 1 p.m. c.d.t.



(f) 2 p.m. c.d.t.

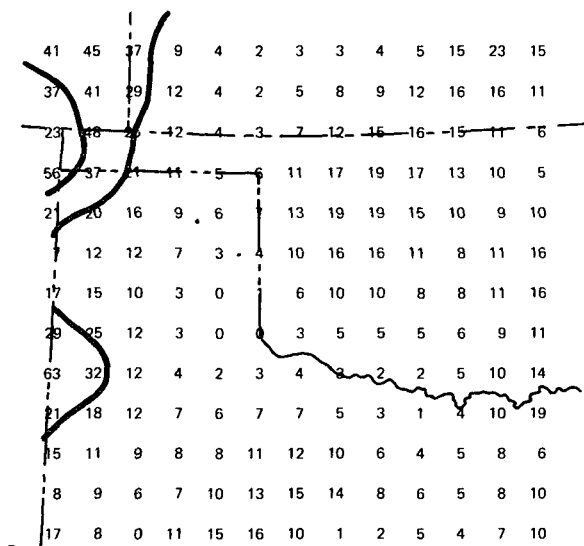


(g) 3 p.m. c.d.t.

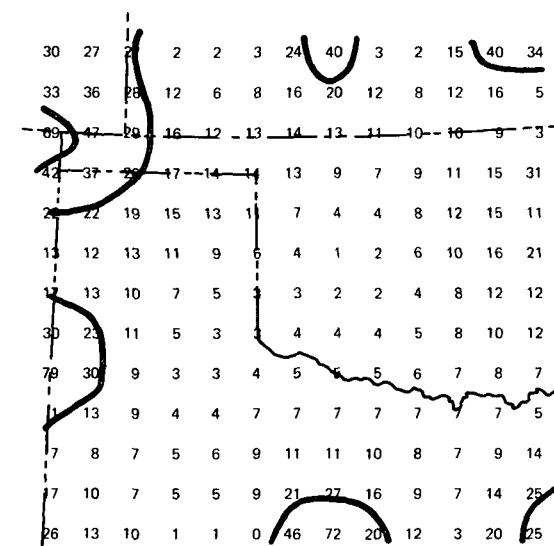


(h) 4 p.m. c.d.t.

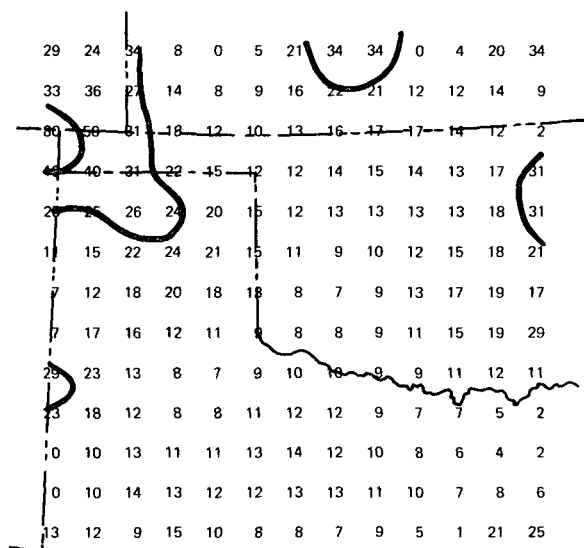
Figure 4-11.- Concluded.



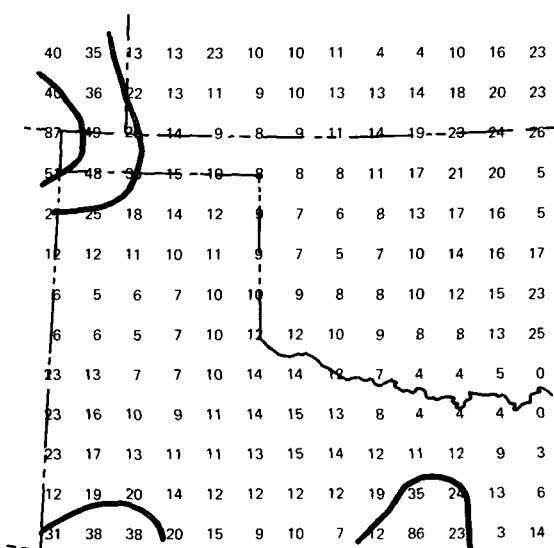
(a) 9 a.m. c.d.t.



(b) 10 a.m. c.d.t.

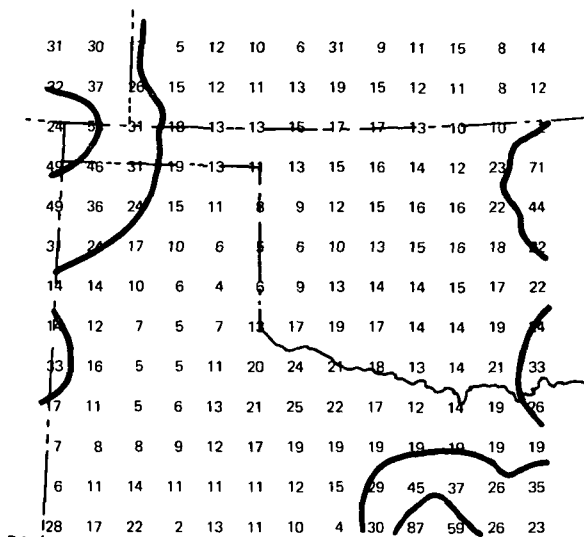


(c) 11 a.m. c.d.t.

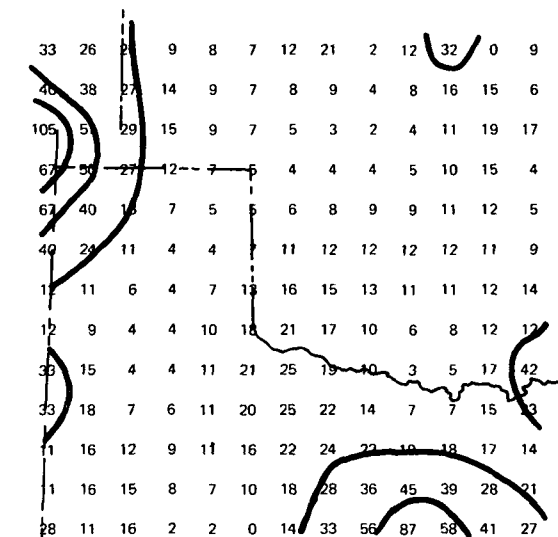


(d) 12 m. c.d.t.

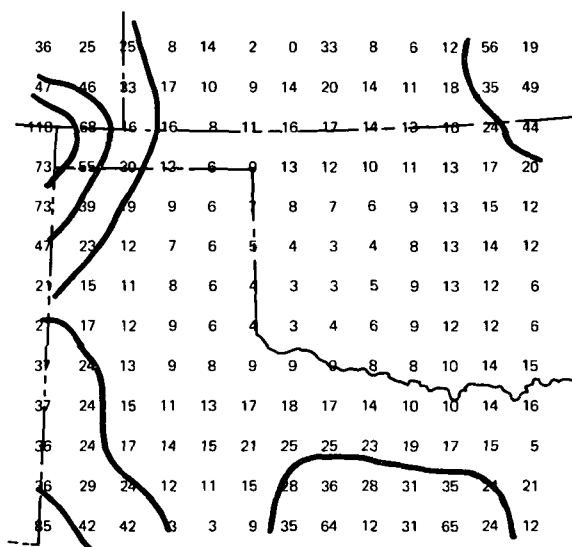
Figure 4-12.- Hourly variations in dewpoint convergence patterns for June 11, 1973. Temperature variances are shown in $K \sec^{-1} \times 10^{-5}$.



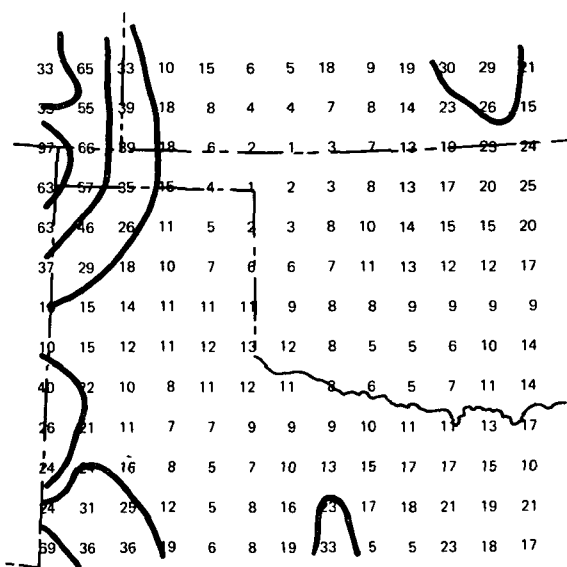
(e) 1 p.m. c.d.t.



(f) 2 p.m. c.d.t.



(g) 3 p.m. c.d.t.



(h) 4 p.m. c.d.t.

Figure 4-12.- Concluded.

5. THE CORRELATION OF SKYLAB L-BAND BRIGHTNESS TEMPERATURES

WITH ANTECEDENT PRECIPITATION

Marshall J. McFarland^a

The accurate determination of the temporal and spatial distribution of soil moisture is important in several disciplines. The meteorologist is interested in the moisture content of the upper several centimeters of the soil because of the governing effects of soil moisture on soil thermal properties, evapotranspiration rates, and the resulting influences on the heat and moisture transport at the atmosphere/Earth boundary. As an example, studies of severe thunderstorms indicate that the inflow air source region is from the near-surface layer of the atmosphere (refs. 5-1 to 5-3). The addition of either heat or moisture to this inflow air will add energy to the storm. Beebe (ref. 5-4) found that the tornado frequency maximums in the Texas Panhandle were centered in the region of extensive irrigation. He attributed the maximums to the increased water vapor content of the lower atmosphere as a result of evapotranspiration from the irrigated fields. The hydrologist is interested in soil moisture content because the soil moisture in the upper several centimeters largely determines the amount of precipitation that appears as surface runoff, the component responsible for flooding. The agronomist requires soil moisture information for the management of agricultural operations and for crop yield estimate models.

Before the advent of remote-sensing technology, accurate soil moisture measurements were possible only through such direct methods as neutron scattering probes, tensiometers, and oven drying and weighing. These methods all have common problems: they are time-consuming and are representative of very small areas. Measurements of soil moisture distribution over large areas, especially those with differing vegetative cover and soil type, and over areas not readily accessible are not possible by direct methods.

When soil moisture information is necessary but not available from direct measurements, the soil moisture content is often inferred from other meteorological variables. Based on the obvious but complex relationships between precipitation, evapotranspiration, surface and subsurface runoff, and soil moisture, the precipitation history over an area is commonly used to infer the soil moisture. From this, the amount of precipitation required to produce flooding for an inferred soil moisture content can be empirically determined.

^aEnvironmental Studies Service Center, National Oceanic and Atmospheric Administration, College Station, Texas. (Research sponsored by NASA Contract NAS9-13360 and conducted at the University of Oklahoma.)

Many models for characterizing the precipitation history have been devised; one of the simplest in concept and computation is (ref. 5-5)

$$API = \sum_{i=1}^n K^i P_i \quad (5-1)$$

where API is the antecedent precipitation index and P_i is the daily precipitation for each day from n days previous to the current day. The parameter K characterizes the loss of moisture from the soil due to evapotranspiration and subsurface runoff. The values of K normally are empirically assigned in the range 0.85 to 0.95 as a function of soil type, slope, season, and vegetative cover. The value may either be constant or a function of time.

REMOTE SENSING OF SOIL MOISTURE

The remote sensing of soil moisture is possible through several physical properties of water and water-soil mixtures. Water has a greater specific heat than soil, so for a given input of heat energy, the temperature of moist soil will be lower than that of dry soil. Similarly, after radiational cooling, the moist soil will have a higher temperature because of its thermal inertia. Thus, remote sensing in the thermal-infrared wavelengths at two or more times during the day can be used to indirectly determine the amount of water present in the surface layer of soil (ref. 5-6).

Another remote-sensing technique for soil moisture content is based on the darkening (decreased reflectance of soil as it is progressively moistened), apparently as a result of the optical effects of surrounding the soil particles with free water. Within a narrow range of soil types and for bare soil, remote sensing in the visible to near-infrared wavelengths can be used to determine the soil moisture areal distribution.

Both of these techniques, although successful under controlled conditions, are completely overshadowed in scope and importance by remote sensing in the microwave portion of the spectrum. Water has the highest dielectric constant of naturally occurring abundant materials; soils have very low dielectric constants at microwave frequencies. When water is added to soil, the resulting mixture will have a dielectric constant proportional to the relative amounts of water, soil, and air present (ref. 5-7). However, if small amounts of water are added to completely dry soil, the water is tightly bound to the soil particles with a low dielectric constant, so the dielectric constant of the mixture does not appreciably change (refs. 5-8 and 5-9). This low water content probably corresponds to hygroscopic water, so it is not available for plant growth. With a greater water content, the water appears as free water in the soil pore spaces and produces the dielectric constant changes predicted and observed in the soil-water-air mixture as the moisture content ranges from the wilting point to field capacity.

The microwave emission of a soil-water-air mixture is determined by its dielectric constant, which is a function of the volumetric water content and, to a much lesser degree, the type of soil. However, the moisture retention and transmission characteristics of an in situ soil are functions of many physical characteristics of the soil, including the type. Thus, the microwave emission from a soil is a function of soil moisture and soil type. The small-scale variations of the soil physical characteristics that hamper direct measurement methods can be minimized through remote sensing from aircraft or satellite altitudes. The radiometer antenna receives radiation from a fairly large ground area, so the integrated radiation measurement provides soil moisture information representative of a large area (ref. 5-10).

The radiation emitted from the surface is modified through scattering, absorption, and emission by surface roughness and vegetative cover (ref. 5-11). Both are wavelength dependent; the modification of radiation from the surface by surface roughness and vegetative cover is lessened at longer microwave lengths. A further advantage of a longer wavelength is that the atmosphere and weather phenomena, including clouds and precipitation, are essentially transparent to the emitted microwave radiation because the particle size is small in relation to the wavelength. At longer wavelengths, remote-sensing operation is not restricted by adverse weather conditions. At shorter microwave wavelengths, such as the 1- to 10-centimeter range commonly used for weather radar, the larger cloud particles and precipitation particles are effective scatterers and absorbers of emitted microwave radiation.

At longer wavelengths, the skin depth (the depth of the surface layer contributing to the total emitted microwave radiation) increases. Although some investigators (ref. 5-12) have reported skin depths in excess of the free-space wavelength at long microwave wavelengths, the general consensus is that the skin depth is on the order of several centimeters under varying field conditions. The major significance is that remote sensing in the microwave portion can provide measurements of the subsurface soil moisture content under varying conditions of soil type, surface roughness, and vegetative cover.

L-BAND MICROWAVE DETECTION OF SOIL MOISTURE

The development of remote-sensing techniques for soil moisture detection has tended to cluster at certain wavelengths. The common "long" microwave wavelength has been near 21 centimeters, which is in the L-band. At L-band wavelengths, the Rayleigh-Jeans approximation of Planck's law states that emitted radiation is linearly proportional to the thermometric or actual temperature of the emitting body (ref. 5-13). The emitted radiation received at the radiometer is thus commonly expressed as a brightness or antenna temperature. The brightness temperature T_A of an object or terrain measured by a radiometer is (ref. 5-14)

$$T_A = L(\epsilon T_g + T_s) + T_a \quad (5-2)$$

where L is the atmospheric transmittance, ϵ is the emissivity of the object or integrated emissivity for the terrain, T_g is the actual temperature of the object or terrain, T_s is the upward scattered radiation, and T_a is the atmospheric emission. At L-band wavelengths, the atmospheric transmittance is very close to unity and both the scattered radiation and the atmospheric emission are very low (ref. 5-15). The brightness temperature can be approximated as

$$T_A = \epsilon T_g \quad (5-3)$$

The brightness temperature will normally be much more responsive to changes in emissivity than to normal changes in surface terrain temperature.

SKYLAB S194 L-BAND RADIOMETER AND DATA ACQUISITION

An L-band radiometer was one of six sensors known collectively as the Earth resources experiments package (EREP). The L-band radiometer (the S194 experiment) measured terrestrial surface groundtracks in the microwave radiation band centered at the 21.4-centimeter wavelength (1.41 gigahertz). The footprint, or sensor instantaneous ground viewing area, at the half-power point (-3 decibels) was a circular area with a 115-kilometer-diameter area for the 15° viewing angle. A footprint of approximately 280 kilometers in diameter accounted for 90 percent of the total energy received at the antenna. The spacecraft altitude was 439 kilometers (237 nautical miles) with an altitude velocity of 7.65 km/sec. The data acquisition rate of the L-band radiometer was approximately three data points per second (one data point per 2.48 surface kilometers). The footprint overlap for each data point was approximately 95 percent.

The S194 L-band soil moisture experiment performed by Eagleman and Lin produced excellent correlations between S194 brightness temperatures and soil moisture (refs. 5-14 and 5-16). For five data sets of groundtracks 100 to 300 kilometers long in Kansas and Texas, soil moisture measurements at six depths for 6-kilometer intervals along the groundtrack centerline were correlated with the S194 brightness temperatures. The correlation coefficients of brightness temperature to soil moisture (percent water by weight) ranged from -0.808 to -0.984 for the uppermost 2.5-centimeter layer and -0.765 to -0.979 for the uppermost 7.5-centimeter layer for the five data sets (ref. 5-16).

Because the half-power footprint had a diameter of more than 100 kilometers, the 100- to 300-kilometer groundtrack lengths represented a few independent measurements. A greater problem was the representativeness of centerline soil moisture measurements at selected sites to the actual soil moisture within the footprint area, especially if the footprint area was not suited for conventional soil moisture sampling or if evapotranspiration or precipitation occurred between the time-consuming sampling and the sensor pass

time. However, in view of the good agreement among the data sets, these high correlations are indicative of the excellent response of the S194 L-band radiometer to soil moisture.

The excellent correlations between the S194 brightness temperature and measured soil moisture imply that S194 L-band radiometer measurements could be used to verify methods of estimating soil moisture from meteorological data. The API was calculated and correlated with S194 L-band brightness temperatures for two data sets. The location of the Skylab groundtracks is included in figure 1-1 of section 1.

June 11, 1973, Data Set

The area of the June 11, 1973, data set included the sandy soils and sparse vegetative cover of the high plains of the Texas and Oklahoma Panhandles and the tight clay soils and heavily vegetated terrain of eastern Texas. The weather conditions at the time of the Skylab pass (Skylab 2, track 48) from 10:18 to 10:20 central daylight time (c.d.t.) varied from thin broken cirrus (not visible in the color photography from the S190A multispectral camera) over the Texas and Oklahoma Panhandles to multilayered overcast conditions from just south of the Red River to the Louisiana border. Precipitating moderate thunderstorms with an areal coverage of 30 percent were occurring from the Fort Worth area to nearly 160 kilometers southeast along the groundtrack. The rainfall amounts were generally light because the cells, as determined from weather radar film from the Greater Southwest Airport in Fort Worth, were 4 to 8 kilometers in diameter and were moving toward the north at 10.3 m/sec (20 knots). The air temperatures along the track ranged from 294 to 299 K.

The S194 brightness temperatures over the area ranged from 229.8 to 275.2 K. For an assumed emitting skin-depth temperature of 298 K (the approximate air temperature along the groundtrack at the time of the data pass), these values would produce an emissivity range from 0.77 for very moist terrain to 0.92 for very dry terrain, with varying vegetative cover.

The API was calculated for each of the 180 precipitation reporting stations of the National Oceanic and Atmospheric Administration (NOAA) climatological network along the groundtrack (refs. 5-17 and 5-18). Two sets of API were calculated for each station. One API set was calculated for the precipitation data of the preceding 11 days (June 1 to 11), and the other API set was calculated for the preceding 5 days.

The precipitation totals for the first 11 days of June 1973 ranged from zero in the Texas and Oklahoma Panhandles to approximately 25 centimeters (10 inches) in the Dallas area. To eliminate the influence of very high daily point values of precipitation in the calculation of the API, the maximum daily rainfall for the API calculation was arbitrarily set at 5.08 centimeters (2.0 inches). The physical rationale for the assumption is that amounts in excess of 5 centimeters contribute to immediate runoff but probably do not contribute to increased soil moisture.

The arithmetic average of the API for the 115-kilometer-diameter footprint coincident with the position of the spacecraft for every third data point was then calculated for correlation with the S194 brightness temperatures. The value of the parameter K was set at 0.9 after trials within the range from 0.85 to 0.95 showed the best correlation of API to S194 brightness temperatures. The S194 brightness temperature at every third data point (one measurement point) and the averaged API for the footprint are shown in figure 5-1.

Figure 5-1 shows that the S194 brightness temperature was highly correlated with the 11-day API but very poorly correlated with the 5-day API. The majority of the precipitation that contributed to the API peak occurred more than 5 days before the Skylab pass. The major point suggested by figure 5-1 is that an API must be based on more than a 5-day precipitation history to be representative of areal soil moisture conditions. The optimal period is not known; the June 11, 1973, data suggest that 10 days (very little precipitation occurred on June 1) is adequate. A 5-day precipitation history is used in the antecedent moisture condition (AMC) in the Soil Conservation Service Handbook of Hydrology (ref. 5-19).

The data of figure 5-1 are plotted as a scatter diagram in figure 5-2. The lack of correlation for API values of less than 1.75 centimeters was consistent with theory but would be a function of soil type.

The equation for the linear least-squares line fitted to the data, excluding the points below 1.75 centimeters API, was

$$\text{API} = 31.99 - 0.114T_A \quad (5-4)$$

and the correlation coefficient was -0.9715. It should be noted, however, that for the 930-kilometer length of the groundtrack, only eight data points were independent for the half-power footprint size.

The influence of the surface water of precipitation and lakes was not apparent, possibly because of the small areal extent in comparison with the sensor footprint size. The surface water may have contributed to the lowest S194 temperatures, but this could not be confirmed.

August 8, 1973, Data Set

The S194 brightness temperatures of the Skylab pass from eastern New Mexico into central Texas on August 8, 1973 (Skylab 3, track 34), were correlated with the areally averaged API calculated from the precipitation reports of the NOAA climatological network (refs. 5-18 and 5-20). The methodology was identical to that used in the June 11 data set: an 11-day period was used, the maximum daily rainfall allowed was 5.08 centimeters, and the value of the K parameter was 0.9. For this data set, the S194 brightness temperature measurements recorded every 2 seconds were used in the correlations. The surface position of the footprint was shifted approximately 14 kilometers

southeastward downtrack for each reading used in the correlation. The number of precipitation reporting stations within the footprint ranged from 4 to 14; the average number was 8. The S194 brightness temperatures and the averaged API over the footprint area are shown in figure 5-3.

The correlation between the API and the S194 brightness temperatures was good. The correlation coefficient of -0.7326 was lower than the -0.9715 of the June 11 data set, primarily as a result of the two anomalous areas indicated by A and B in figure 5-3. At A, the brightness temperature was colder than indicated by the API; at B, the brightness temperature was warmer than indicated by the API. When the June 11 data are used as calibration, the colder brightness temperatures indicate more soil moisture and the warmer temperatures indicate less soil moisture. These areas are also shown when the S194 brightness temperatures and the corresponding API values are plotted as a scatter diagram in figure 5-4.

The August 8 data, with the exceptions of areas A and B, were in general agreement with the June 11 data set as indicated by the linear least-squares fit of the API and S194 measurements. For the data points of area A, the June 11 relationship suggested that the actual surface soil moisture was as much as 0.72-centimeter API equivalent greater than indicated by the API from precipitation.

Geographically, area A corresponded to the high plains of Texas and area B corresponded to the dissected cap-rock area east of the high plains. This suggested that the anomalies of the API-S194 correlations were related to surface physical features and/or cultural practices.

To investigate the effects of cultural practices on API-S194 correlations, the percentage of the footprint area at the half-power point devoted to agriculture was approximated through a Monte Carlo technique. For each of the 43 Texas counties along the groundtrack from the New Mexico border to central Texas, the percentage of the area devoted to cultivated cropland, irrigated cropland, and irrigated cotton was determined from the 1973 Texas County Statistics (ref. 5-21). These percentages were assigned to a point location near the geographic center of the county. The county centroids and the location of the S194 footprint center at each 2-second increment were converted to Cartesian coordinates, and a Monte Carlo technique similar to that used for the objective determination of Thiessen polygons in hydrologic analyses (ref. 5-22) was used to determine the agricultural land use of each footprint.

For each footprint center location, the coordinates of 500 points in the circular footprint area were determined with a random number generator. For each of these points, the closest county centroid was determined. A normalization of the total number of points assigned to each county approximated the percentage of the footprint occupied by each county. The percentage of the footprint devoted to cultivation, irrigation, and irrigated cotton was then determined. These values are shown in figure 5-5 with the S194 brightness temperatures.

With the caveat that the S194 data represent only a few independent measurement points, the lowered brightness temperatures in area A were apparently

a result of soil moisture added through irrigation. For area A, the correlation coefficient between API and S194 brightness temperature was -0.24 , which indicated a poor correlation between API and soil moisture as indicated by the S194 sensor. Cotton is normally extensively irrigated during late July and early August in the high plains, so a correlation coefficient was calculated for the S194 readings and the percentage of irrigated cotton in the footprint area. This correlation coefficient was -0.92 for area A and -0.95 for the entire groundtrack in Texas. Definite conclusions cannot be drawn because of the limited data sample, but a strong possibility exists that the increased soil moisture detected by the S194 sensor was due to irrigation practices. This soil moisture measurement would be virtually impossible to quantify from direct soil moisture measurement techniques.

For area B, the footprint percentage of cultivated land indirectly provided a rough parameterization of soil type and surface relief. The very low footprint percentage of cultivated land was indicative of the dissected topography and rocky terrain of the cap-rock break. For this type of terrain, the recession parameter K should be decreased to allow for the increased soil moisture lost to surface and subsurface runoff. The effects of the surface roughness on the emitted radiation were not determined.

A difference between the two data sets was the apparent response of the S194 brightness temperatures to low values of soil moisture in eastern New Mexico in the August 8 data set. The data sets of Eagleman and Lin (ref. 5-14) also showed varying degrees of S194 responsiveness to low soil moisture values.

CONCLUSIONS

In view of the limited number of independent measurements, definite conclusions could not be reached. However, the general agreement between the June 11 and August 8 data sets and the agreement between the results of this research and Eagleman's research provided several strong hypotheses. The L-band of the microwave wavelength is well suited for the remote sensing of synoptic soil moisture over large areas under a wide variety of weather and terrain conditions. The correlations between Eagleman's direct measurements of soil moisture and S194 brightness temperature and the correlations between the S194 brightness temperature and an 11-day API indicate that an API averaged over a large area can provide an accurate parameterization of soil moisture. To describe the soil moisture, the precipitation history for at least a 10-day period must be included, however. As microwave remote sensing continues to develop, especially with the Space Shuttle Program, the data sets will provide an excellent data base to develop and refine evapotranspiration and soil moisture models for meteorological, hydrological, and agronomic purposes.

REFERENCES

- 5-1. Marwitz, John D.: The Structure and Motion of Severe Hailstorms; Part I: Supercell Storms. J. Appl. Meteorol., vol. 11, no. 1, Feb. 1972, pp. 166-179.
- 5-2. Davies-Jones, Robert P.: Discussion of Measurements Inside High-Speed Thunderstorm Updrafts. J. Appl. Meteorol., vol. 13, no. 6, Sept. 1974, pp. 710-717.
- 5-3. Sasaki, Yoshikazu K.: Mechanism of Squall-Line Formation as Suggested From Variational Analysis of Hourly Surface Observations. Proceedings of the Eighth Conference on Severe Local Storms, American Meteorological Society, 1973, pp. 300-307.
- 5-4. Beebe, R. C.: Large Scale Irrigation and Severe Storm Enhancement. Proceedings of the Symposium on Atmospheric Diffusion and Air Pollution, American Meteorological Society, 1974, pp. 392-395.
- 5-5. Linsley, Ray K., Jr.; Kohler, M. A.; and Paulhus, J. L. H.: Hydrology for Engineers. McGraw-Hill, 1958.
- 5-6. Blanchard, Maxwell B.; Greely, Ronald; and Goettelman, Robert: Use of Visible, Near-Infrared, and Thermal Infrared Remote Sensing to Study Soil Moisture. Proceedings of the Ninth International Symposium on Remote Sensing of Environment, Vol. I, Environmental Research Institute of Michigan, 1974, pp. 693-700.
- 5-7. Poe, G.; Stogryn, A.; and Edgerton, A. T.: Determination of Soil Moisture Content Using Microwave Radiometry. Summary Report 1684R-2 (contract 0-35239), Aerojet-General Corp., 1971.
- 5-8. Schmugge, T.; Gloerson, P.; and Wilheit, T.: Remote Sensing of Soil Moisture With Microwave Radiometer. NASA TM X-66265, 1973.
- 5-9. Schmugge, T.; Gloerson, P.; Wilheit, T.; and Geiger, F.: Remote Sensing of Soil Moisture With Microwave Radiometer. J. Geophys. Res., vol. 79, no. 2, Jan. 10, 1974, pp. 317-323.
- 5-10. Eagleman, J. R.; and Ulaby, F. T.: Remote Sensing of Soil Moisture by Skylab Radiometer and Scatterometer Sensors. AAS Paper 74-146, Aug. 1974.
- 5-11. Newton, R. W.; Lee, S. L.; Rouse, J. W., Jr.; and Paris, J. F.: On the Feasibility of Remote Monitoring of Soil Moisture With Microwave Sensors. Proceedings of the Ninth International Symposium on Remote Sensing of Environment, Vol. I, Environmental Research Institute of Michigan, 1974, pp. 725-738.

- 5-12. Poe, G.; and Edgerton, A. T.: Soil Moisture Mapping by Ground and Airborne Microwave Radiometry. Fourth Annual Earth Resources Program Review, Vol. IV, NASA TM X-68563, 1972, pp. 93-1 to 93-23.
- 5-13. Allison, L. J.; Rodgers, E. B.; Wilheit, T. T.; and Wexler, R.: A Multi-Sensor Analysis of Nimbus 5 Data on 22 January 1973. NASA TM X-70633, 1973.
- 5-14. Eagleman, Joe R.; and Lin, Wen C.: Soil Moisture Detection From Skylab. Proceedings of the Earth Resources Survey Symposium, Vol. I-D, NASA TM X-58168, pp. 2233-2241.
- 5-15. Blanchard, B. J.: Passive Microwave Measurement of Watershed Runoff Capability. Ph. D. Dissertation, Univ. of Okla., 1974.
- 5-16. Eagleman, J. R.: Moisture Detection From Skylab. Proceedings of the Ninth International Symposium on Remote Sensing of Environment, Vol. I, Environmental Research Institute of Michigan, 1974, pp. 701-705.
- 5-17. Climatological Data — Oklahoma, vol. 82, no. 6. NOAA Environmental Data Service, Asheville, N.C., 1973.
- 5-18. Climatological Data — Texas, vol. 78, nos. 6-8. NOAA Environmental Data Service, Asheville, N.C., 1973.
- 5-19. SCS National Engineering Handbook. Section 4: Hydrology. USDA Soil Conservation Service, 1972.
- 5-20. Climatological Data — New Mexico, vol. 77, nos. 7-8. NOAA Environmental Data Service, Asheville, N.C., 1973.
- 5-21. 1973 Texas County Statistics. Texas Crop and Livestock Reporting Service, 1974.
- 5-22. Diskin, M. H.: On the Computer Evaluation of Thiessen Weights. J. Hydrology, North-Holland Publishing Co. (Amsterdam), vol. 11, no. 1, July 1970, pp. 69-78.

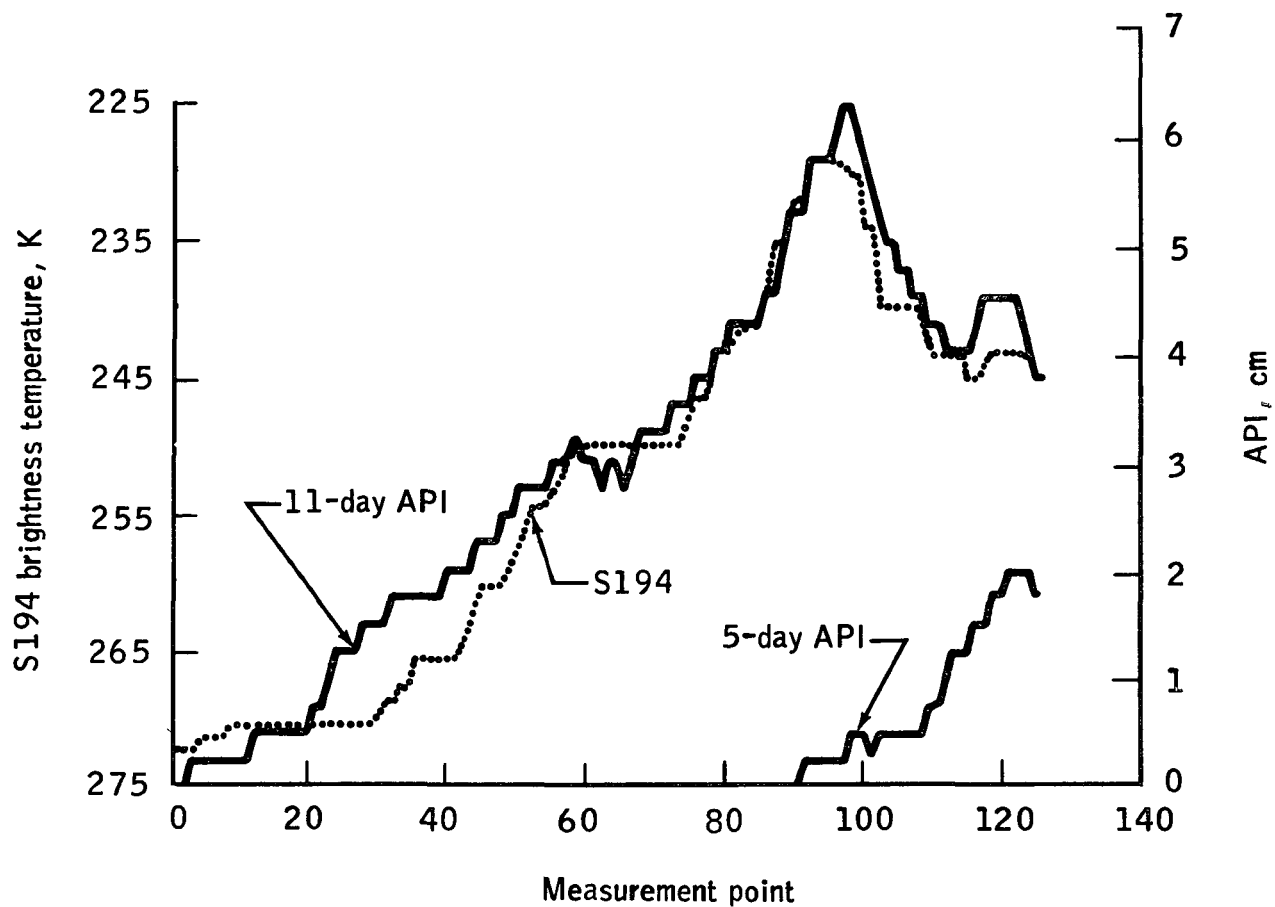
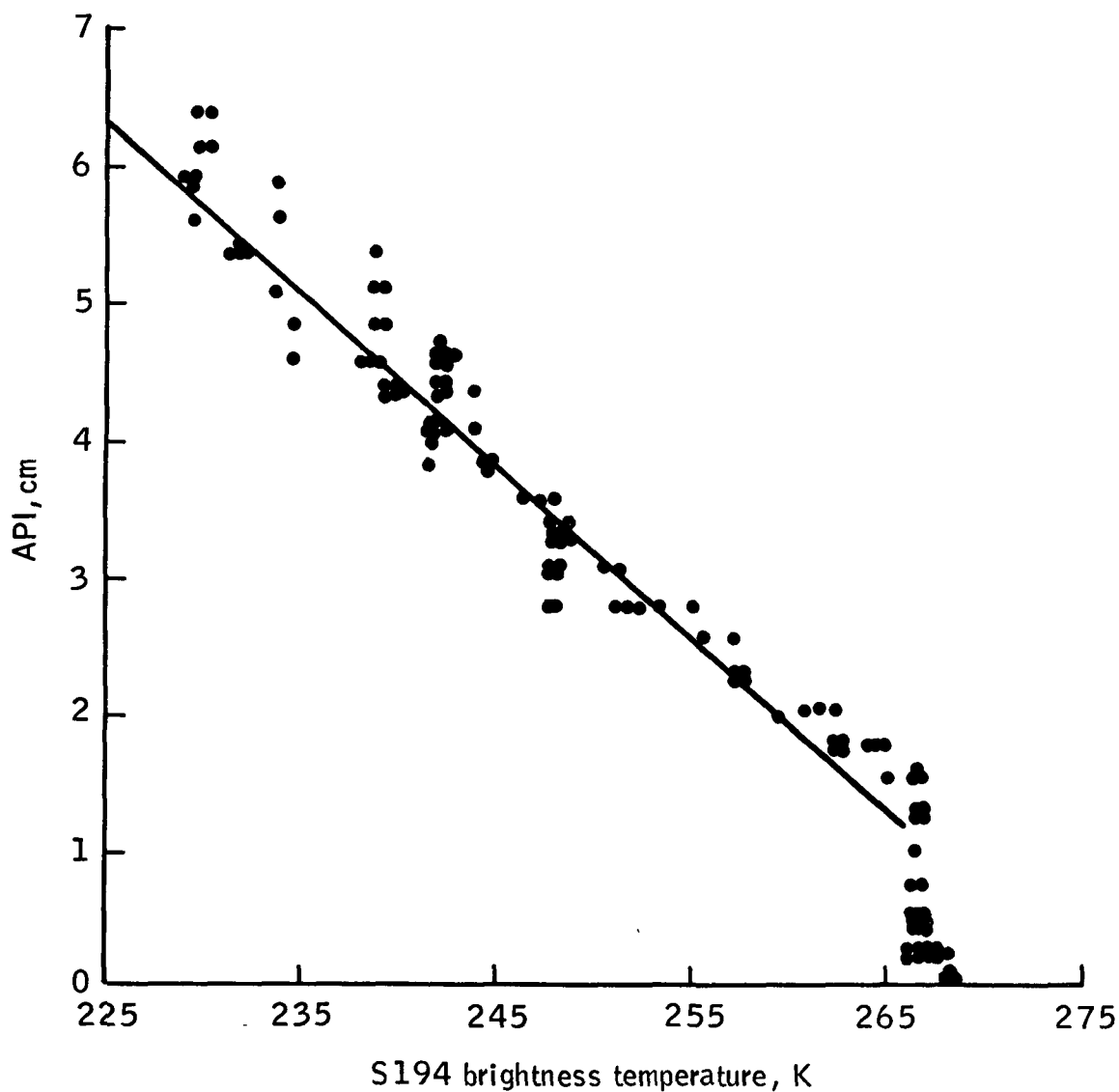


Figure 5-1.- The S194 L-band brightness temperatures compared to the averaged 11-day API and 5-day API for the footprint for June 11, 1973.



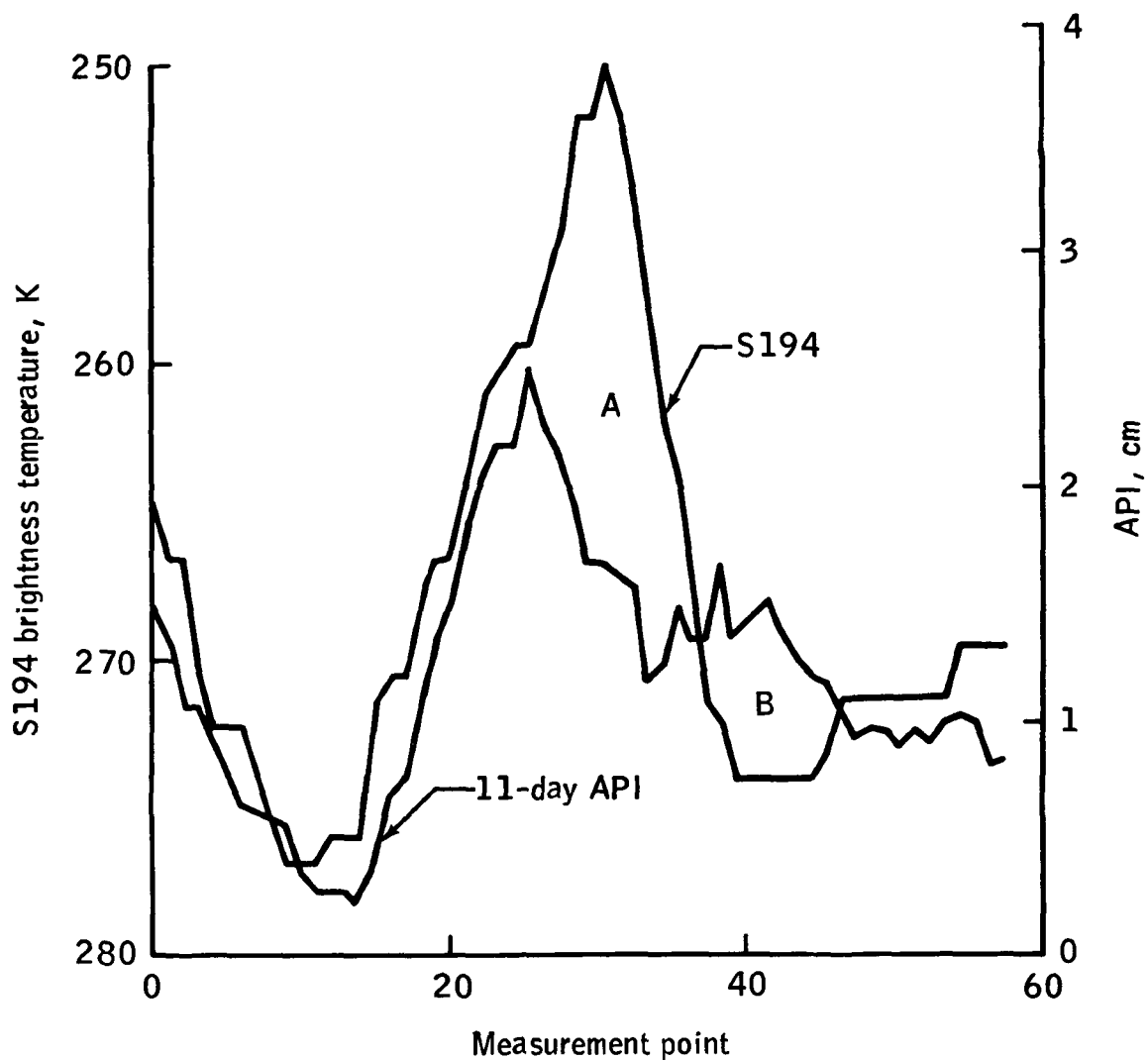


Figure 5-3.- The L-band brightness temperature from S194 and the averaged 11-day API for the footprint for August 8, 1973. Areas A and B indicate anomalous S194 brightness temperatures.

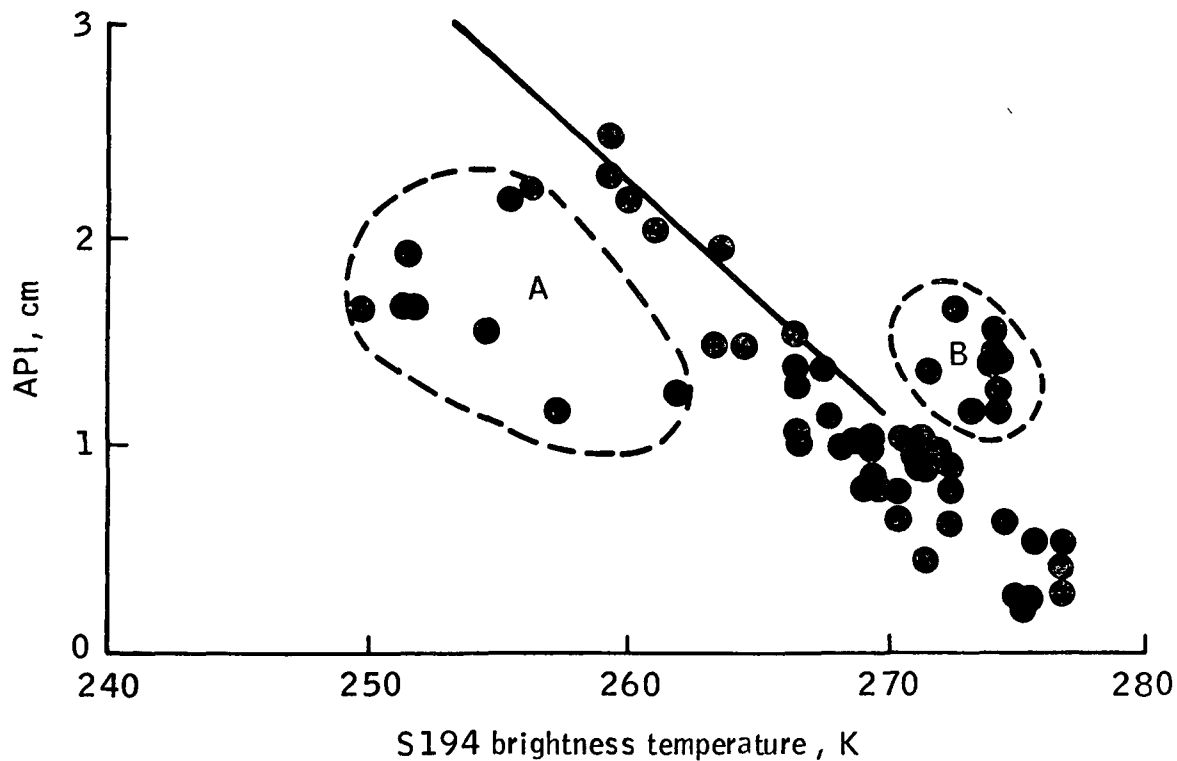


Figure 5-4.- Scatter plot of 11-day API compared to S194 brightness temperature (data from fig. 5-3). Areas A and B represent anomalous S194 brightness temperatures.

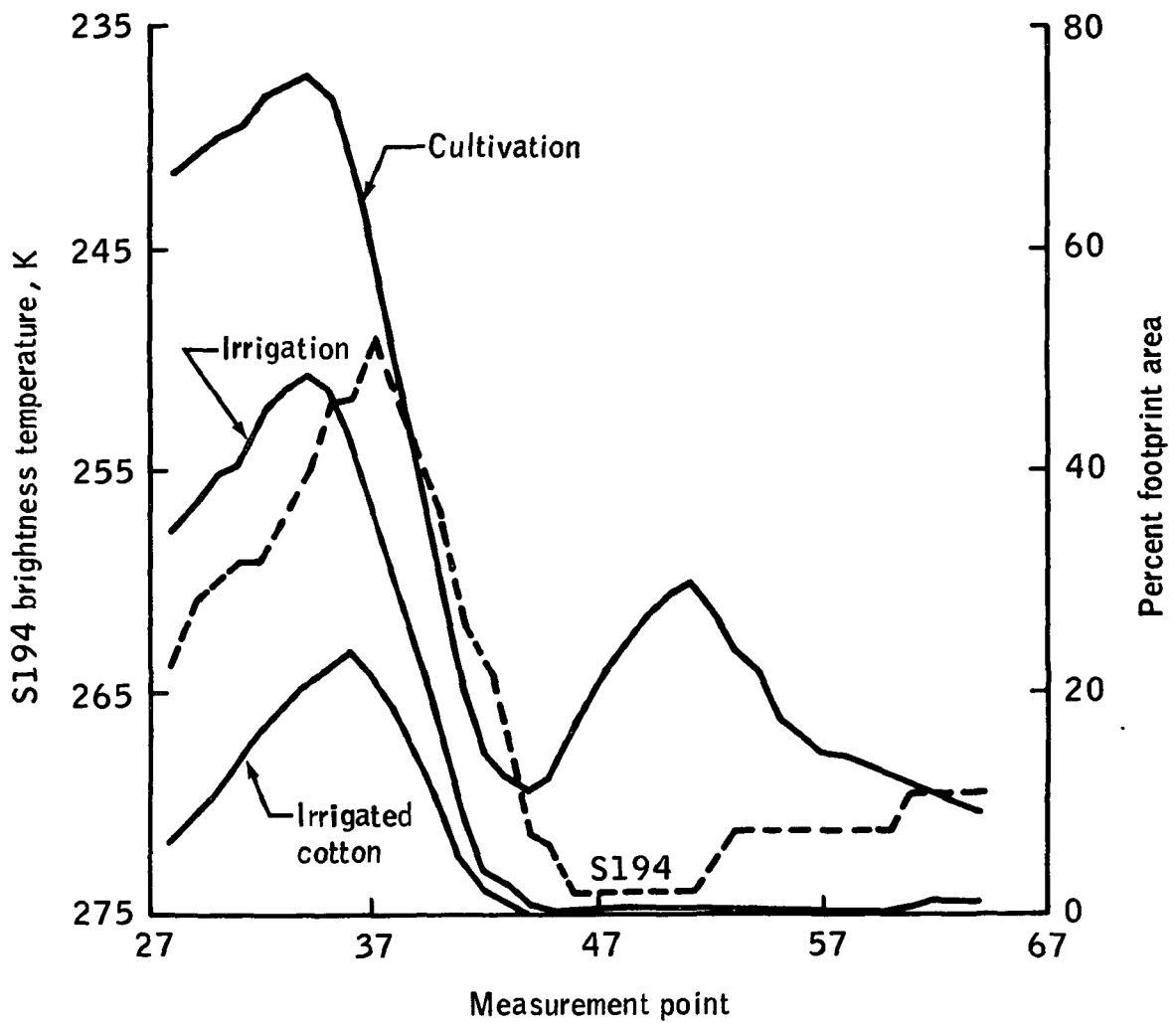


Figure 5-5.- Comparison of S194 data with land use.

6. SOIL MOISTURE STUDY USING THE S193 RADIOMETER

Bob E. Stucky^a

The Skylab 2 radiometer/scatterometer (RAD/SCAT) S193 experiment of June 11, 1973, provided 1085 discrete intrack measurements during the period from 10:17:56 to 10:19:19 central daylight time (c.d.t.). Scatterometer and radiometer measurements totaled 105 and 980, respectively. During data acquisition, 21 intrack contiguous (ITC) antenna scans were made with the initial scan reserved for scatterometer operations only. For each of the remaining 20 scans, 49 passive measurements were made at viewing angles intermediate to the five angles corresponding to active measurements. Angles of incidence ranged from 46.7° to 0.5° for each antenna scan, which, when coupled with the 439-kilometer altitude of Skylab, enabled almost contiguous ground coverage of approximately 500 kilometers for a single scan. The Skylab groundtrack with RAD/SCAT coverage is geographically shown in figure 6-1. Details of the S193 system and its potential for remote sensing of soil moisture are given in reference 6-1.

The computer plotter of the University of Oklahoma was used to produce a 1:1 000 000 Lambert conformal plot of sensor footprint ground positions. The plot was used as an overlay on an operational navigation chart (ONC) of the same 1:1 000 000 scale. The detailed ONC map provided a useful means of identifying surface features that may have contributed to sensor response. An additional plot of each footprint ground position was made to overlay an uncontrolled mosaic of enlarged, 70-millimeter, black-and-white infrared (0.7 to 0.8 micrometer) photographs from the S190A multispectral camera. The photographs correspond to the time of S193 data acquisition. This plot permitted the identification both of influential weather phenomena and of surface features not readily discernible on the ONC map. The scale of the enlarged S190A photographs was 1:821 000.

The study area was described in the previous section. Radar film furnished by the National Oceanic and Atmospheric Administration (NOAA) Climatological Center at the Greater Southwest Airport at Fort Worth was used to help identify the precipitating areas along the groundtrack on the S190 photographs. Contours of S193 apparent brightness temperatures relative to the individual thunderstorm cells are illustrated in figure 6-2.

^aLower Mississippi River Forecast Center, National Oceanic and Atmospheric Administration, Slidell, Louisiana. (Research sponsored by NASA Contract NAS 9-13360 and conducted at the University of Oklahoma.)

PRECIPITATION HISTORY

The precipitation history over the study areas was used to infer soil moisture conditions because direct soil moisture measurements were not available along the Skylab groundtrack. Moisture present in the soil depends on the relationship between precipitation and the complex process of evapotranspiration. A simple model that parameterizes soil moisture by incorporating precipitation history is the antecedent precipitation index (API). The API is defined (ref. 6-2) as

$$\text{API} = \sum_{i=1}^n K^i P_i \quad (6-1)$$

where P_i is the daily precipitation for each day from n days previous to the current day. The coefficient K^i is a recession factor in which the parameter K (a positive number less than unity) characterizes the ability of the soil to lose moisture through evapotranspiration. Typical values of K range from 0.85 to 0.95.

The relationship between API and microwave temperature was first investigated by McFarland (ref. 6-3) and is described in the preceding section. For basically the same precipitation data and for the identical Skylab groundtrack as used in this section, McFarland found an excellent linear correlation of -0.97 between Skylab S194 L-band radiometer (21.4-centimeter wavelength) apparent brightness temperatures and 11-day API values averaged over the large 115-kilometer-diameter S194 antenna footprint. The maximum daily rainfall allowed in his API calculations was arbitrarily set at 5.08 centimeters (2.0 inches) to eliminate the influence of very high daily rainfall; i.e., the amount of daily rainfall in excess of 5.08 centimeters should contribute primarily to surface runoff and should not appreciably change the moisture content of the soil. The value used for K in his API calculations was 0.9. These values established by McFarland are applied in the analysis presented here.

Antecedent precipitation indices were calculated for each of 145 daily reporting stations of the NOAA Climatological Network (refs. 6-4 and 6-5) distributed along the groundtrack. The precipitation history of each station for the 11-day period (June 1 to 11) preceding the Skylab pass was used. As shown in figure 6-3, the maximum number of stations receiving measurable precipitation (≥ 0.025 centimeter (0.01 inch)) for a specified day is 123 (85 percent of the stations) on June 2 (the 10th preceding day). Furthermore, 144 of the 145 stations reported measurable precipitation on at least one day during the 10-day period before the pass of Skylab (fig. 6-4). Only 17 stations received precipitation on the 11th preceding day (June 1) with rainfall amounts being generally less than 0.6 centimeter (0.25 inch). Therefore, it

is assumed that the preceding 10-day period (June 2 to 11) of precipitation should provide a better indication of the soil moisture distribution throughout the entire study area.

Two sets of API were then calculated for each station, one set for the preceding 10-day period (10-day API) and the other for the preceding 6-day period. Following an API weighting procedure to be discussed shortly, correlations of S193 apparent brightness temperatures with the two sets of API were made. The 6-day API set was used to determine whether a shorter precipitation history would result in better correlations. The 2- or 3-day period before the Skylab pass would have been better to use; however, few stations received precipitation during those periods (figs. 6-3 and 6-4).

To reduce data handling, only radiometer measurements made at average incidence angles of 0.596° , 9.849° , 19.893° , 29.845° , and 39.685° were used for correlation with API. Figure 6-5 shows the 20 apparent brightness temperatures for each of the five angles of incidence along the groundtrack. Possible causes for the pronounced relative maximums and minimums as determined from the ONC base map and the S190A photographs are also given in figure 6-5.

Because of the small S193 antenna footprint size (11-kilometer diameter at nadir) relative to station separation, weighted API values were used for correlation with S193 apparent brightness temperatures. A distant-dependent circular weighting function was used for determining the representative API coincident with each footprint center point. The distant-dependent weighting function is given as (ref. 6-6)

$$W_k = \frac{R^2 - d_k^2}{R^2 + d_k^2} \quad (6-2)$$

where R is the radius of influence about each footprint center point and d_k is the distance separating the k th reporting station and the footprint center point. The weight W_k is defined to be zero for $d_k \geq R$, forcing the weights to take on positive values between zero and unity for $d_k < R$. The radius of influence was chosen to be 57 kilometers, which permitted a minimum of three API values to fall within the circular region of influence. The radius of influence of 57 kilometers is equal to the radius of the S194 footprint used in the study by McFarland.

The weighted API values used for subsequent correlation with the S193 apparent brightness temperatures were calculated by

$$API = \frac{\sum_{k=1}^M w_k API_k}{\sum_{k=1}^M w_k} \quad (6-3)$$

where M is the number of daily reporting stations falling within each circular region of influence, and w_k and API_k are the weight and API, respectively, assigned to the k th station. In this study, $M \geq 3$.

RESULTS

Correlations of S193 apparent brightness temperature T_A , at each of the five angles of incidence, with both the 6-day and 10-day weighted API are shown in figure 6-6. There is a weak correlation (-0.26 to -0.51) between T_A and the 6-day API set at the given angles of incidence. As indicated in figure 6-3, only slightly more than 50 percent of the daily reporting stations received precipitation within the preceding 6-day period. Furthermore, rainfall was concentrated in the southern half of the study area, leaving much of the groundtrack free of precipitation during the preceding 6 days.

On the other hand, figure 6-6 shows a relatively strong correlation (-0.855) between nadir (0.593° incidence angle) S193 apparent brightness temperatures and the 10-day weighted API. Correlations are seen to deteriorate with increasing incidence angle. The linear least squares fit between the nadir T_A and the 10-day API is illustrated in figure 6-7. Apparent brightness temperatures less than 260 K were not included in the preceding correlations because of the strong influence of lakes (fig. 6-5).

The ability of the API to parameterize soil moisture is indicated by comparing the -0.855 correlation of figure 6-6 to the excellent -0.97 correlation (between the S194 L-band (21.4-centimeter wavelength) apparent brightness temperatures and the 11-day footprint-averaged API) determined by McFarland. From a theoretical viewpoint, the presence of vegetative cover tends to mask the dependence of the shorter emitted microwave wavelengths on soil moisture. Generous rains were common throughout the study area on the 10th day (June 2) preceding S193 data acquisition. Therefore, a reasonable assumption is that a considerable amount of new and increased vegetative growth should have

been present at the time of the Skylab pass. This would tend to reduce the influence of soil moisture on S193 apparent brightness temperatures, which implies that the comparatively weaker -0.855 correlation is consistent with past experiments related to direct soil moisture measurements (refs. 6-7 and 6-8). Another contributive factor is that a smaller skin depth is associated with the shorter 2.16-centimeter wavelength.

The effect of surface roughness on the S193 apparent brightness temperature is not readily apparent, although figures 6-5(a) to 6-5(d) indicate a slight increase in apparent brightness temperature due to the granite outcrop area in the Wichita Mountains of southwest Oklahoma. Because of the smaller S193 antenna footprint diameter of 11 kilometers, compared to the S194 footprint diameter of 115 kilometers, the S193 sensor would be more sensitive to small-scale variations in terrain roughness and vegetative cover; i.e., the larger S194 footprint effectively averages small-scale variations in surface roughness and vegetative cover. The comparison between S193 and S194 footprint center point values, as given in figure 6-8, suggests the greater sensitivity of the Ku-band sensor to such surface features as roughness and vegetation, factors that decrease soil moisture dependency.

As illustrated in figure 6-6, correlations degrade noticeably with angle of incidence. Vertically polarized apparent brightness temperatures increase with both angle of incidence and vegetative cover. Therefore, the heavily vegetated terrain of East Texas combined with the higher angles of incidence would logically reduce the T_A -API correlations. In addition, some areas along the groundtrack were experiencing light to moderate rainfall during the Skylab pass, further complicating the analysis.

The influence of precipitating thunderstorms on S193 apparent brightness temperatures is illustrated in figure 6-7 and in figures 6-5(a) to 6-5(e). It is readily apparent in these figures that relative minimums of S193 measurements are associated with areas of thunderstorm activity.

As indicated in figures 6-5(b) to 6-5(e) and in figure 6-7, significantly low S193 apparent brightness temperatures are obtained because of the presence of lake water. The low emissivity of lake water is responsible for these low S193 measurements, thereby illustrating the dominance of the surface emissive term. For the same reason, it is likely that surface water from precipitation in the vicinity of thunderstorm cells serves to reduce microwave emissions; however, the presence of surface water from precipitation along the Skylab groundtrack cannot be confirmed. Regions experiencing rainfall would presumably have lower emissivities because of the surface water of precipitation. Consequently, the low emissivities of wet terrain due to precipitation coupled with the higher emissivities of the background terrain, which did not receive rainfall, should account for the reduced S193 apparent brightness temperatures in the vicinity of thunderstorms. Thus, it appears that the Ku-band sensor is capable of detecting terrestrial radiation in the presence of light to moderate precipitation.

Theoretically, precipitation raises the apparent brightness temperature of the atmosphere T_A because of microwave absorption and re-emission by the

precipitation particles (refs. 6-9 and 6-10). Therefore, the measured apparent brightness temperature T_A would increase (momentarily neglecting surface effects) as a result of increased upward atmospheric emissions. (See equation (5-2) in section 5.) Consequently, a decrease in terrain microwave emissions because of the presence of precipitating thunderstorms illustrates the dominance of the multiplicative atmospheric transmissivity/surface emissivity term.

When areas of precipitation are being sensed at microwave frequencies, the importance of the background material may be further illustrated by considering precipitation falling on an ocean surface. The low emissivity of seawater provides a "cool" background with respect to areas of precipitation. Furthermore, precipitation striking the ocean surface (adding to the effect of surface winds) creates bubbling and foaming; these factors increase microwave emissions (ref. 6-11). Thus, a positive correlation between ocean surface emissivity and upward atmospheric emissions in areas of precipitation is evident, resulting in apparent brightness temperatures that are relatively higher in the vicinity of thunderstorms compared to the "cool" ocean background (refs. 6-12 to 6-14). Although the opposite effect is apparent over terrain, the same principle applies.

REFERENCES

- 6-1. Stucky, Bob E.: Analysis of Skylab S193 Apparent Brightness Temperature in a Thunderstorm Environment. M. S. Thesis, Univ. of Okla., 1975.
- 6-2. Linsley, Ray E., Jr.; Kohler, M. A.; and Paulhus, J. L. H.: Hydrology for Engineers. McGraw-Hill, 1958.
- 6-3. McFarland, M. J.: The Correlation of Skylab L-Band Brightness Temperatures With Antecedent Precipitation. WEAT Report 17, Atmospheric Research Laboratory, Univ. of Okla., 1975.
- 6-4. Climatological Data - Oklahoma, vol. 82, no. 6. NOAA Environmental Data Service, Asheville, N.C., 1973.
- 6-5. Climatological Data - Texas, vol. 78, no. 6. NOAA Environmental Data Service, Asheville, N.C., 1973.
- 6-6. Cressman, G. P.: An Operational Objective Analysis System. Monthly Weather Rev., vol. 87, 1959, pp. 367-374.
- 6-7. Eagleman, J. R.; and Ulaby, F. T.: Remote Sensing of Soil Moisture by Skylab Radiometer and Scatterometer Sensors. AAS Paper 74-146, Aug. 1974.
- 6-8. Newton, R. W.; Lee, S. L.; Rouse, J. W., Jr.; and Paris, J. F.: On the Feasibility of Remote Monitoring of Soil Moisture With Microwave Sensors. Proceedings of the Ninth International Symposium on Remote Sensing of Environment, Vol. I, Environmental Research Institute of Michigan, 1974, pp. 725-738.
- 6-9. Gunn, K. L. S.; and East, T. W. R.: The Microwave Properties of Precipitation Particles. Quart. J. Roy. Meteorol. Soc. (London), vol. 80, no. 346, 1954, pp. 522-545.
- 6-10. Weger, Eric: Apparent Sky Temperatures in the Microwave Region. J. Meteorol., vol. 17, no. 2, Apr. 1960, pp. 159-165.
- 6-11. Paris, Jack Frederick: Microwave Radiometry and Its Application to Marine Meteorology and Oceanography. Dept. of Oceanography, 69-IT, Texas A. & M. Univ., 1969.
- 6-12. Sabatini, R. R.; and Merritt, E. S.: The Nimbus EMSR and Its Application to Storm Detection. Final Report EPRF 51-0873-004, Environmental Protection Research Facility, U.S. Navy, Monterey, Calif., 1973.
- 6-13. Wilheit, T.; Theon, J.; Shenk, W. E.; and Allison, L.: Meteorological Interpretations of the Images From Nimbus 5 Electrically Scanned Microwave Radiometer. NASA TM X-70424, 1973.

- 6-14. Ross, D.; Au, B.; Brown, W.; and McFadden, J.: A Remote Sensing Study of Pacific Hurricane Ava. Proceedings of the Ninth International Symposium on Remote Sensing of Environment, Vol. I, Environmental Research Institute of Michigan, 1974, pp. 163-180.

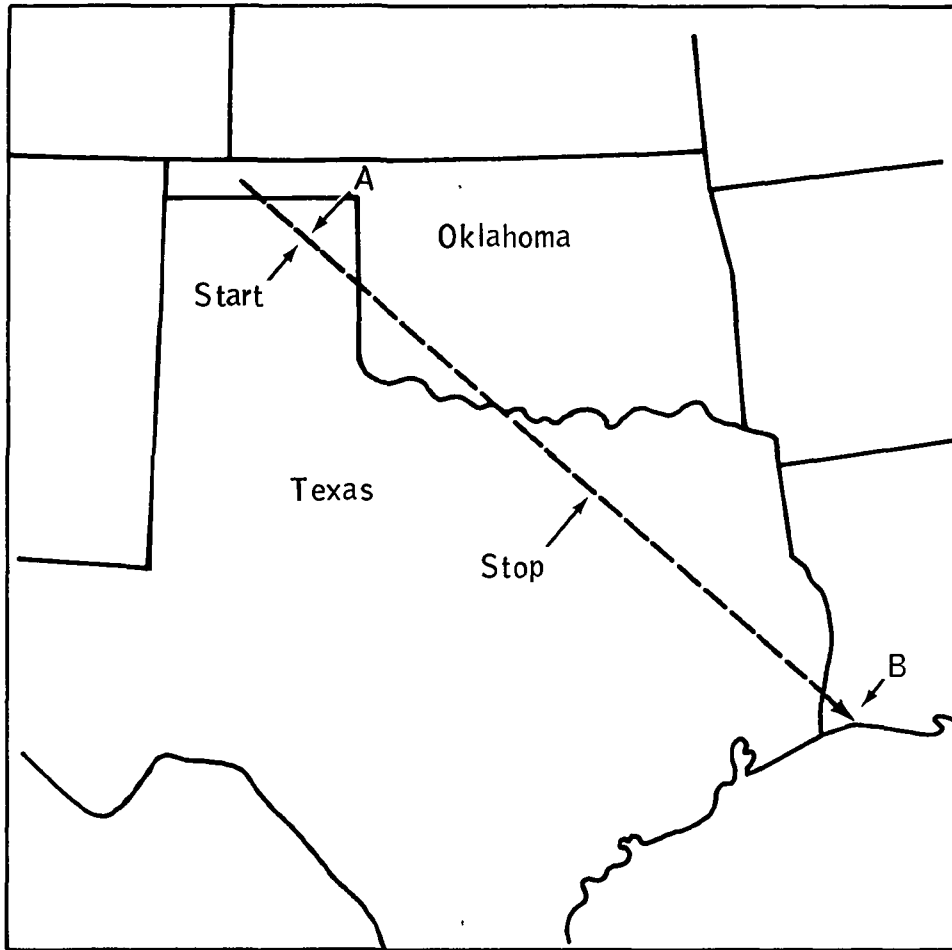


Figure 6-1.- Track of the RAD/SCAT footprints for groundtrack 48, pass 8, June 11, 1973.

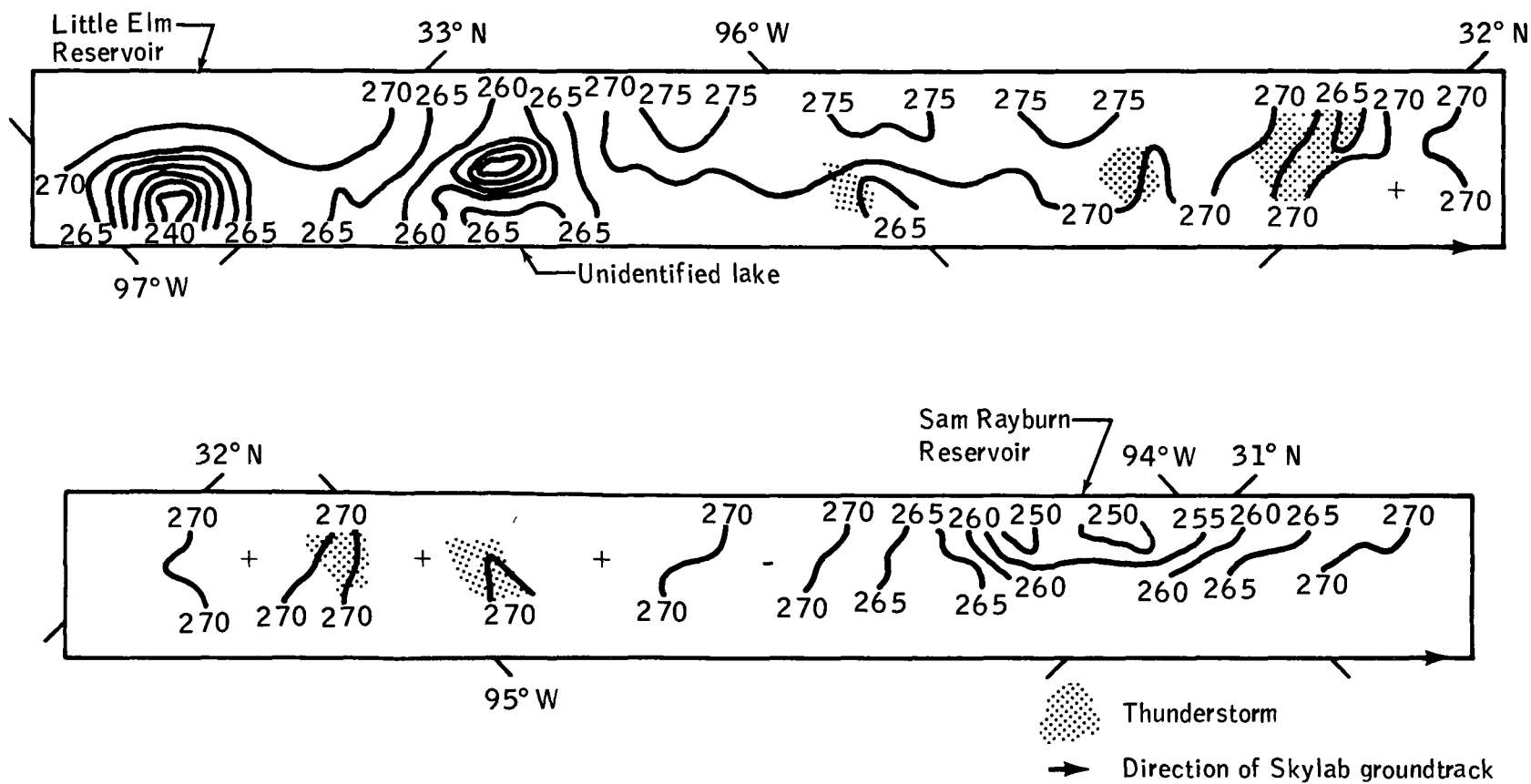


Figure 6-2.- Contours of S193 apparent brightness temperatures (in kelvin) covering the region from near Dallas to Louisiana.

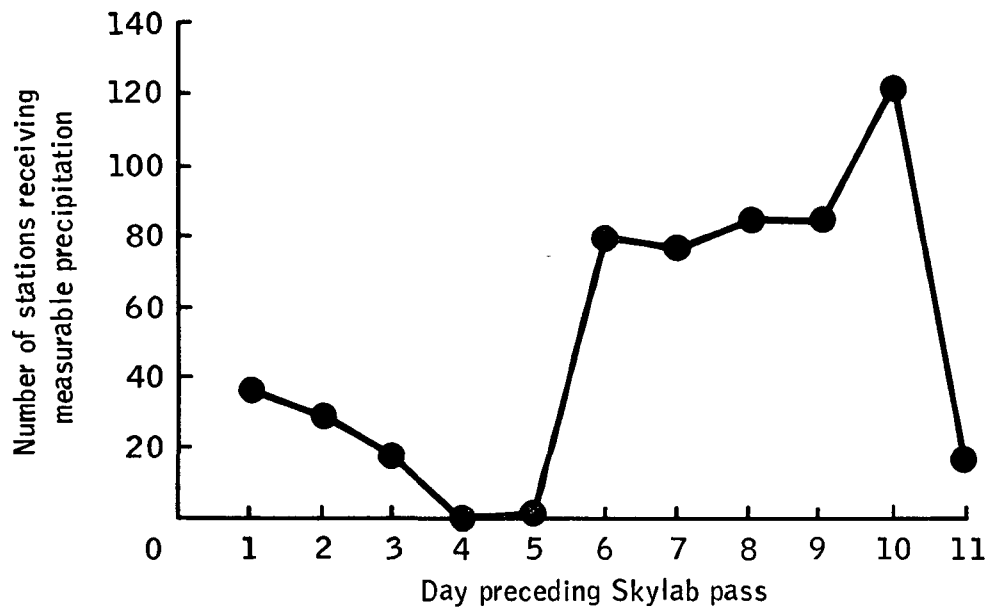


Figure 6-3.- The number of daily reporting stations receiving measurable precipitation on each of the 11 days preceding the Skylab pass.

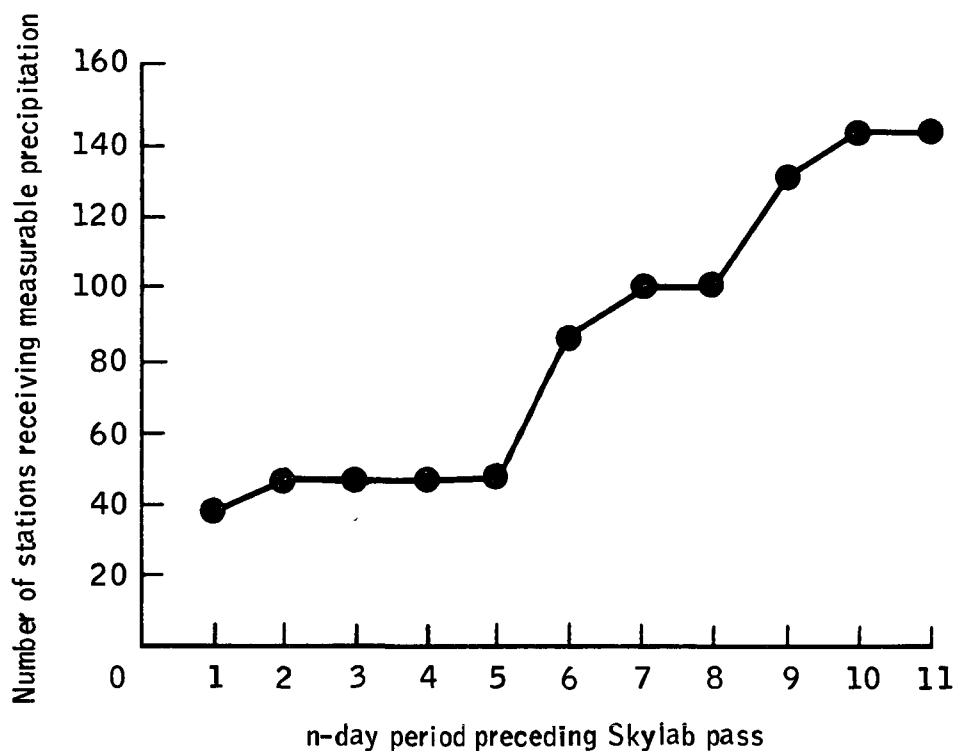
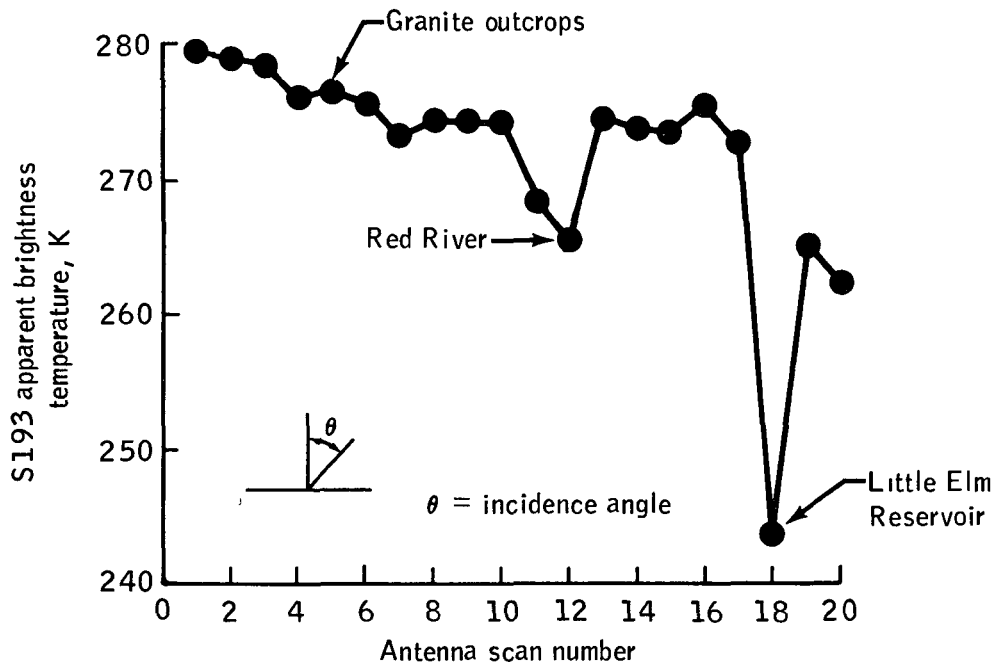
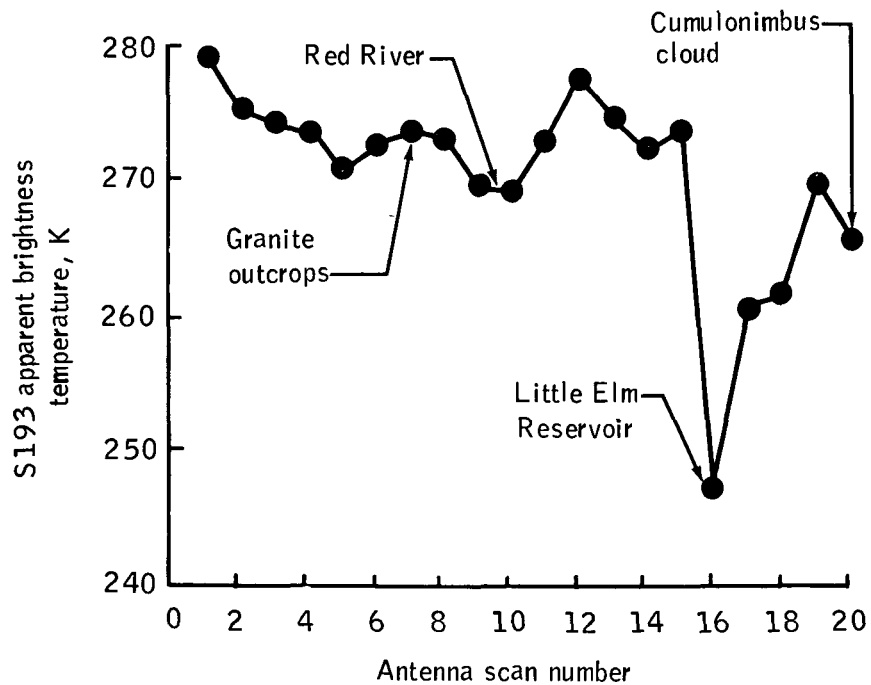


Figure 6-4.- The number of daily reporting stations receiving measurable precipitation on any given day during each consecutive n-day period preceding the Skylab pass.

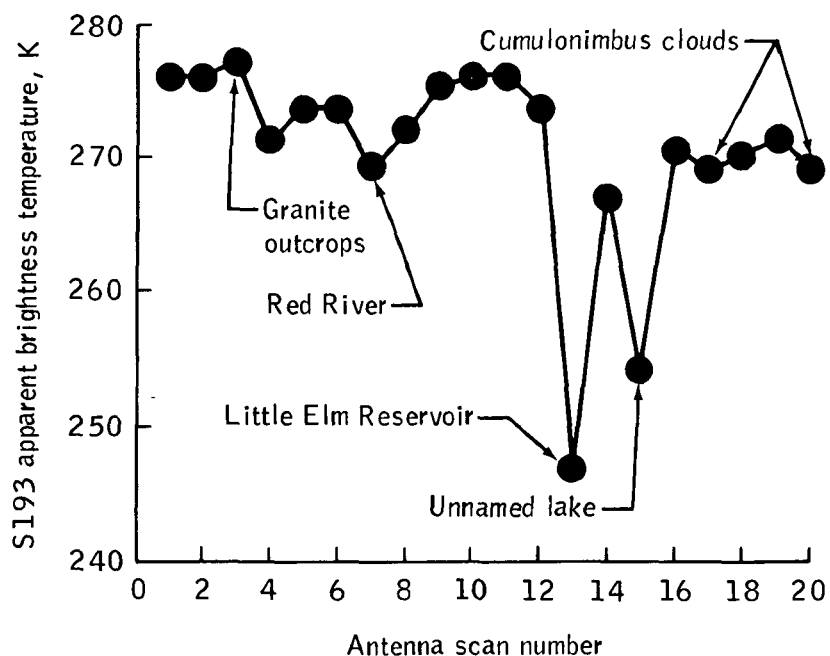


(a) Average incidence angle of 0.596° .

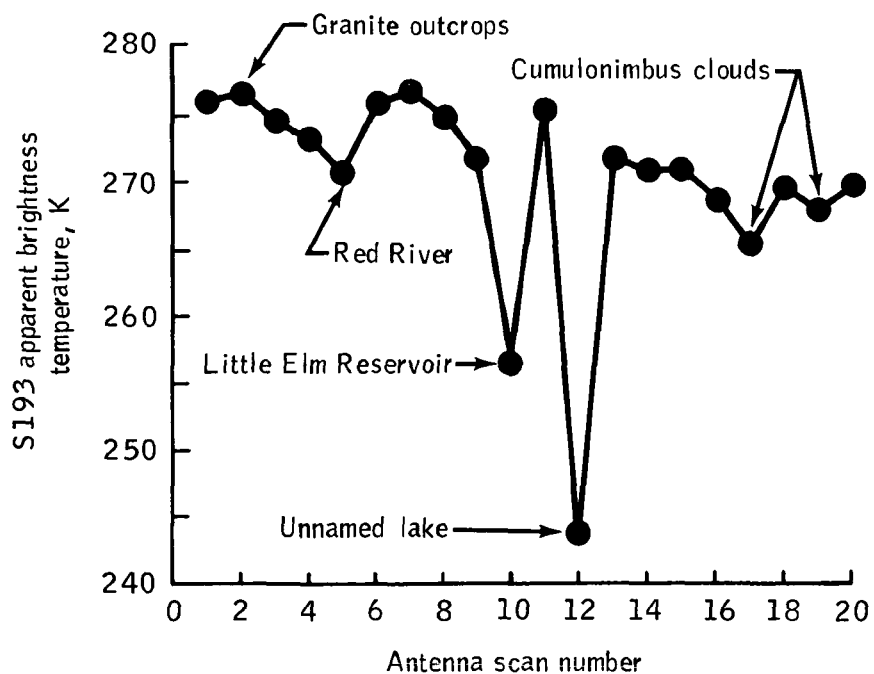


(b) Average incidence angle of 9.849° .

Figure 6-5.- S193 apparent brightness temperature for each of the 20 antenna scans.

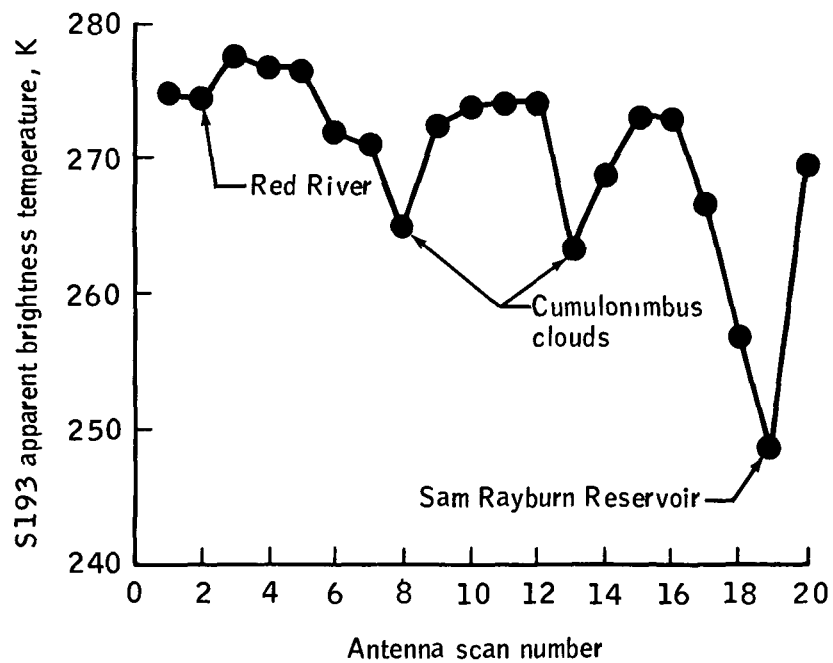


(c) Average incidence angle of 19.893° .



(d) Average incidence angle of 29.845° .

Figure 6-5.- Continued.



(e) Average incidence angle of 39.685° .

Figure 6-5.- Concluded.

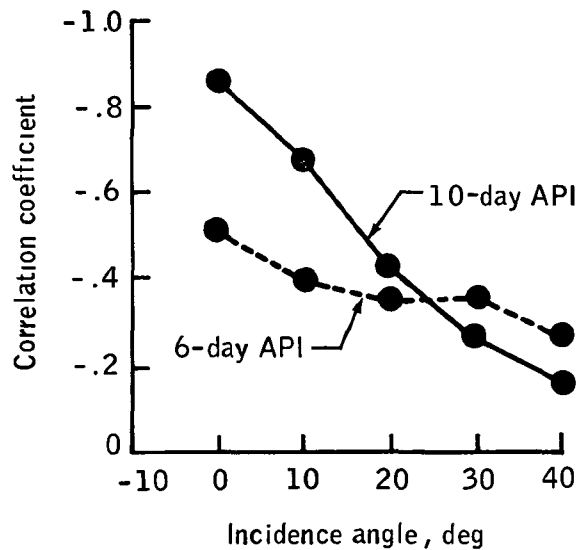


Figure 6-6.- Correlation of S193 apparent brightness temperatures with the 6-day and 10-day weighted API sets for each of the five angles of incidence shown in figure 6-5.

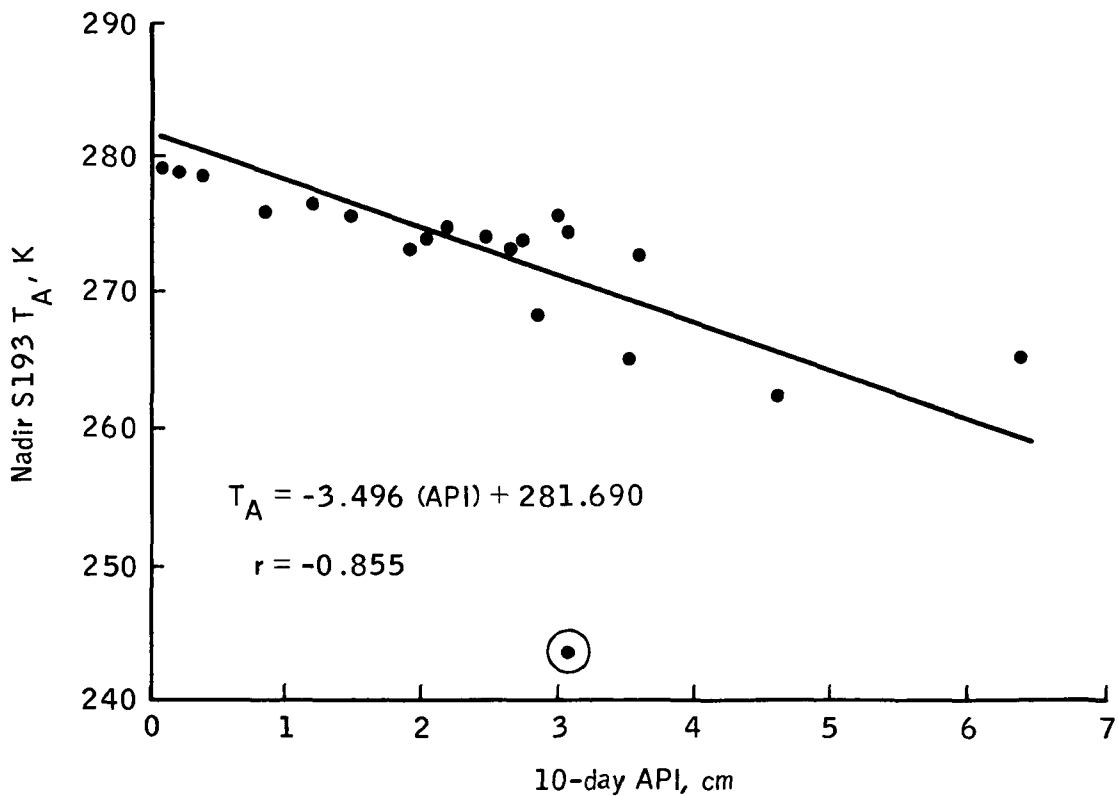


Figure 6-7.- Correlation of nadir (incidence angle = 0.596°) S193 T_A with the 10-day weighted API. The equation of the linear least squares line and the correlation coefficient r are shown. The circled datum was omitted because of pronounced lake influence.

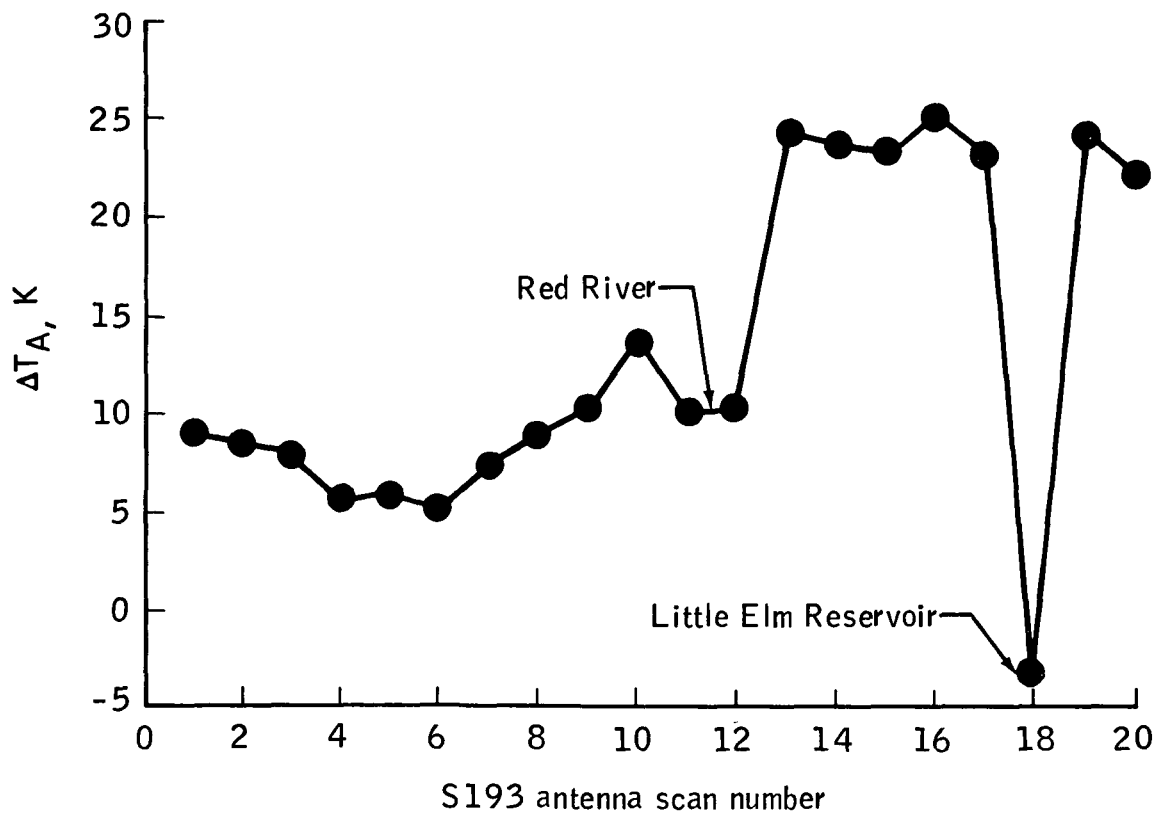


Figure 6-8.- The difference ΔT_A of coincident S193 T_A and S194 T_A footprint center point values ($\Delta T_A = S193T_A - S194T_A$).

7. S193 SCATTEROMETER CORRELATION WITH SOIL MOISTURE

Bob E. Stucky^a

In previous sections, it was shown that for the June 11, 1973, Skylab pass (groundtrack 48, Earth resources experiments package (EREP) pass 8) the S194 L-band radiometer antenna temperature was highly correlated with the antecedent precipitation index (API) and that the S193 radiometer/scatterometer antenna temperature had a slightly lower correlation. To determine whether the S193 scatterometer differential backscatter coefficient σ° is correlated with soil moisture, the backscatter coefficient was correlated with the antenna temperature T_A for S193. Figure 7-1 shows the approximate footprint size of the scatterometer for the 2.714° nadir angle. For this case, σ° at $\theta = 2.714^\circ$ is highly correlated (-0.949) with T_A . Figure 7-2 gives the linear least squares fit between T_A and σ° for this angle of incidence. The average closest distance separating T_A and σ° pairs of footprints was 1.089 kilometers with a standard deviation of 0.449 kilometer. The maximum separation between footprints was 2.239 kilometers and the minimum was 0.189 kilometer. The average nadir angle θ associated with T_A was 5.153° with a standard deviation of 4.460° , and the T_A angle σ° ranged from 14.308° to 1.397° . Figure 7-3 shows the response of both the radiometer and the scatterometer at 2.714° for each scan along the groundtrack. Figure 7-4 shows that the correlation between T_A and σ° decreases linearly and the incidence angle θ increases.

There was no apparent relationship between T_A and θ ; however σ° does depend on θ as illustrated in figure 7-5. Thus, the decrease in relationship between T_A and σ° for increasing θ suggests that the atmosphere and terrain are more reflective with respect to σ° .

The K-band scatterometer appears to have a high correlation with soil moisture for a near-vertical incidence angle from the spacecraft. At angles more than 17° off nadir, the correlation is low enough to prevent the use of the scatterometer for this purpose. At present, no advantage is evident in the use of the scatterometer instead of the passive radiometer for the detection of soil moisture.

^aLower Mississippi River Forecast Center, National Oceanic and Atmospheric Administration, Slidell, Louisiana. (Research sponsored by NASA Contract NAS 9-13360 and conducted at the University of Oklahoma.)

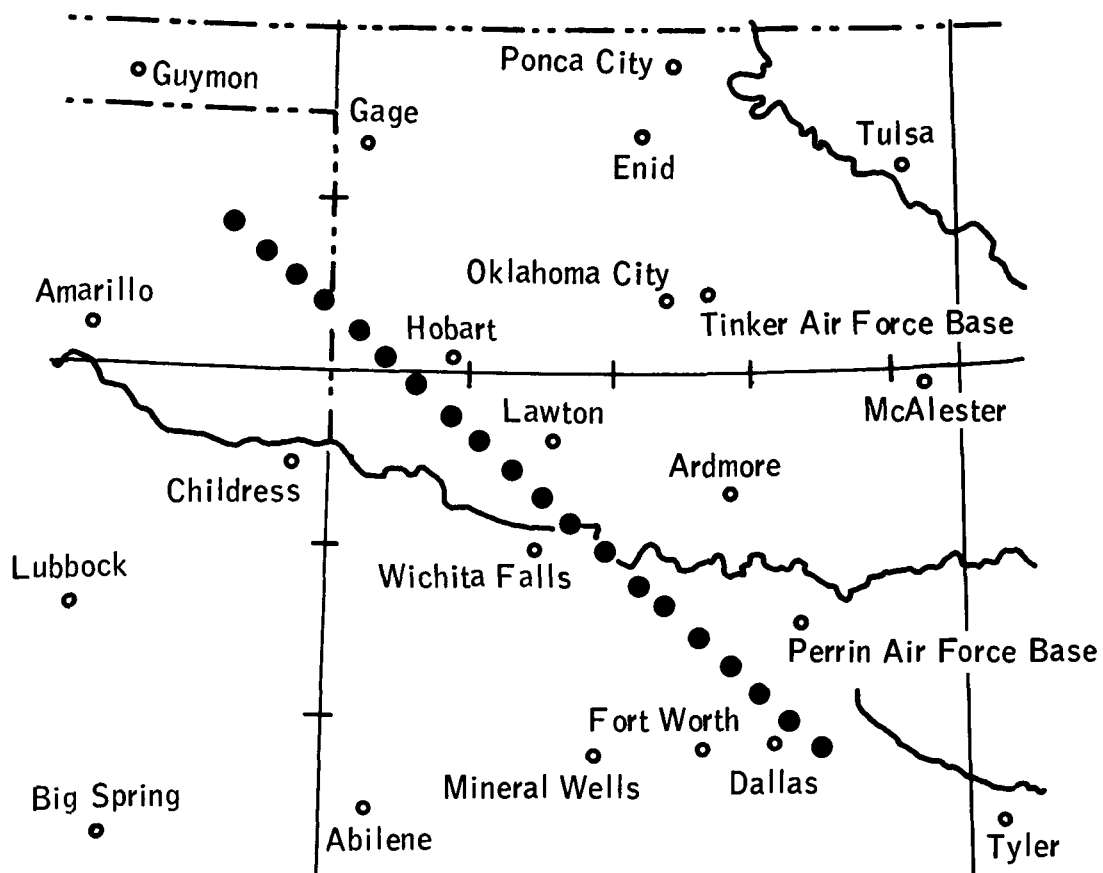


Figure 7-1.- Footprints of the S193 scatterometer for groundtrack 48 on June 11, 1973, at an incidence angle of 2.714° .

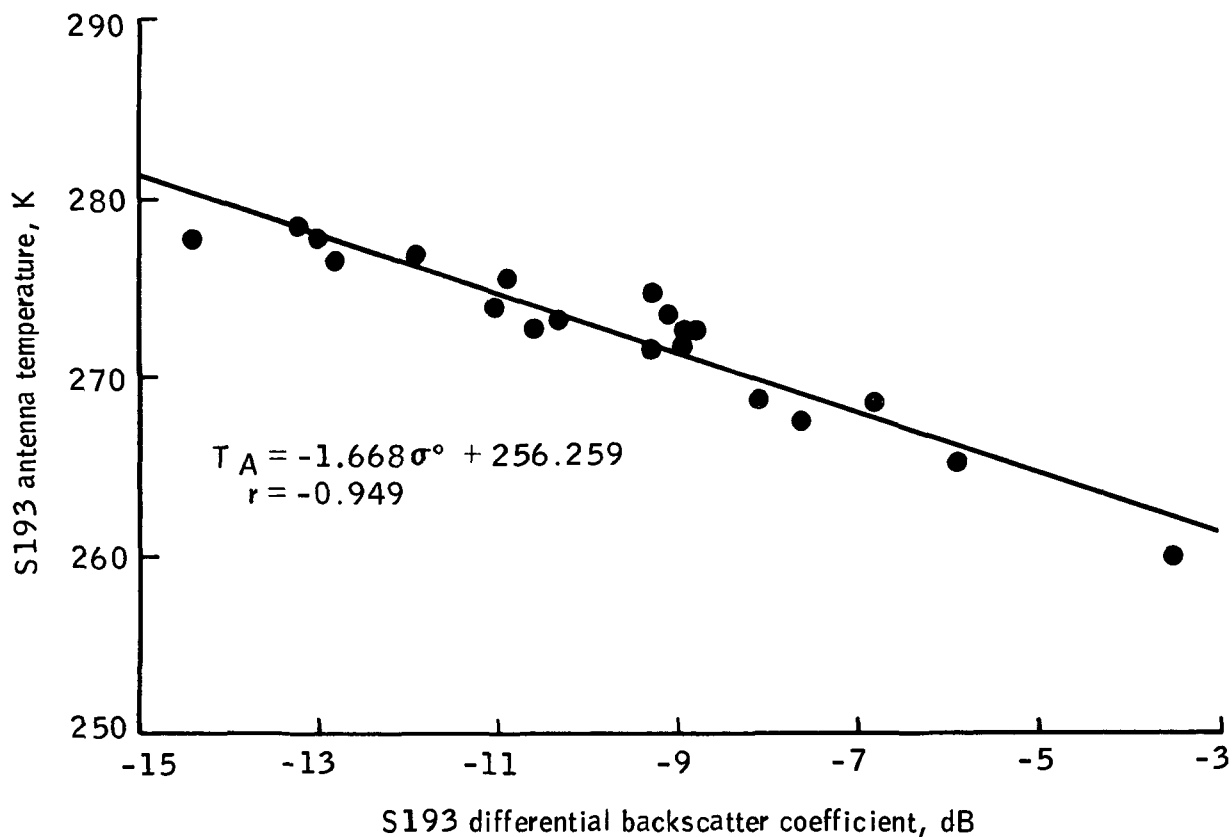


Figure 7-2.- Plot of S193 antenna temperature T_A and differential backscatter coefficient σ° with the least squares linear fit between the two parameters (r = correlation coefficient).

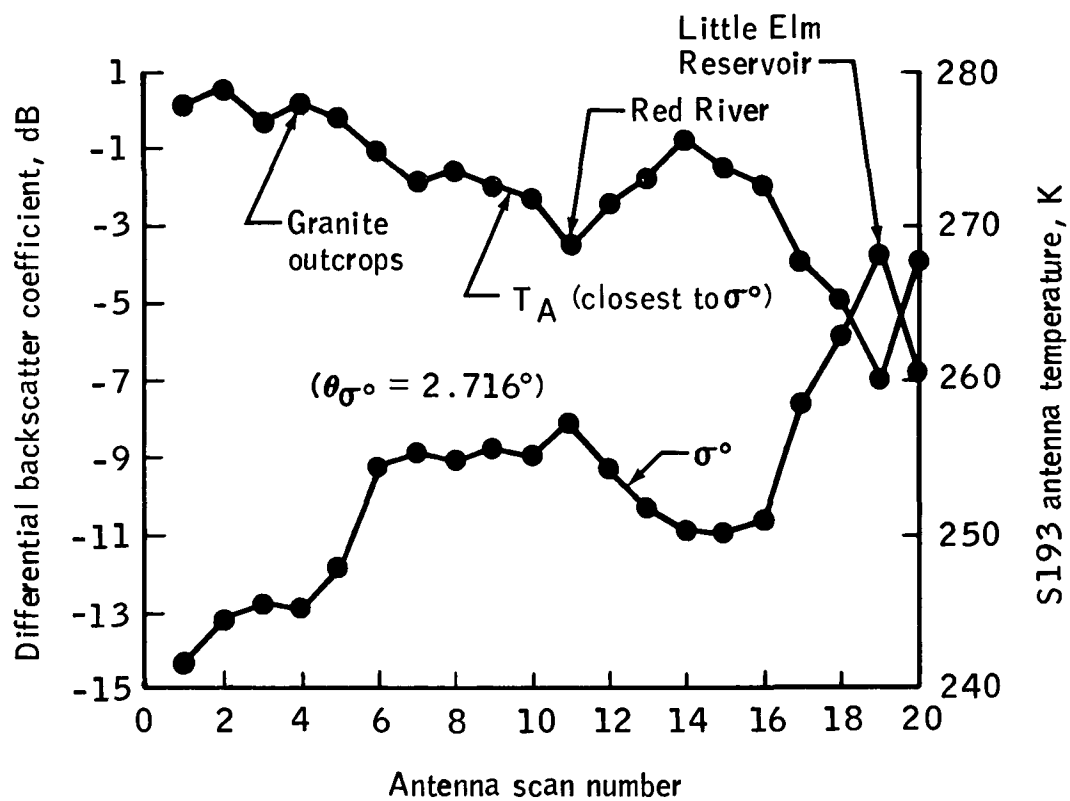


Figure 7-3.- Plot of S193 antenna temperature T_A and S193 differential backscatter coefficient σ° for each scan.

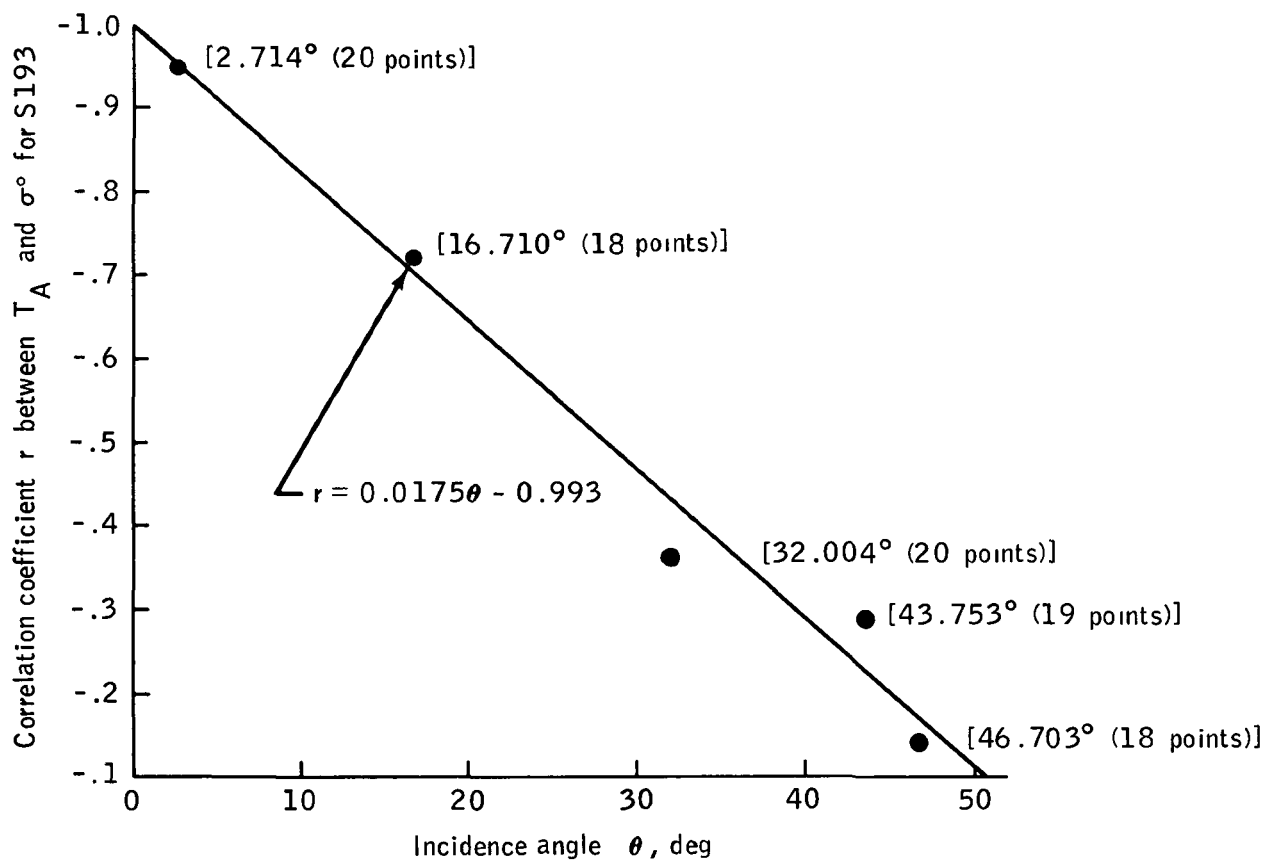


Figure 7-4.- Plot of correlation coefficient r as a function of incidence angle θ for S193. The correlation coefficient between r and θ was 0.9877. Numbers in brackets indicate the incidence angle and the number of data points involved.

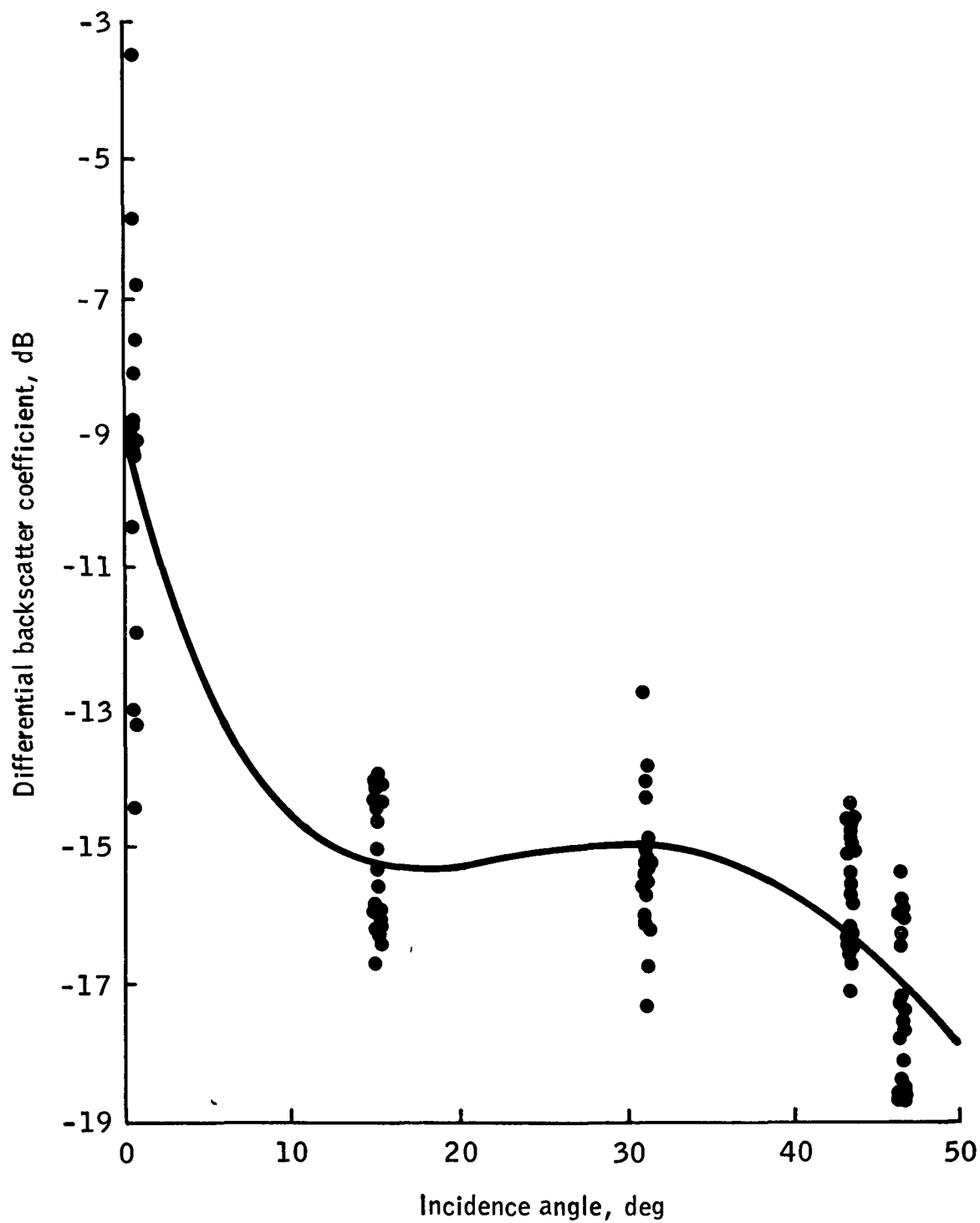


Figure 7-5.- Plot of all scatterometer data for EREP pass 8, June 11, 1973, together with least squares polynomial (third order) fit for the plot.

8. RECTIFICATION OF A WHOLE-SKY PHOTOGRAPH AS A TOOL FOR DETERMINING SPATIAL POSITIONING OF CUMULUS CLOUDS

Bob E. Stucky^a

INTRODUCTION

The purpose of this section is to investigate the whole-sky photograph as a reliable instrument for determining real-space positioning of cumulus clouds. Once reliability of spatial positioning is established, the whole-sky photographs may become a valuable asset to squall-line dynamics studies, boundary layer theory, and other related phenomena.

Lund et al. (refs. 8-1 to 8-4) and Rapp et al. (ref. 8-5) used the whole-sky photograph for estimating probabilities of cloud-free lines of sight through the atmosphere as a function of zenith angles and sky coverage (coverage in tenths as reported by the National Weather Service).

DATA ANALYSIS PROCEDURE

On June 11, 1973, whole-sky photographs were taken from a small watercraft on Lake Altus, Oklahoma (latitude 35°55' N, longitude 99°17' W), during the approximate pass-time of Skylab 2 (June 11, pass 8, groundtrack 48). The Nikon camera was set with an aperture of f/8, an exposure time of 1/125 second, and a fixed focus for infinity. Reference 8-6 describes the analysis of these data in detail.

A selected whole-sky color negative (fig. 8-1) was enlarged to fit a 20-by 25-centimeter (standard 8 by 10 inch) photographic print. The resultant circular positive print had a diameter of 20.6 centimeters with a negative enlargement of 8.96X.

A plastic transparency containing 10° increments of azimuth and zenith angles was fitted to the circular print. The diameter of the transparency was such that the 90° zenith angle circumscribed the outermost diameter of the circular positive print. An example of the plastic template used is shown in figure 8-2.

^aLower Mississippi River Forecast Center, National Oceanic and Atmospheric Administration, Slidell, Louisiana. (Research sponsored by NASA Contract NAS9-13360 and conducted at the University of Oklahoma.)

True north was determined on the whole-sky photograph by application of solar azimuth and elevation angles and by proper alinement of small mountain peaks surrounding the lake. Then the base size and relative distances from the camera of the selected cumulus clouds were determined by measuring their zenith and azimuth angles.

Frame 15-31 of color positive infrared film from the S190A multispectral camera (taken from Skylab 2 at 10:18:30 central daylight time (c.d.t.)) was used as reference for the whole-sky photograph. The highly sensitive S190A photographic system and its high resolution (30-meter class) allowed an enlargement to 40X (fig. 8-3) of the Lake Altus area. The resulting scale of the 40X enlargement was 1:71 304. The whole-sky photograph taken closest in time to the Skylab pass-time was selected for the single case study.

Two immediate problems were encountered: the center of the whole-sky photograph did not represent true zenith, and the exposure time of the whole-sky negative was at 10:20 c.d.t., resulting in a 90-second lag from the Skylab 2 pass-time. The former required only a small adjustment. The latter was adjusted by translation of the fisheye coordinate system (on the 40X enlargement) at a velocity vector equal to mean wind at an altitude of 335 meters, with a magnitude of 9 m/sec from 200°. An upper air sounding taken 90 kilometers to the east within a few minutes of the pass-time of Skylab 2 and hourly surface reports were used to determine the altitude of the cumulus cloud bases (near 335 meters) and the winds at cloud base level.

The selected individual cumulus clouds with their respective base size and relative distance from the camera (as determined from the whole-sky photograph) were then mapped onto the S190A 40X enlargement, and comparisons between the two cloud distributions were made.

RESULTS

The comparison between the whole-sky photograph and the S190A enlargement was not as satisfactory as was originally anticipated. Figure 8-4 displays the two photographically compared cumulus cloud distributions, a result of mapping the predetermined cloud base dimensions from the whole-sky photograph onto the enlarged S190A print (hatched areas represent selected cumulus clouds from the whole-sky photograph). As shown in figure 8-4, the adjusted position of the camera's coordinates is due to the 90-second time differential, resulting in a 0.81-kilometer displacement from its original location. As indicated, pattern similarity between the two distributions is weak.

The apparent failure to identify the same cloud base on the two differing photographs is primarily due to the following three major types of errors.

1. Inaccuracy of the subjectively determined cloud base heights and locations

2. Use of a nonsynchronized timing system

3. Rapid formation and dissipation of individual cumulus clouds that can occur during time intervals of 1 to 5 minutes

The cloud bases were assumed to have rectangular images on the whole-sky print, which should have produced only minor effects upon total analysis error. It was further assumed that errors caused by estimating cloud base elevations (335 meters) and the mean wind (9 m/sec from 200°) at cloud base level were insignificant to the final analysis.

Lack of a synchronized timing system between the ground and the Skylab orbital workshop appears to account for a major portion of the total analysis error. This deficiency required the translation of the whole-sky coordinate system, thus introducing additional errors associated with rapid formation and dissipation of individual cumulus clouds during the 90-second time differential.

Because the reliability of the time (10:20 c.d.t.) of whole-sky exposure was questioned, a visual trial-and-error technique was attempted by which the whole-sky coordinate system was readjusted to different locations on the S190A photograph until a better cloud-to-cloud identification pattern resulted. The readjustment was constrained to the general direction of the previously used mean wind (at cloud base level). Figure 8-5 displays a better correlated cloud identification pattern 6.3 minutes after the first analysis.

The major problem associated with both the initial and later time lags is the likelihood of rapid formation and dissipation of cumulus clouds during a short time interval. An excellent example of this is shown in figure 8-6. The selected cumulus cloud as shown in figure 8-6 was traced from whole-sky photographs exposed at 5-minute increments on July 6, 1974. Particular notice should be given to the rapid growth during the first 5-minute timespan, and again the rapid dissipation during the 15- and 20-minute elapsed times.

Figure 8-6 indicates the need of a synchronized timing system when viewing cloud structures from two separate platforms. The lack of synchronization had a pronounced effect upon the transitional nature of the whole-sky coordinate system to fit the S190A time frame, and this characteristic is believed to have been the major contributing factor to the final analysis.

The point to be made about rapid formation and dissipation of cumulus clouds is that the camera location for the initial translation may have, in fact, been accurately identified; but, because of rapid changes in individual clouds, they are no longer identifiable after an elapsed time as short as 90 seconds.

High, thin cirrus clouds were also present on the whole-sky photograph, resulting in some resolution loss caused by scattering of solar radiation. This presented the definition of accurate cloud base altitudes for those clouds located in the quadrant of the Sun. Another disadvantage was most of the cumulus clouds were located in the lower 30° of elevation, thus decreasing their image base size and increasing measurement errors. In general, image measurement error may be further increased when both cloud and Sun are in opposite quadrants and both have low elevation angles, which are due to alterations in the luminous character of the cloud base.

While this single case study produced less than satisfactory results, this certainly does not discount the valuable nature of the whole-sky photograph and its useful application to determine spatial positioning of cumulus clouds by providing total sky coverage. The data collection procedure and not the whole-sky camera appears to have accounted for the unsatisfactory analysis.

REFERENCES

- 8-1. Lund, Iver A.; and Shanklin, Milton D.: Photogrammetrically Determined Cloud-Free Lines-of-Sight Through the Atmosphere. J. Appl. Meteorol., vol. 11, no. 5, Aug. 1972, pp. 773-782.
- 8-2. Lund, Iver A.; and Shanklin, Milton D.: Universal Methods for Estimating Probabilities of Cloud-Free Lines-of-Sight Through the Atmosphere. J. Appl. Meteorol., vol. 12, no. 1, Feb. 1973, pp. 28-35.
- 8-3. Lund, Iver A.: A Model for Estimating Joint Probabilities of Cloud-Free Lines-of-Sight Through the Atmosphere. J. Appl. Meteorol., vol. 12, no. 6, Sept. 1973, pp. 1040-1043.
- 8-4. Lund, Iver A.: Persistence and Recurrence Probabilities of Cloud-Free and Cloudy Lines-of-Sight Through the Atmosphere. J. Appl. Meteorol., vol. 12, no. 7, Oct. 1973, pp. 1222-1228.
- 8-5. Rapp, R. R.; Schultz, C.; and Rodriguez, E.: Cloud-Free Line-of-Sight Calculations. J. Appl. Meteorol., vol. 12, no. 3, April 1973, pp. 484-493.
- 8-6. Stucky, Bob E.: Rectification of a Whole-Sky Photograph as a Tool for Determining Spatial Positioning of Cumulus Clouds. WEAT Report 18 (NASA Contract NAS9-13360), Univ. of Okla., April 1975.

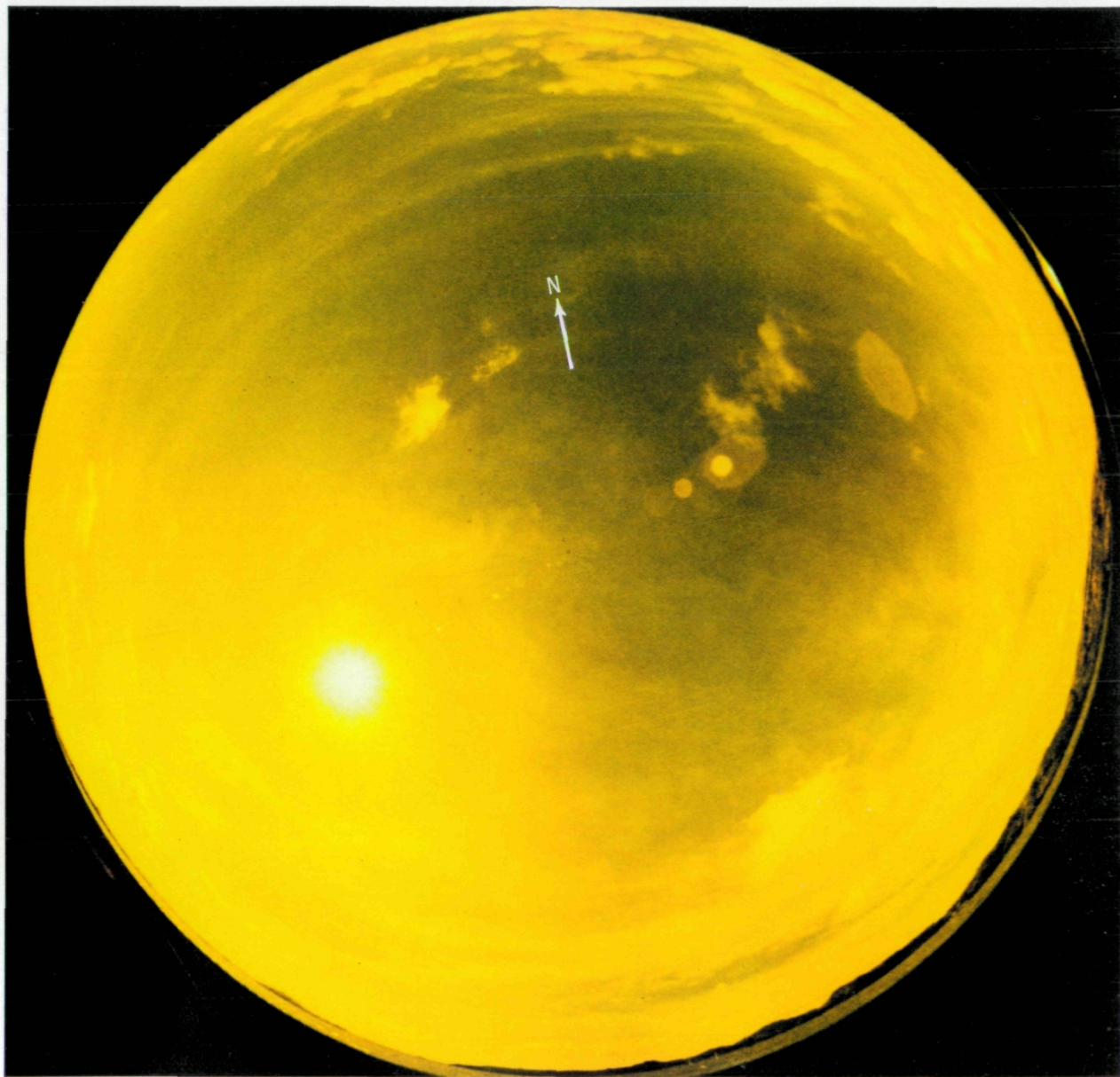


Figure 8-1.- Whole-sky photograph over Oklahoma used in this study.

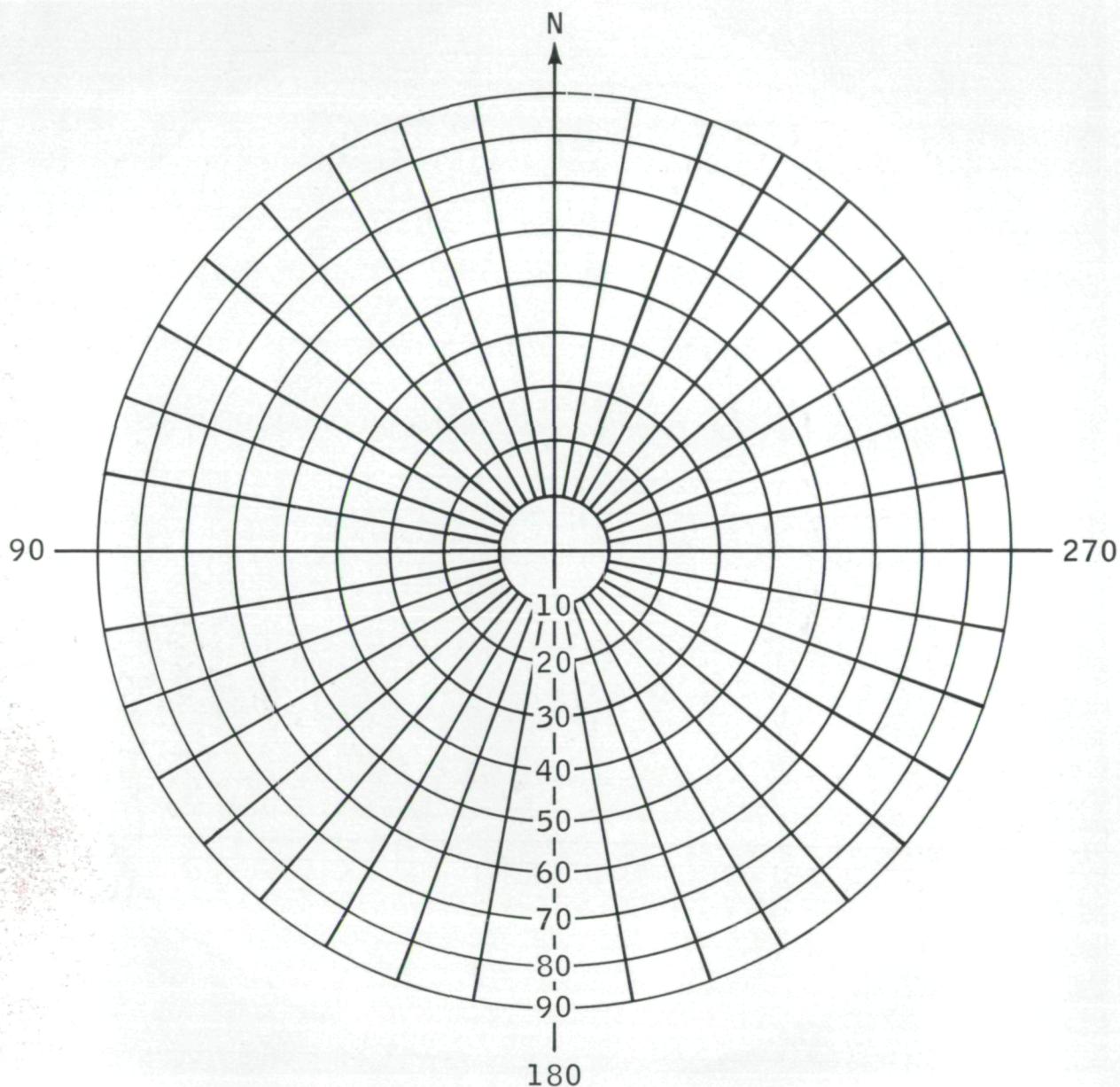


Figure 8-2.- Diagram of the plastic transparency used as an overlay for the whole-sky photograph. The zenith and principal azimuthal angles are shown. Particular attention should be given to the counterclockwise arrangement of the azimuth angles.

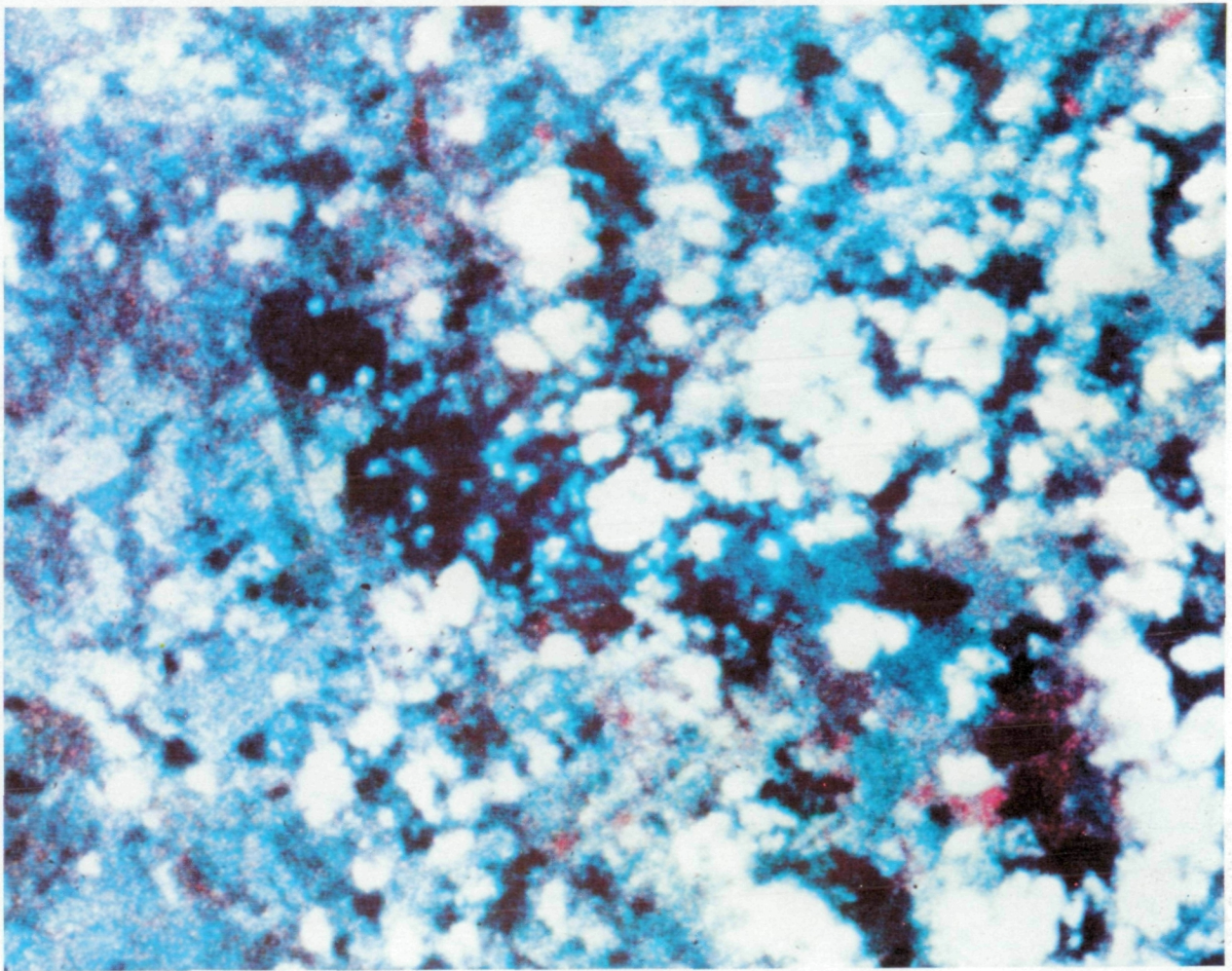


Figure 8-3.- Color-infrared frame of Lake Altus, Oklahoma, taken with the S190A on June 11, 1973.

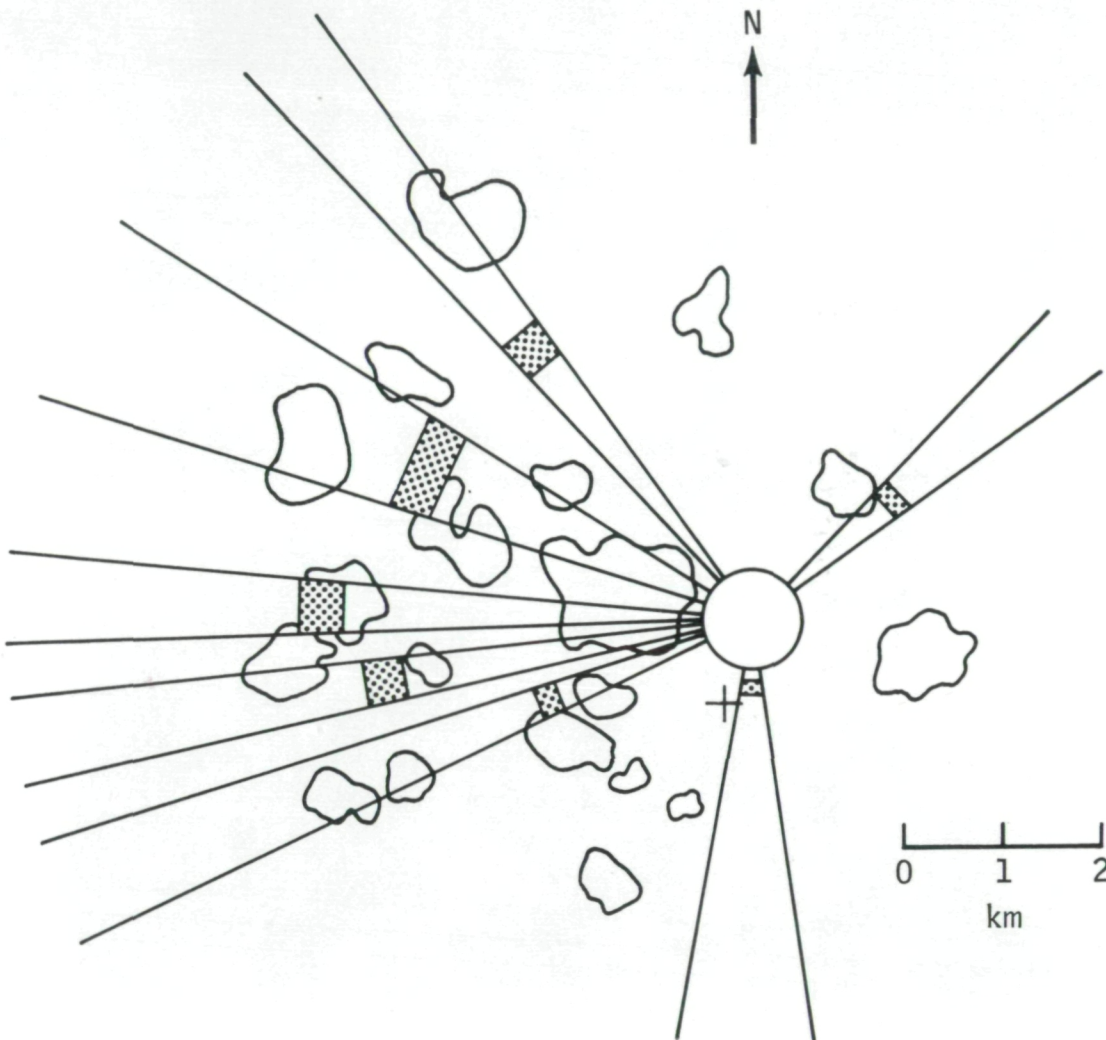


Figure 8-4. - Comparative distributions of the selected cumulus clouds constrained to the camera's initial transitory time of 90 seconds. The hatched areas correspond to the whole-sky distribution together with the fields of view for the individual cumulus clouds. The + represents the position of the camera before translation. A poor correlation between the two distributions exists in this instance.

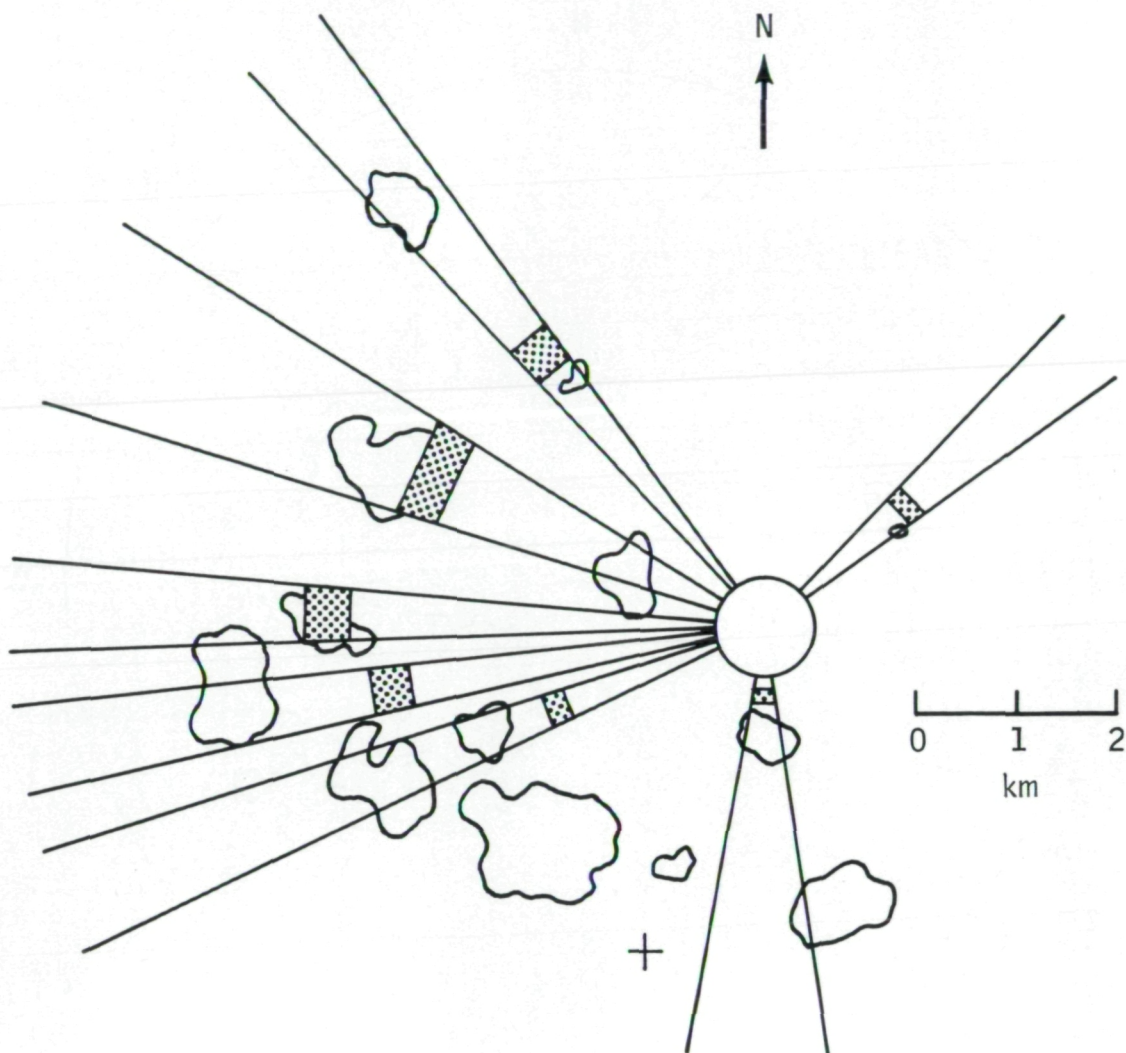


Figure 8-5.- Comparative distributions of the selected cumulus clouds constrained to the camera's secondary transitory time period. The hatched areas correspond to the whole-sky distribution together with the fields of view for the individual cumulus clouds. The + represents the camera position before translation. A much better correlation exists here than in figure 8-4.



Figure 8-6.- An example of rapid formation and dissipation characteristics for a single cumulus cloud during short-time exposure intervals of 5 minutes. The cloud did not exist during sky exposure 5 minutes later than its number 4 position. The cloud was exposed by the whole-sky camera.

9. SEVERE STORM CLOUD-TOP CHARACTERISTICS

David E. Pitts,^a J. T. Lee,^b and W. Johnson^c

AUGUST 8 DATA

On August 8, 1973, the Earth resources experiment package (EREP) on Skylab was used to conduct an experiment to measure the equivalent black-body temperature of the top of a severe storm and to determine spectral characteristics in the visible and near-infrared wavelengths that would be useful in predicting subsequent storm evolution. The storm was located over the Gulf of Mexico (fig. 1-1 in section 1) about 190 kilometers south of Beaumont, Texas, at latitude 28°04.1' N and longitude 94°40.8' W.

The S190A multispectral camera system took a burst of 10 photographs, each having an approximate 60-percent forward overlap so these data could be used to calculate the altitude of the cloud top by stereographic techniques similar to those described in references 9-1 and 9-2. The stereoplotting was done with a stereoplotter at the NASA Lyndon B. Johnson Space Center (JSC) using the 0.8- to 0.9-micrometer band. The water was visible east of the cloud but made a poor reference; therefore, the altitude of the orbital workshop was used as the reference. The photograph (fig. 9-1) shows the north-south oriented squall line with dense cirrus clouds to the west and scattered low clouds to the east. Two high regions were evident, one large area (10 by 20 kilometers) that was about 13.5 kilometers and a small region (perhaps a young cell) at about 11.3 kilometers. The error in altitude for this analysis varies from ±50 to ±500 meters, depending on cloud texture and density.

Data Quality From S192

Fifteen seconds of S192 multispectral scanner imagery was received by the investigators for the August 8, 1973, thunderstorm. Of this, 594 scan lines were of primary interest. John Engvall¹ reported in a Skylab discrepancy report that sensor data outputs (SDO's) 7, 8, 15, 16, and 22 had a high percentage of saturated (255) values. Therefore, these SDO's were not used in the analysis. He also reported that some overfiltering was observed on many other

^aNASA Lyndon B. Johnson Space Center, Houston, Texas.

^bNational Severe Storms Laboratory, Norman, Okla.

^cLockheed Electronics Company, Houston, Texas.

¹In the EREP S192 Data Quality Monitoring Report for August 8, 1973 (Rept-159-03-16, March 11, 1975).

channels over clouds. The correspondence between the channels and SDO's and the channel quality is given in table 9-I.

Thermal Analysis From S192

To easily correlate the equivalent black-body temperature of the cloud top with the altitude and the corresponding equilibrium, preprocessing software was written so that the radiance in channel 13 could be converted to temperature (in kelvin). A second order polynomial was fit to the tables for temperature as a function of radiance given by J. F. DeMoss in the EREP instrumentation calibration manual over a range of 240 to 318 K. The fit was accurate within ± 1 K near 300 K and ± 0.25 K near 240 K. The second order polynomial formula is

$$T = 193.78 - 5.276835 \times 10^7 I^2 + 1.6314132 \times 10^5 I$$

where T is the equivalent black-body temperature in kelvin and I is the S192 channel 13 radiance in $W/(cm^2 \cdot \mu m \cdot sr)$. Figure 9-2 shows the cloud top as filmed on the data analysis station (DAS). The cloud top generally had radiance levels near $1.3 \times 10^{-4} W/(cm^2 \cdot \mu m \cdot sr)$, producing a saturation of channel 13 at an equivalent black-body temperature of 212 K. The radiosonde data for Lake Charles, Louisiana, for August 8, 1973, were obtained from the Space Flight Meteorology Group (National Oceanic and Atmospheric Administration) at JSC. These data were used to generate a table of atmospheric temperature as a function of altitude near the subject storm. Thus, if the storm top were in equilibrium, it should have the given temperature:

<u>Altitude, m</u>	<u>Temperature, K</u>
6 628	260
8 979	245
10 162	235
12 900	215
13 430	212
15 460	204

The yellow color in figure 9-2 indicates 212 to 215 K or 12 900 to 13 430 meters altitude, if in equilibrium. Actually these areas range from 13 500 to 15 935 meters according to the altimetry, thus indicating a consistent underestimate when the infrared altitude is used. The red color covers 10 162 to 12 900 meters if in equilibrium and the altimetry indicates 11 169 to 13 400 meters, thus indicating underestimates of 1000 meters or more. Light red covers 235 to 245 K or 8979 to 10 162 meters; the only data point from altimetry in this color is 9000 meters. Orange covers the temperature range of 245 to 260 K or 6628 to 8979 meters, whereas actual altitudes from altimetry

are 3522 to 7157 meters. Thus, in this test the infrared altitude underestimates the high cloud tops and overestimates the medium-altitude cloud tops.

The sea-surface S192 equivalent black-body temperature was in the range of 280 to 300 K with a mean of 295 K. About 4 hours before the experiment, a ship measured the "bucket" temperature to be 300 K within a few kilometers of the thunderstorm. Six ships in the area that day reported a mean of 301 ± 2 K. Thus, the departure of S192 temperatures from the ground truth is about 5 K, which is in good agreement with the S192 scanner and S191 spectrometer analysis for June 11, 1973, over Oklahoma.

Thermal Analysis From S191

Data from S191 over the cloud top and nearby ocean areas were curve fit using the technique described in reference 9-3 to determine the best equivalent black-body temperature. The time history of this result is given in figure 9-3. The S191 operator, most of the time, appeared to try to avoid the cloud top as he looked around and the result is that data acquired over the cloud were smeared and only a few scans were acquired. Where possible, these data on S191 and S192 were correlated to compare accuracy.

<u>Time, min:sec</u>	<u>S191 temperature, K</u>	<u>S192 temperature, K</u>
6:08	248	241
6:09	229	231

Thus, in this small data set, the two appear similar.

Cloud Phase Detection From S191

Spectrometer (S191) data on the August 8 EREP pass included spectral scans, in the visible to near infrared (0.5 to 2.4 micrometers), of areas of the cirrostratus deck (fig. 9-1) near 13 kilometers altitude and cumulus cloud tops at about 1 to 4 kilometers altitude near the Texas coast. The cumulus cloud radiance seen in figure 9-4 shows that from 0.5 to about 0.9 micrometers, the reflected radiance is about equal to the solar radiance. At longer wavelengths, minima of reflected radiance are evident at 0.9419, 1.135, 1.38 to 1.45, 1.87, and 2.66 micrometers. These minima are a result of atmospheric water vapor absorption along the Sun-cloud-spacecraft path. Carbon dioxide absorption decreases the signal at 1.43 micrometers and at 1.96 to 2.06 micrometers. The cirrostratus reflected radiance indicates a reduction in reflectance from 0.5 to 0.9 micrometers, from 1.35 to 1.8 micrometers, and from 1.9 to 2.5 micrometers. The area around the center of the water vapor absorption regions has higher radiance because very little water vapor occurs above the 13-kilometer cloud tops. Furthermore, the reflected radiance of the cirrostratus deck shows minima at 1.47, 2.0, and 2.3 micrometers. These results agree well with the aircraft spectra of similar clouds taken by Hunt, Salisbury, and Bunting (ref. 9-4), who found major ice absorption lines at 1.5 and 2.0

micrometers. Furthermore, both the cumulus and cirrostratus cloud reflectance agree well with the absorption coefficient data for water and ice of Irvine and Pollack (ref. 9-5) shown in figure 9-5. Careful examination of figure 9-4 in light of the absorption coefficient shows that the liquid water absorption at 1.44 micrometers lies on top of the water vapor absorption at 1.38 to 1.45 micrometers; also the 1.95-micrometer liquid water absorption is very distinct from the 1.87-micrometer water vapor absorption.

Considering the absorption coefficient curves, it is evident that the S192 bands 11 (1.45 to 1.85 micrometers) and 12 (2.0 to 2.42 micrometers) are not optimum choices for cloud phase detection. Figures 9-4 and 9-5 indicate that a near-optimum sensor could be constructed to use the bands of 1.37 ± 0.07 micrometers and 1.50 ± 0.07 micrometers to give a ratio of the latter divided by the former of 6.0 for liquid water and 0.6 for the ice phase.

Cloud Phase Detection From S192

Hovis (ref. 9-6) has shown that ice crystals have low reflection in the near-infrared spectral range between 1.4 and 2.4 micrometers. Because this is the spectral region covered by S192 bands 11 (SDO 11 and 12) and 12 (SDO 13 and 14), the June 11, 1973, screening film was perused and regions of dense cirrus and water droplet clouds were located. These areas were then gray mapped, training fields were chosen, and statistics were calculated using the LARSYS system² on the computers at JSC. Figure 9-6 shows that SDO 11 for the cirrus cloud had a mean of 80 ($147 \times 10^{-5} \text{ W}/(\text{cm}^2 \cdot \mu\text{m} \cdot \text{sr})$) and figure 9-7 shows that SDO 11 for a water cloud had a mean of 130 ($242 \times 10^{-5} \text{ W}/(\text{cm}^2 \mu\text{m}^5)$).

The SDO 11 data were color enhanced and filmed (fig. 9-8) on the DAS at JSC. Two things are striking about the result: (1) much more structure is evident in this image than in the photograph from S190 in figure 9-1 and (2) areas that have a radiance higher than 185×10^{-5} in SDO 11 (red on the image) should be water clouds and indicate an area of new development on the east edge of the squall line. This is in agreement with the direction of propagation of the line.

In bands outside the 1.4- to 2.4-micrometer area, cirrus and other clouds have similar reflectances, thereby allowing ratios of bands to be used to extend these signatures to other Sun angles. Figures 9-6 and 9-7 show the ratio 700 (SDO 11/SDO 18) histogram for cirrus and water clouds. The two clusters are clearly indicated as distinct, but it is not necessarily obvious that the ratio of the bands is better than SDO 11 alone. The LARSYS separability program showed that, for the channels that were not thresholded, the following SDO's were the best (in order of importance): 21, 11/19, and 11. The tests included equal weighting and weighting proportional to e^{-D} (where D is the

²A maximum likelihood pattern recognition computer program developed by the Laboratory for Applications of Remote Sensing at Purdue University.

divergence between classes). The SDO 21 data depend on the fact that cirrus clouds are cold and other clouds are usually at warmer altitudes; however, the use of SDO 11 and ratios using that band make use of inherent physical characteristics of the two classes and therefore could distinguish cirrus and a liquid water cloud lying at the same altitude, side by side.

In order to better understand the relationship between the S192 spectral channels and the occurrence of water and ice phases of clouds, plots of spectral radiances for SDO's 1, 9, 17, 19, 20, 11, 13, and 21 were prepared for the August 8 storm along a line parallel to the groundtrack of Skylab. This was done by determining the average radiance for collections of 2- by 7-pixel (picture element) areas along this line for each channel. Each such line is called a transect.

Transect number 1 on the August 8 thunderstorm (shown in fig. 9-1) started over the cirrus shield, continued over the edge of the 11 300-meter tower, and over the ocean surface. Figure 9-9 indicates the counts in each channel across the transect from A_1 to B_1 . SDO's 1 and 9 appear to be highly correlated and they were saturated over the thicker cloud areas. These two SDO's are representative of the other channels less than 1.3 micrometers. SDO's 11 and 13 appear correlated and increase by a large amount on the edge of the cumulus tops. This increase is probably due to an active growing cell in the cumulus that is still composed of liquid water drops. Lower readings in these two SDO's would indicate the ice phase. Furthermore, as these two channels increase over the active cell, the equivalent black-body temperature increases by more than 15 K. The temperature over the growing cell, however, is about 263 K, still cold enough to require the drops to be supercooled or for the growing cell to be partially covered by a colder cirrus cloud.

Figure 9-10 shows a two-dimensional histogram plot of the ratio of SDO 11/9 versus the reflectance in channel 9, where

$$\text{Reflectance} = \frac{\pi R_i}{\mu_o I_{si}}$$

R = radiance in band i

$$\mu_o = \cos \theta$$

θ = solar zenith angle

I_{si} = solar irradiance in band i

These data in figure 9-9 allow one to determine that the transect from A_1 to B_1 follows the path from A_1 to B_1 shown in figure 9-10. The cirrus shows up as the lower right-hand cluster due to the lower 11/9 ratio and the high reflectance in SDO 9. The ocean surface and the water cloud have approximately

the same 11/9 ratio but the latter has a significantly higher reflectance in SDO 9, thus separating the two clusters. The data over the water cloud tower saturated in SDO 9, however, so there is no assurance that the channel 9 reflectance did not also increase at the same rate as channel 11. Figure 9-11 shows the plot of the 11/9 ratio compared to equivalent black-body temperature of the cloud or ocean surface. This shows two distinct clusters that divide about the 11/9 ratio of about 40 and a temperature of about 265 K. The ocean surface is the right-hand region of the top cluster with the water cloud tower occupying the left-hand side of the top cluster. The cirrus cluster is both colder and lower in 11/9 ratio than are the other two features.

Transect number 2 on the August 8 thunderstorm shown in figure 9-1 was parallel to transect number 1 but passed directly over the 11 300-meter thunderstorm top from A_2 to B_2 . Figure 9-12 shows the counts in several channels across the transect. SDO 9 saturated over a wide area of the cloud top, whereas SDO 17 saturated only over the highest region of the cloud top. Higher values occur on the sunward side of the roll cloud in all channels, where the equivalent black-body temperature increases significantly. This is believed to be caused by an active growing cumulus cloud region composed of water drops. This active area is on the opposite side of the cloud from the active area found on transect 1. Figure 9-13 shows a two-dimensional histogram of the ratio ($\text{SDO } 11/\text{SDO } 9 \times 100$) compared to the reflectance in channel 9 doubled. The transect starts at A_2 , moves to the right to the 11 300-meter cloud top, up to the roll cloud, and back to the water cloud in the B_2 region. It appears, based on these data, that values of the ratio less than 50 may be used to indicate water is in the solid phase. Figure 9-14 shows a two-dimensional histogram plot of the ratio compared to equivalent black-body temperature as measured in the SDO 21 channel. The transect starts over an ice cloud at A_2 , moves to the lower left near the roll cloud, and moves rapidly to the upper right into the liquid-water cloud region. The ocean surface appears at a ratio of about 60 and a temperature of 268 K. Based on this plot, it appears that any realistic value of the ratio (e.g., 56) will require acceptance of the theory that some water droplet regions are supercooled by more than 10 K.

BORNEO THUNDERSTORM

To extend the conclusions derived from the August 8, 1973, thunderstorm, data were analyzed from a less severe thunderstorm observed near Borneo in the East Indies on December 9, 1973. Transect 3 started at A_3 of figure 9-15 and continued over the cirrus cloud top. Figure 9-16 indicates the counts in each channel across the transect (A_3 to B_3). All SDO's appear to be highly correlated, with colder areas appearing brighter. Figure 9-17 shows a two-dimensional histogram plot of the ratio SDO 11/9 compared to the reflectance in channel 9. This plot is significantly different from the August 8 transects shown in figures 9-10 and 9-13. Very little area in figure 9-17 has the characteristic of optically thick water clouds, whereas the great majority exhibits

the characteristic of optically thick cirrus. The ocean area around A_3 exhibits the characteristics of the ocean surface seen in transects 1 and 2. Figure 9-18 compares the ratio of SDO 11/9 and equivalent black-body temperature derived from SDO 21. This figure also is quite different from the thermal transects over the August 8 thunderstorm (figs. 9-11 and 9-14). In figure 9-18, very cold cloud tops appear to be composed of the liquid phase of water (high ratios of SDO 11/9 > 40) as well as the solid phase of water (SDO 11/9 < 40).

Transect 4 (fig. 9-19) over the December 9, 1973, Borneo thunderstorm started over the ocean at A_4 and continued to B_4 , which was in an area of thin clouds. This transect has similar properties to transect 3, in that all channels appear correlated; however, this area has much warmer temperatures. Figure 9-20 shows that the low reflectance in SDO 9 over the ocean at A_4 was accompanied by a highly variable ratio of SDO 11/9. Clouds with a reflectance in channel 9 greater than about 10 percent appear to have 11/9 ratios greater than 40, indicating these are water droplet clouds. Indeed, figure 9-21 shows that both the ocean and the cloud are warmer than about 271 K and greater than 50 in 11/9 ratio, thus corroborating the other data, which indicate that none of the clouds are in the ice phase.

CONCLUSIONS

The combination of the thermal-infrared and the near-infrared bands near 1.0 to 2.0 micrometers provides sufficient information to determine whether a cell is young and growing, is mature, or is decaying. This, together with areal measurements of the amount of water in each phase over growing thunderstorms, could provide key inputs of mesoscale energy budgets for both developing airmass thunderstorms and squall-line-type thunderstorms. However, for this important information to be usable for forecasting thunderstorms, it must be available on the scales of a few hundred meters and tens of minutes. This would, of course, require geosynchronous satellites with large-aperture multispectral scanners.

REFERENCES

- 9-1. Whitehead, Victor S.; Browne, Ivan D.; and Garcia, Joe G.: Cloud Height Contouring From Apollo 6 Photography. Bull. American Meteorol. Soc., vol. 50, no. 7, July 1969, pp. 522-528.
- 9-2. Shenk, William E.; and Holub, Robert: An Example of Detailed Cloud Contouring From Apollo 6 Photography. Bull. American Meteorol. Soc., vol. 52, no. 4, April 1971, p. 238.
- 9-3. Pitts, David E.; Reeser, Warner K.; and Mendlowitz, Maury A.: Equivalent Blackbody Temperature of the Top of a Severe Storm. J. Appl. Meteorol., vol. 14, no. 4, June 1975, pp. 609-618.
- 9-4. Hunt, G. R.; Salisbury, J. W.; and Bunting, J. T.: A Study to Develop Improved Spacecraft Snow Survey Methods Using Skylab EREP Data: Demonstration of the Utility of the S-190A and S-192 Data. Air Force Cambridge Research Laboratories, Terrestrial Sciences Laboratory, Hanscom AFB, Mass., 1974.
- 9-5. Irvine, W. M.; and Pollack, J. B.: Infrared Optical Properties of Water and Ice Spheres. Icarus, vol. 8, 1968, pp. 324-360.
- 9-6. Blau, H. H.; and Hovis, W. A.: Cloud Characteristics From Infrared Measurements. Space Research XI, Akademie-Verlag, Berlin, 1971.

TABLE 9-I. CHANNEL IDENTIFICATION AND QUALITY

Channel	Color (10-percent transmission)	Wavelength, μm	SDO	Data quality	Saturates on clouds	Ice/water distinction	Atmospheric correction
1	Violet	0.41 to 0.45	22	Not usable	Yes	No	Cirrus distinction
2	Blue	0.44 to 0.51	18	Excellent	Yes	No	Cirrus distinction
3	Blue-green	0.49 to 0.57	1, 2	Good	Yes	No	
4	Green-yellow	0.53 to 0.61	3, 4	Good	Yes	No	
5	Orange-red	0.59 to 0.68	5, 6	Good	Yes	No	
6	Red	0.64 to 0.77	7, 8	Very good	Yes	No	
7	Near-infrared	0.72 to 0.97	9, 10	Very good	No	No	
8	Near-infrared	0.88 to 1.09	19	Excellent	Yes	No	Cirrus and water vapor distinction
9	Near-infrared	1.00 to 1.24	20	Excellent	Yes	No	
10	Near-infrared	1.10 to 1.35	17	Good	No	No	
11	Near-infrared	1.45 to 1.85	11, 12	Excellent	No	Yes	
12	Near-infrared	2.00 to 2.42	13, 14	Excellent	No	Yes	
13	Infrared	9.70 to 13.00	15, 16, 21	Poor	Cold clouds	No	Cirrus distinction

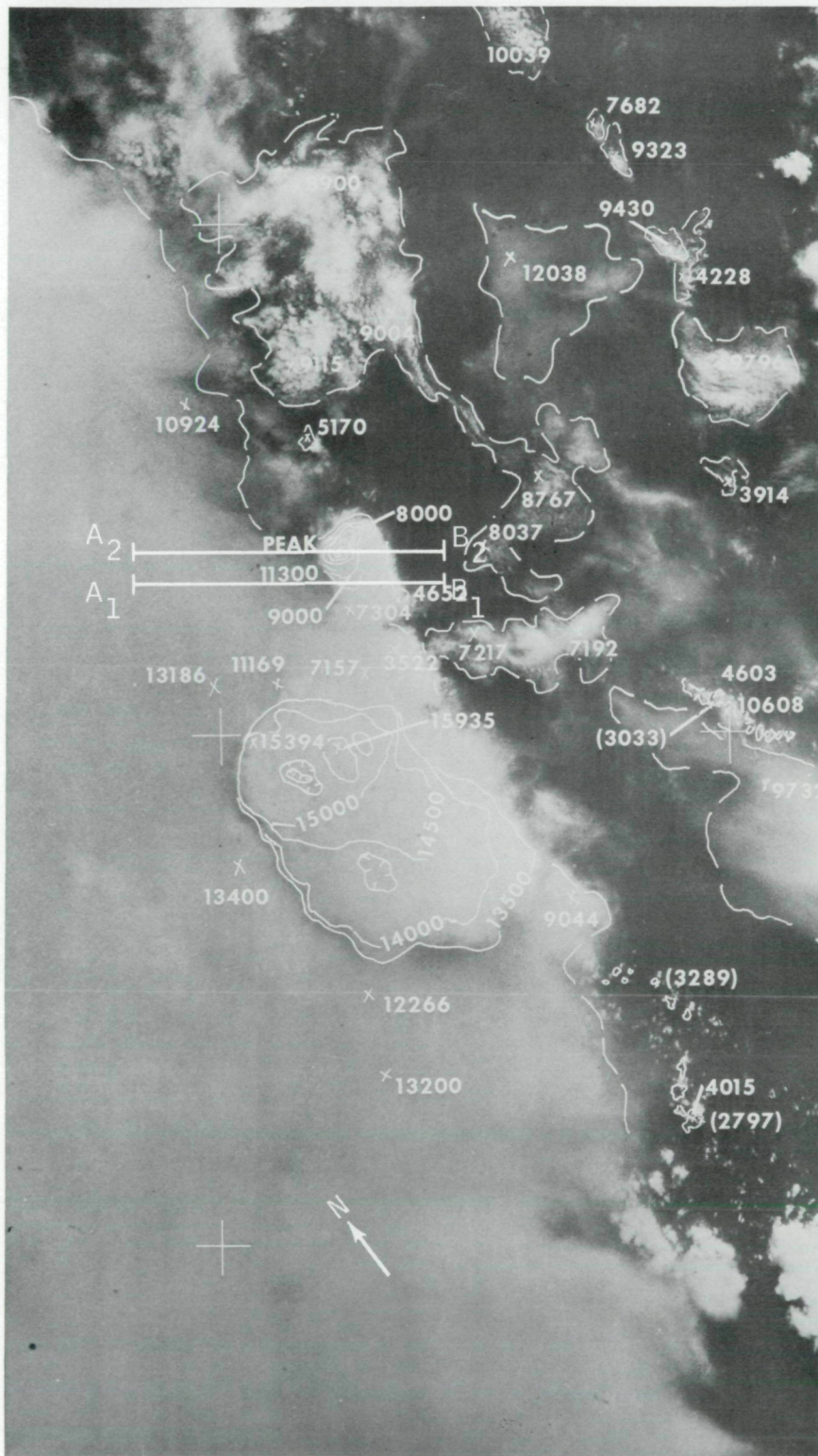


Figure 9-1.- Squall line of August 8, 1973, taken from S190A (SL3-20-353 and SL3-20-354). Cloud-top altitudes are shown in meters, with the apparent cloud-base altitude in parentheses.

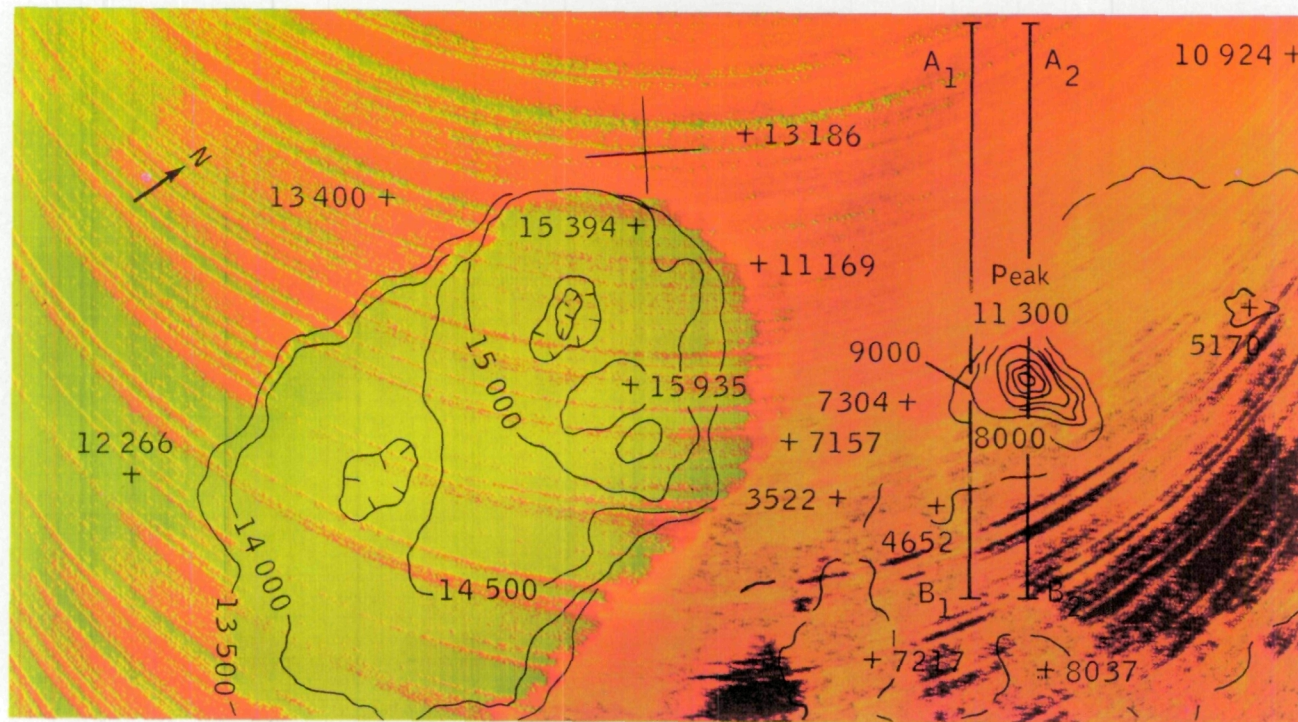


Figure 9-2.- Color-enhanced image from S192 thermal-infrared band (channel 13, sensor data output (SDO) 21) of the center part of the area shown in figure 9-1. Equivalent black-body temperature variations are indicated by the color variations. Altitudes of cloud tops are shown in meters.

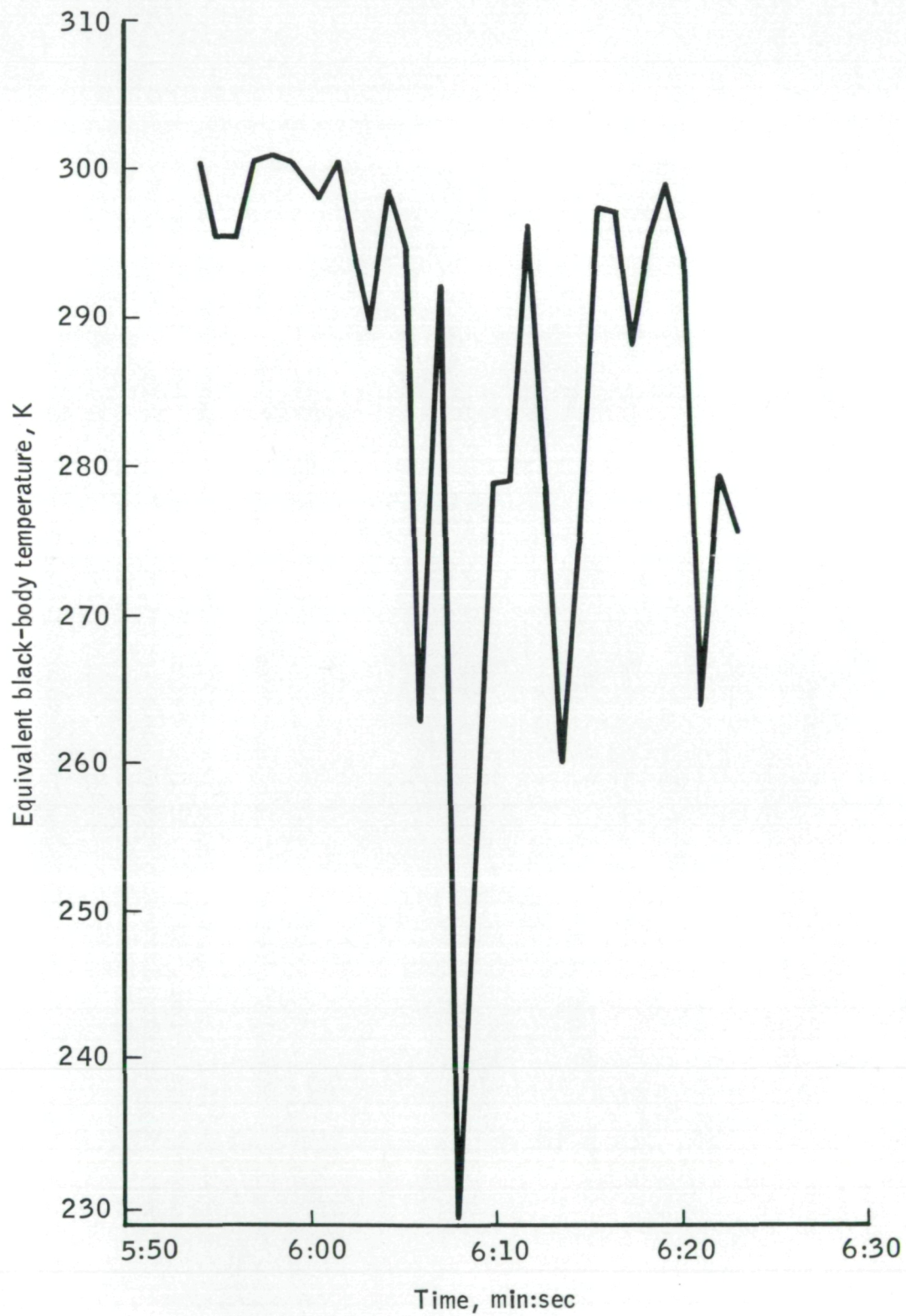


Figure 9-3.- Equivalent black-body temperature as a function of time (S191 data).

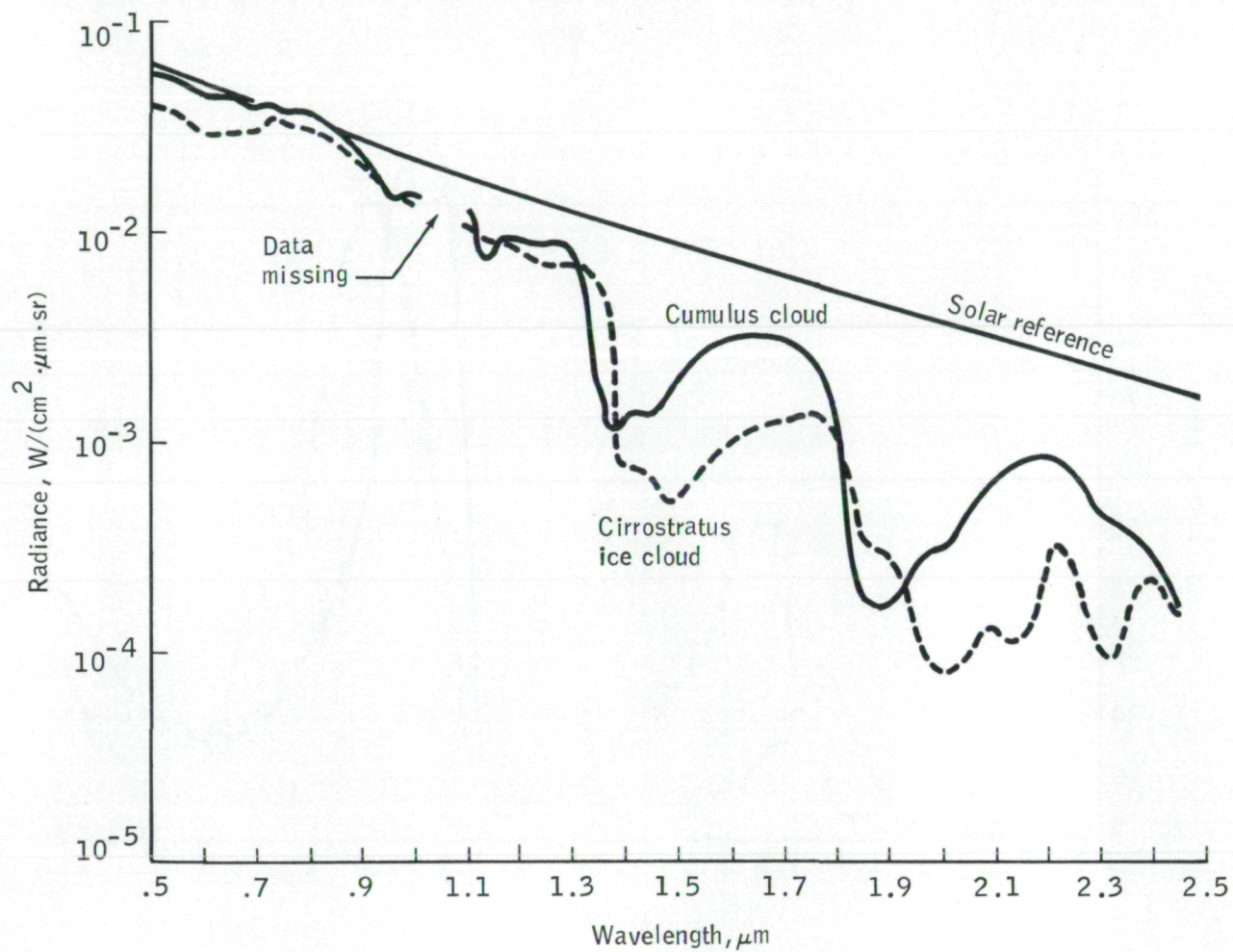


Figure 9-4.- The S191 reflected radiance for a cumulus cloud and for a cirrostratus cloud in the area shown in figure 9-1.

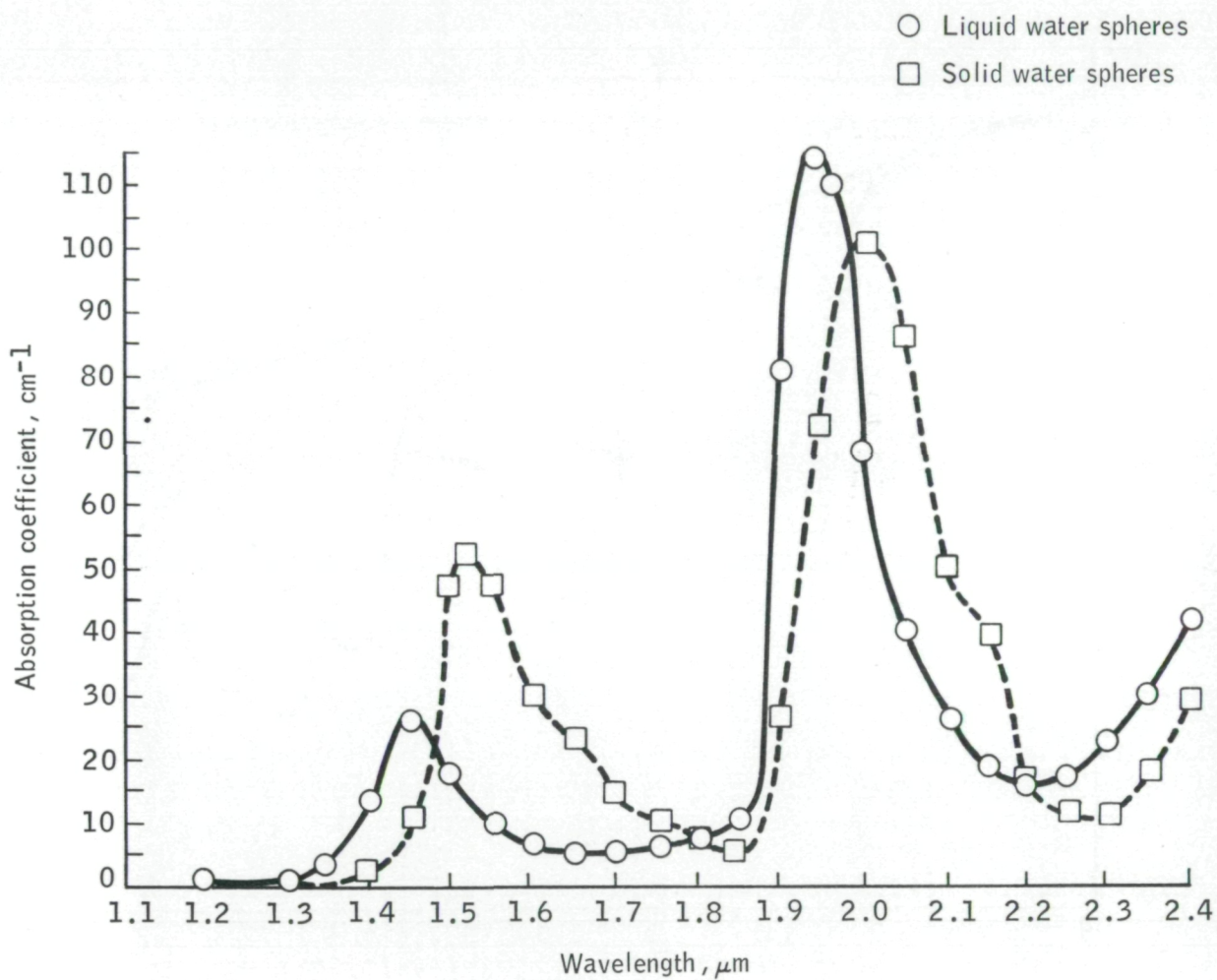
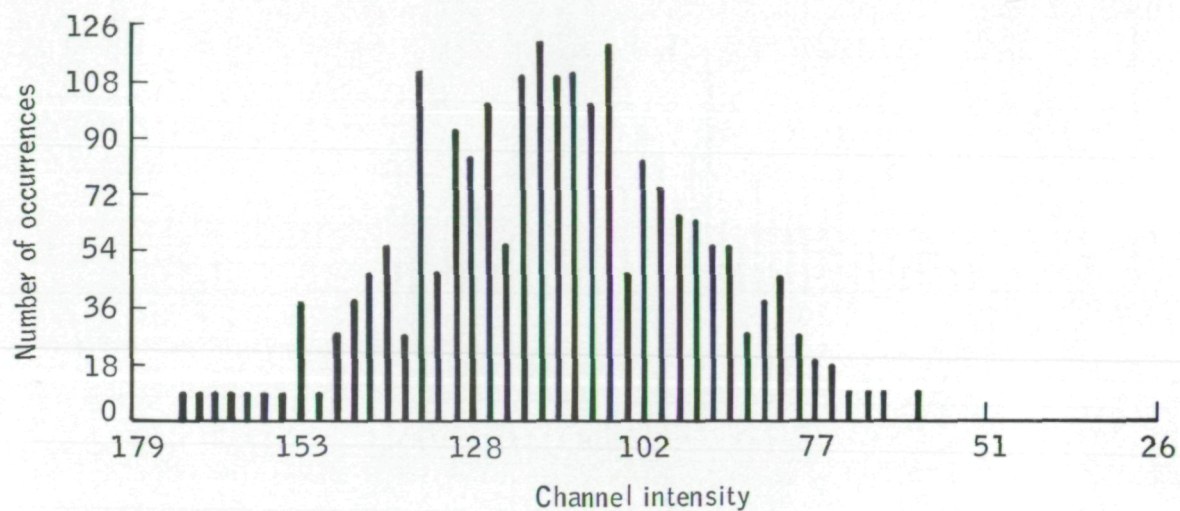
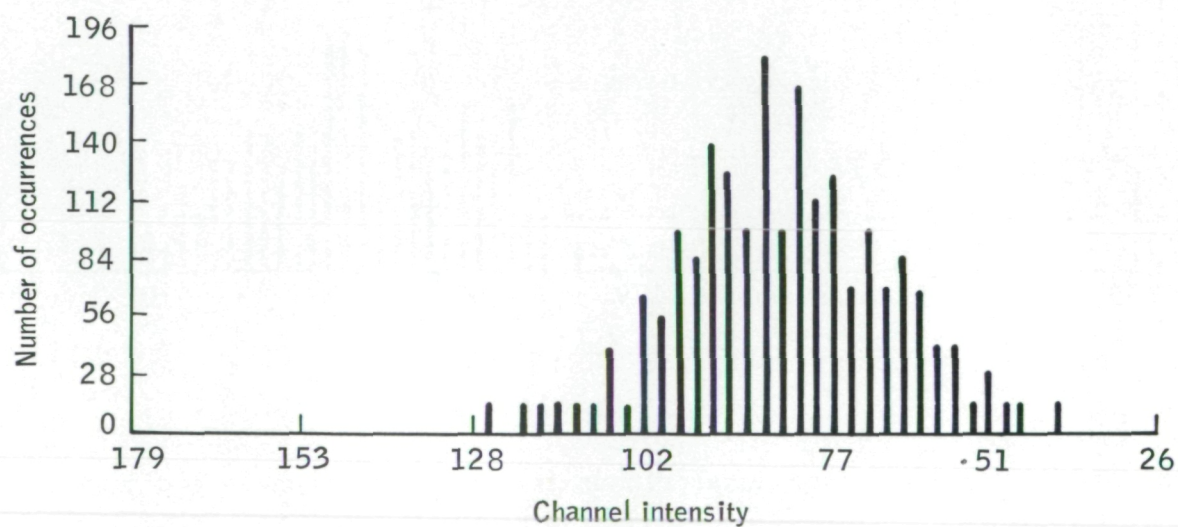


Figure 9-5.- Absorption coefficient for water and ice.

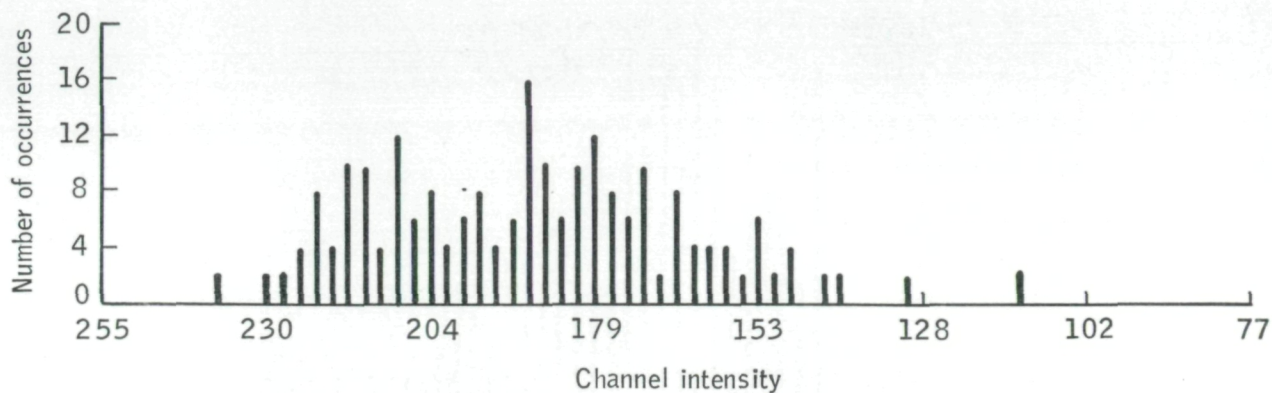


(a) 700 (SDO 11/SDO 18).

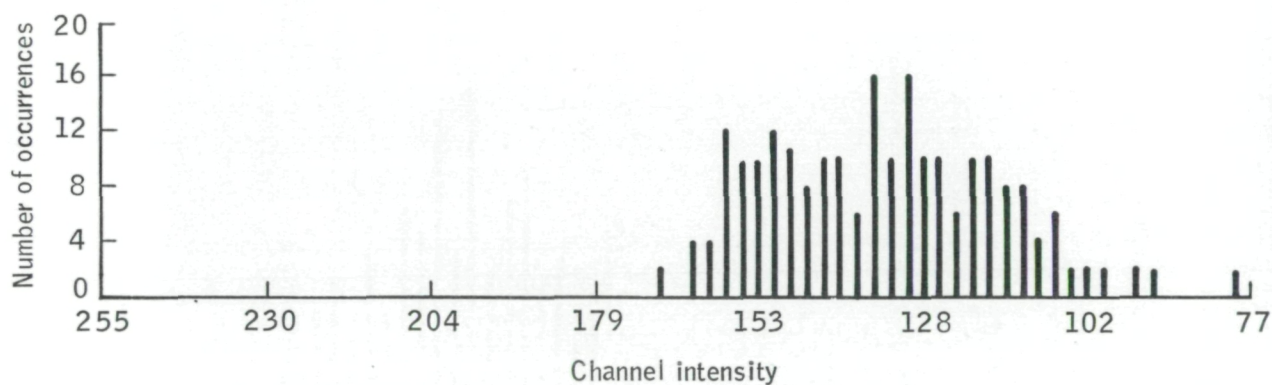


(b) SDO 11.

Figure 9-6.- Histograms for cirrus clouds on June 11, 1973.



(a) 700 (SDO 11/SDO 18).



(b) SDO 11.

Figure 9-7.- Histograms for water clouds for the same channels and date shown in figure 9-6.

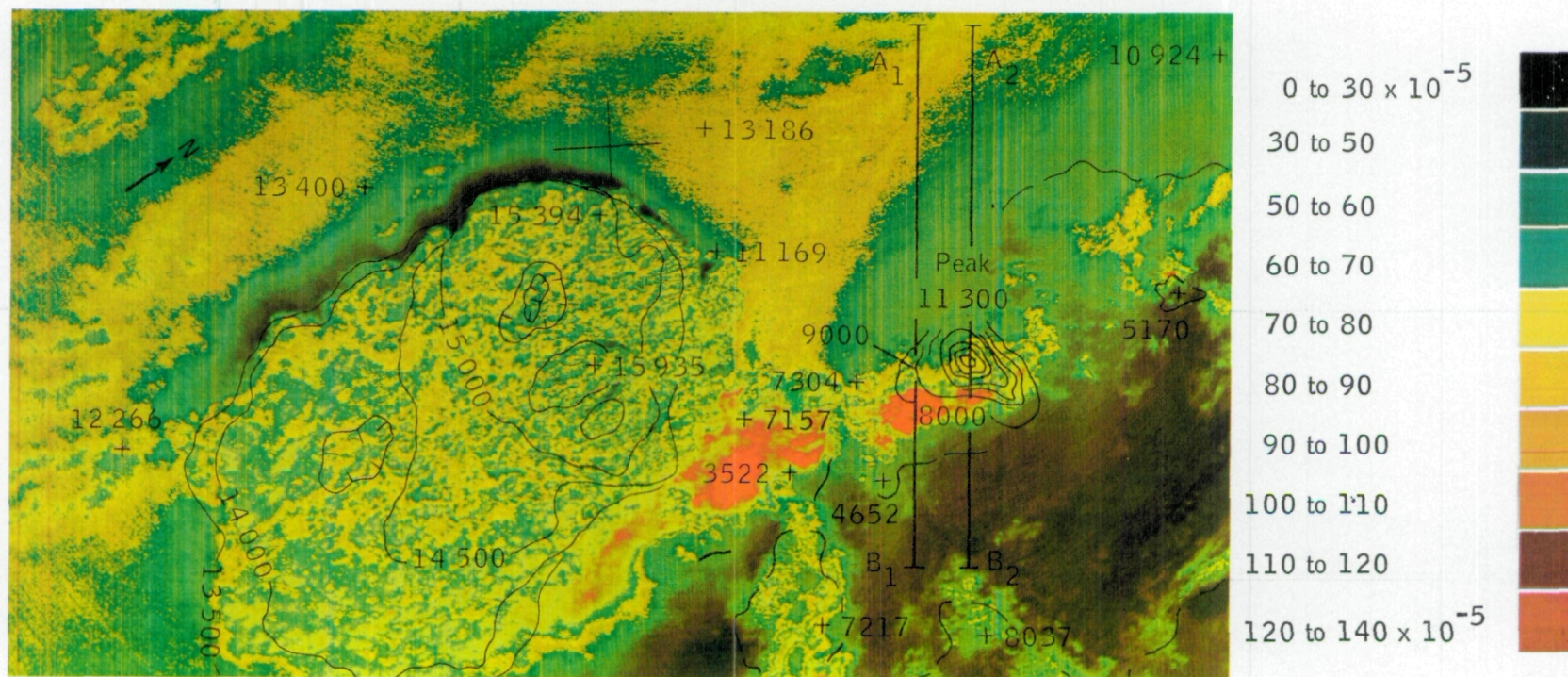
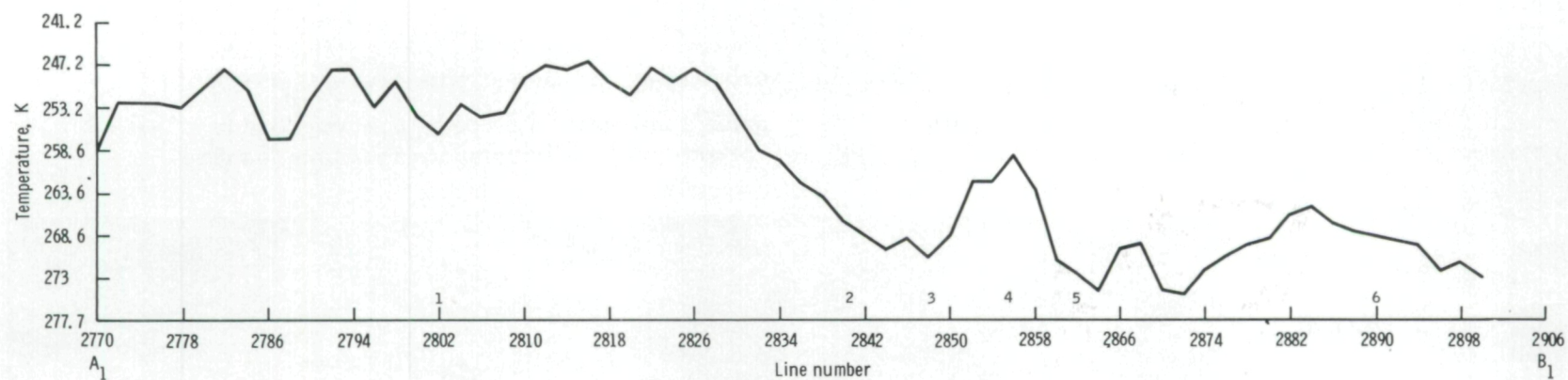
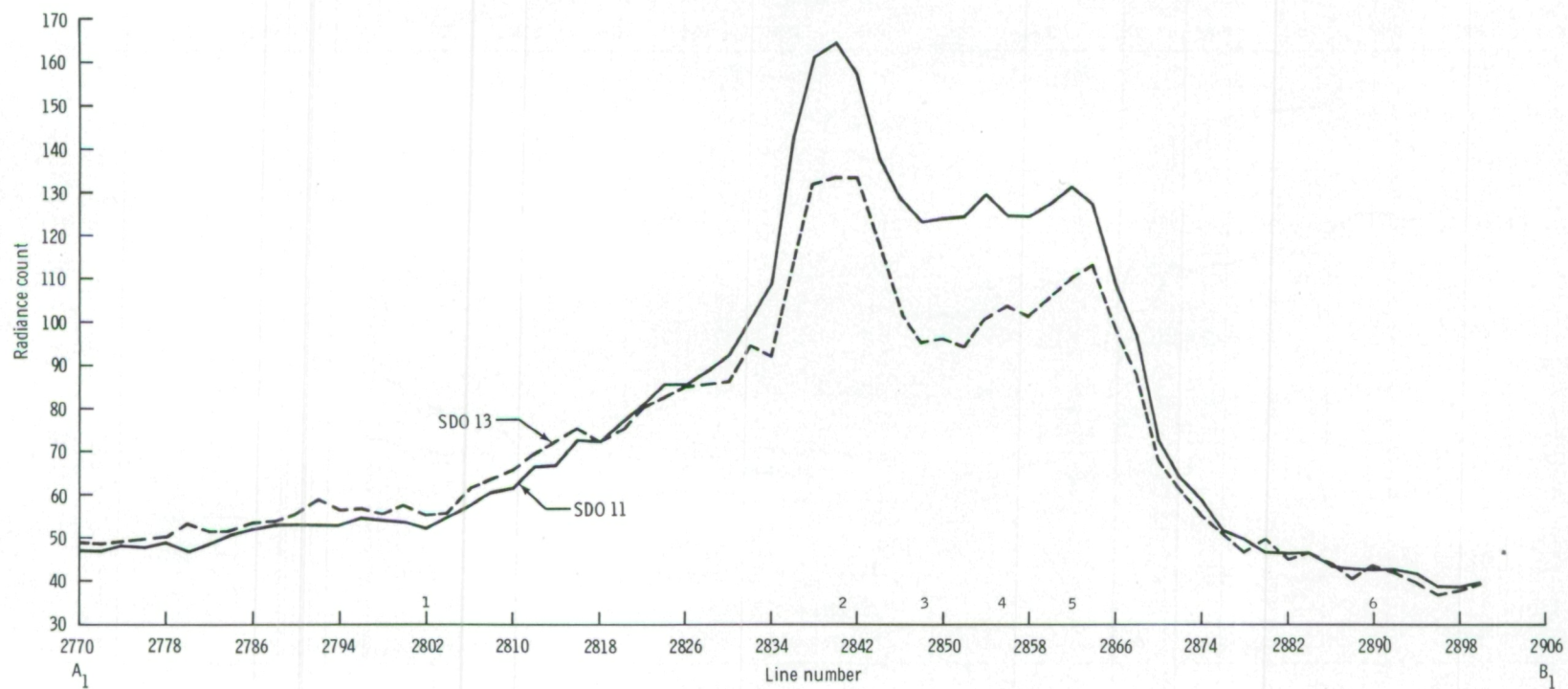


Figure 9-8.- Color-enhanced S192 image for SDO 11 (channel 11) showing approximately the same area as figure 9-2. Variations of radiance in $W/(cm^2 \cdot \mu m \cdot sr)$ are shown by the colors. Numbers are cloud-top altitudes in meters.



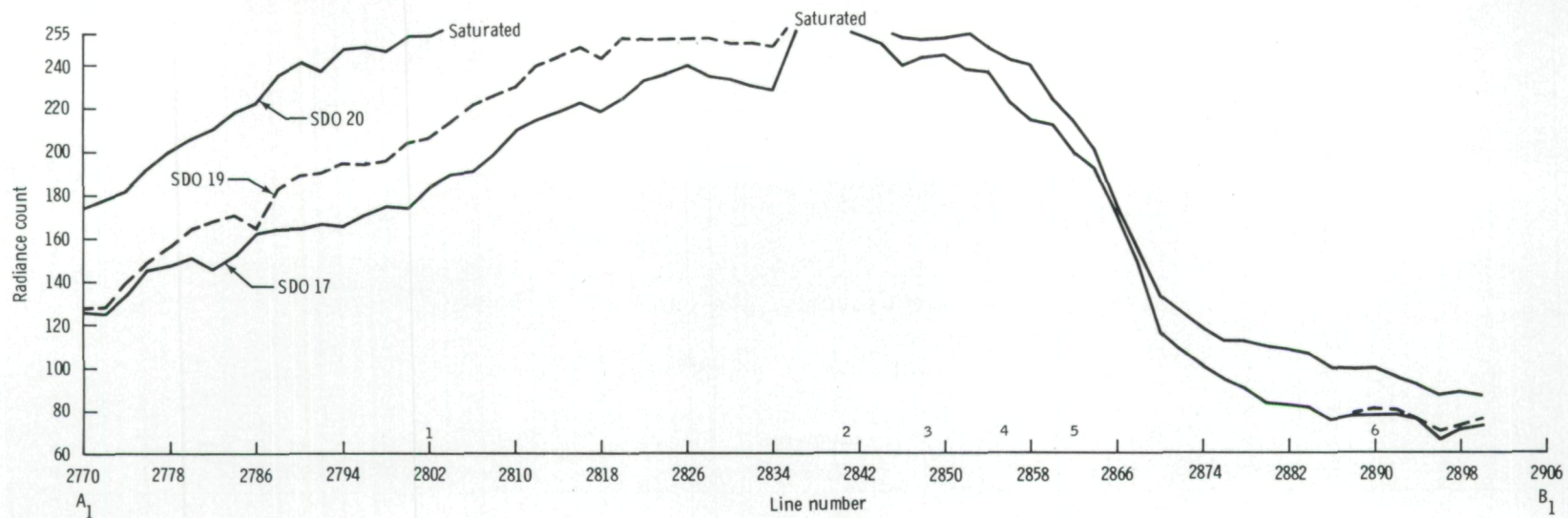
(a) SDO 21.

Figure 9-9.- Plot of transect 1 radiance counts for the August 8, 1973, Gulf of Mexico thunderstorm.

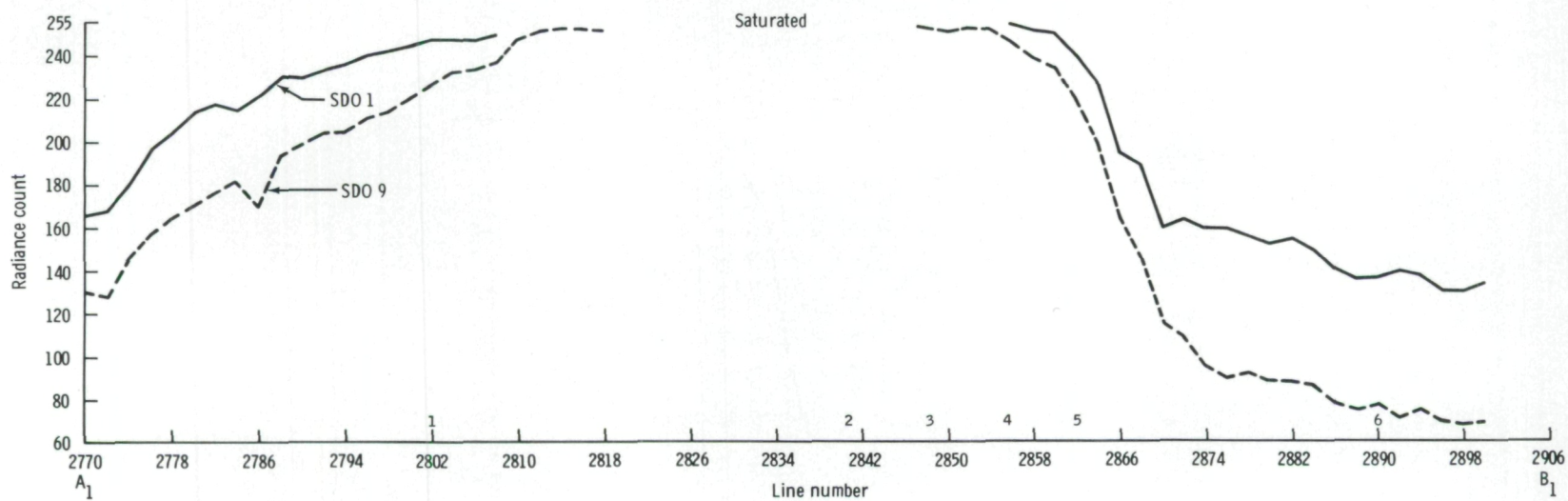


(b) SDO's 11 and 13.

Figure 9-9.- Continued.



(c) SDO's 17, 19, and 20.



(d) SDO's 1 and 9.

Figure 9-9.- Concluded.

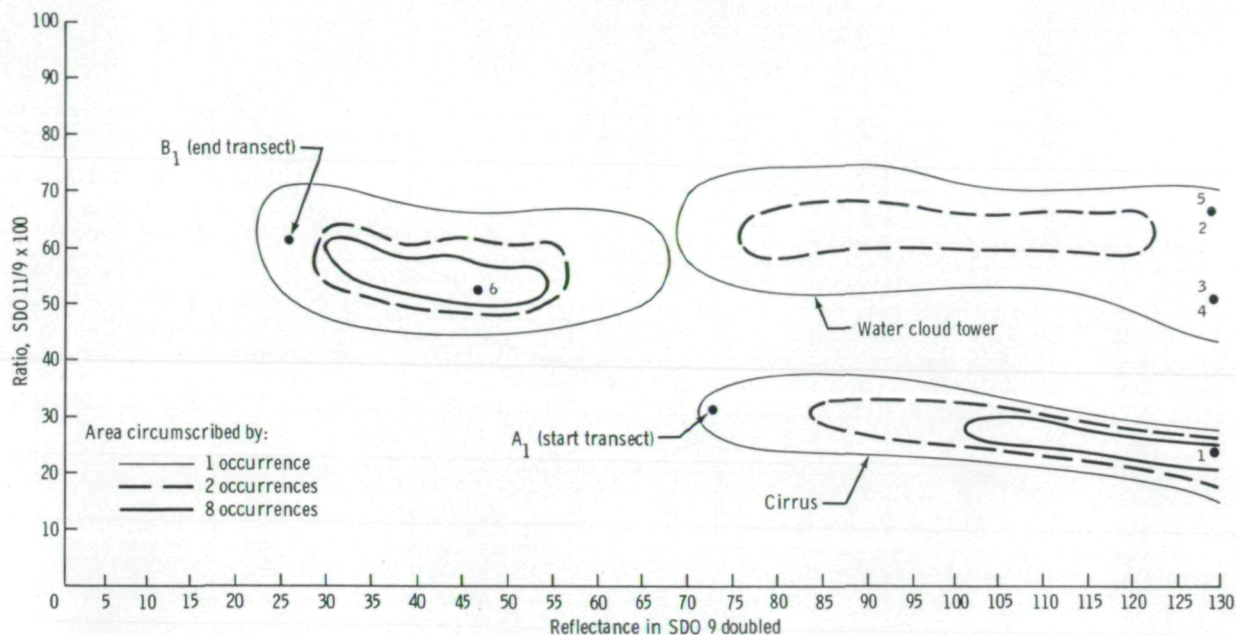


Figure 9-10.- Histogram of transect 1 for the August 8, 1973, Gulf of Mexico thunderstorm, comparing the ratio of SDO 11/9 to the reflectance in SDO 9 doubled. Points 1 to 6 refer to the points marked on the abscissa scale of figure 9-9.

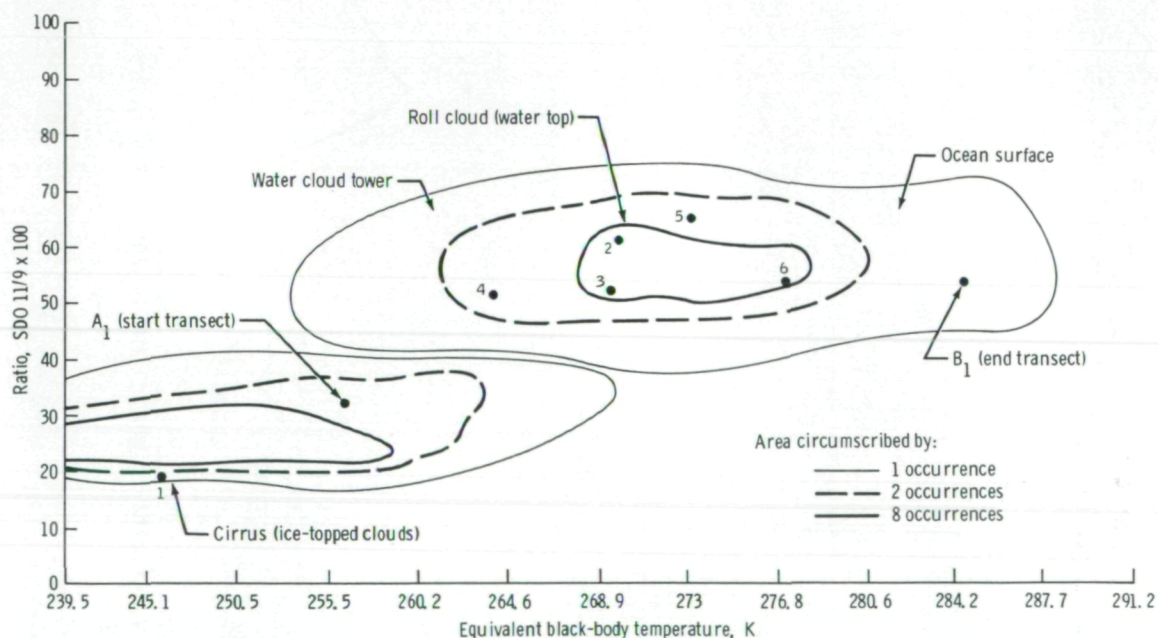
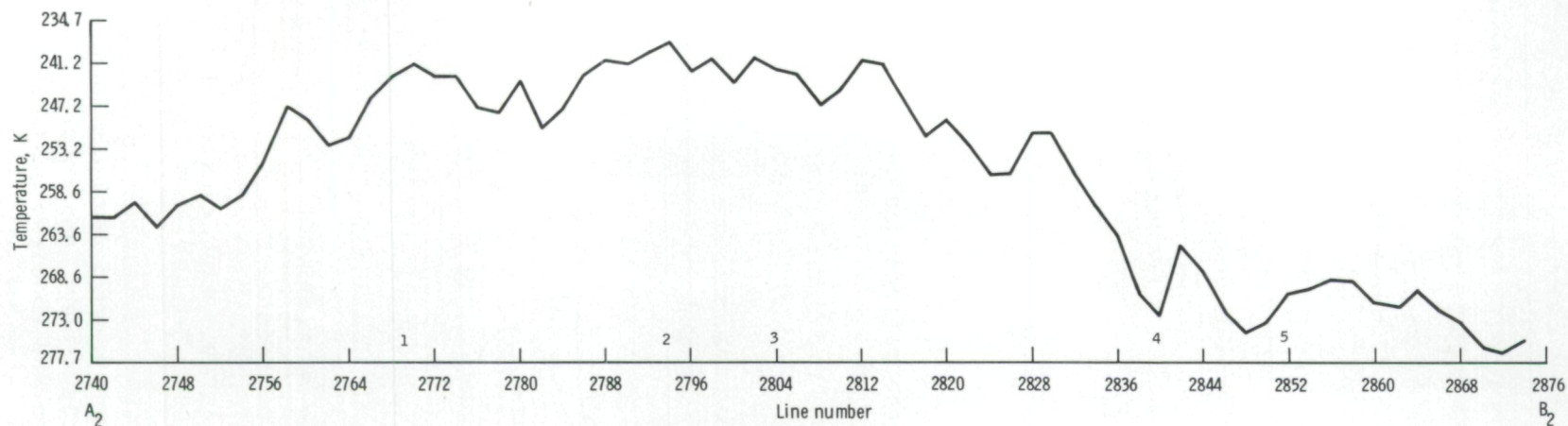
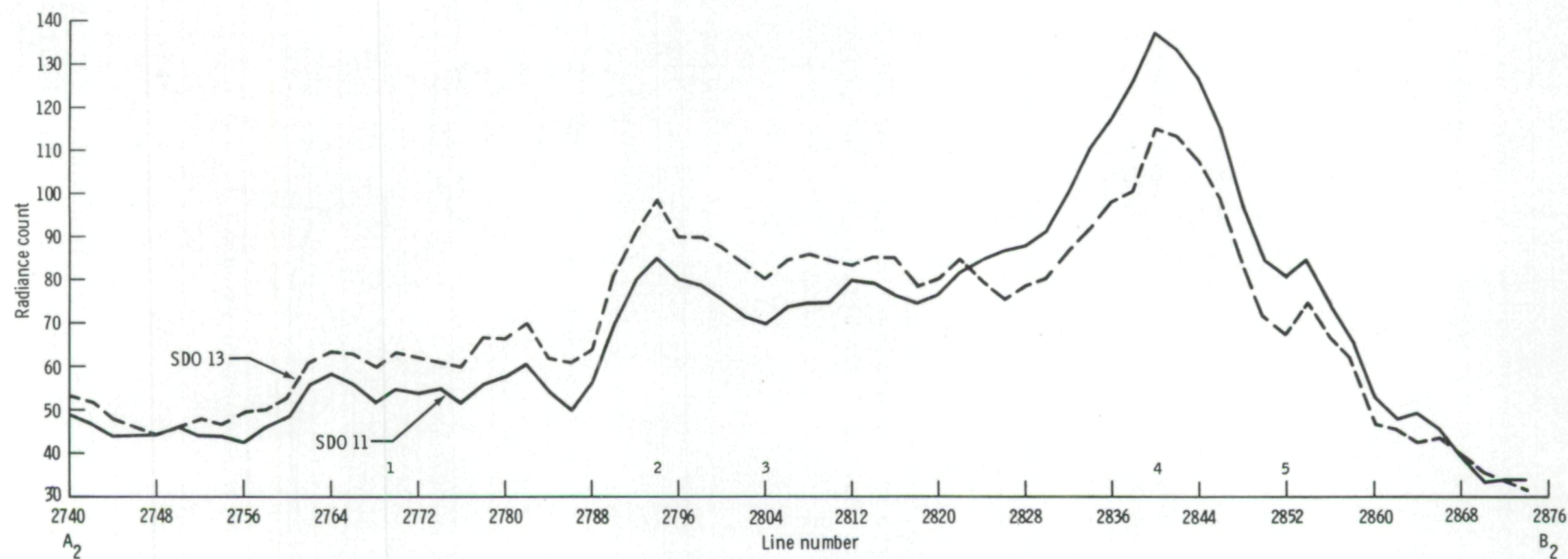


Figure 9-11.- Histogram of transect 1 for the August 8, 1973, thunderstorm, comparing the SDO 11/9 ratio to the equivalent black-body temperature. The numbered points refer to the points marked on the abscissa scale of figure 9-9.

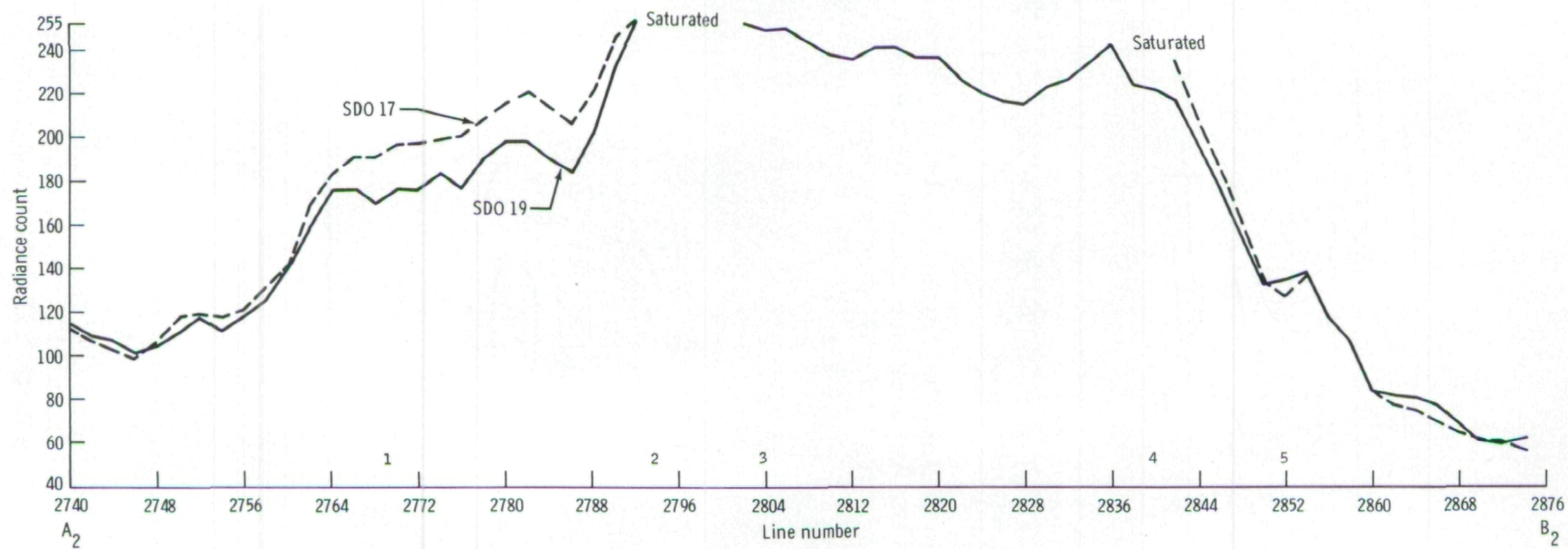


(a) SDO 21.



(b) SDO's 11 and 13.

Figure 9-12.- Plot of transect 2 radiance counts for the August 8, 1973, thunderstorm.



(c) SDO's 17 and 19.

Figure 9-12.- Concluded.

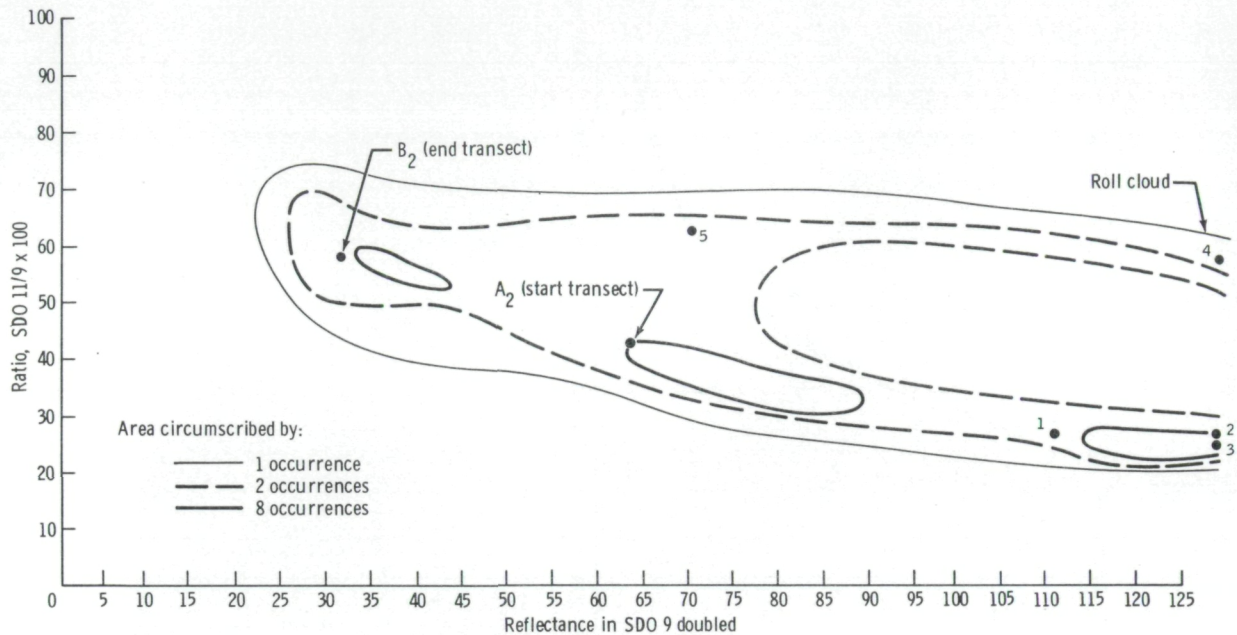


Figure 9-13.- Histogram of transect 2 for the August 8, 1973, thunderstorm, comparing the ratio of SDO 11/9 to the reflectance in SDO 9 doubled. The numbered points refer to the points marked on the abscissa scale of figure 9-12.

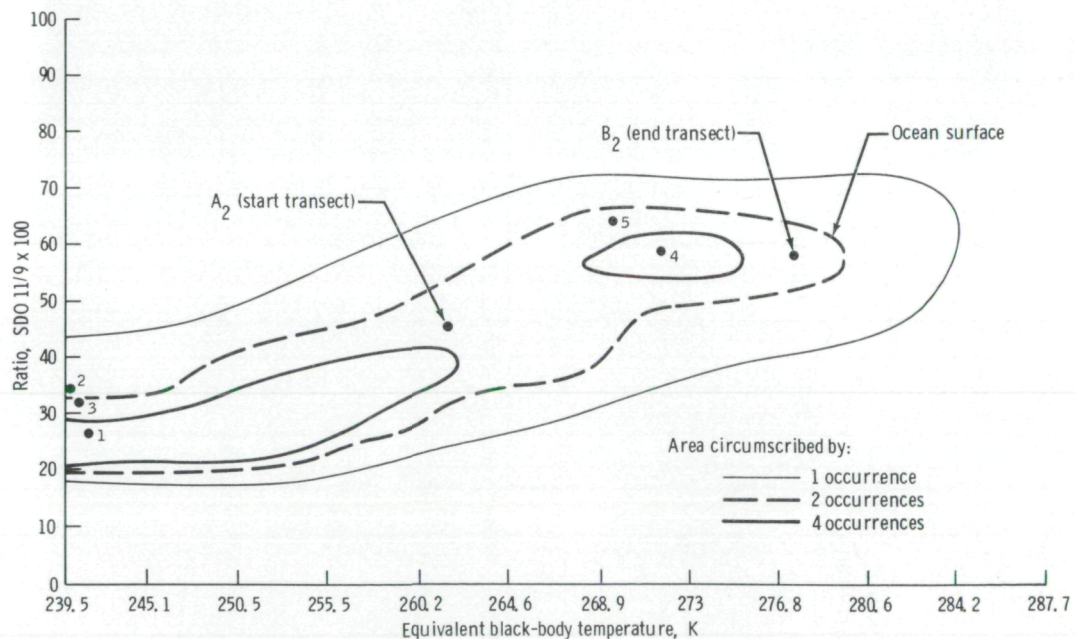


Figure 9-14.- Histogram of transect 2 for the August 8, 1973, thunderstorm, comparing the SDO 11/9 ratio to the equivalent black-body temperature (temperature based on SDO 21). The numbered points refer to the points marked on the abscissa scale of figure 9-12.

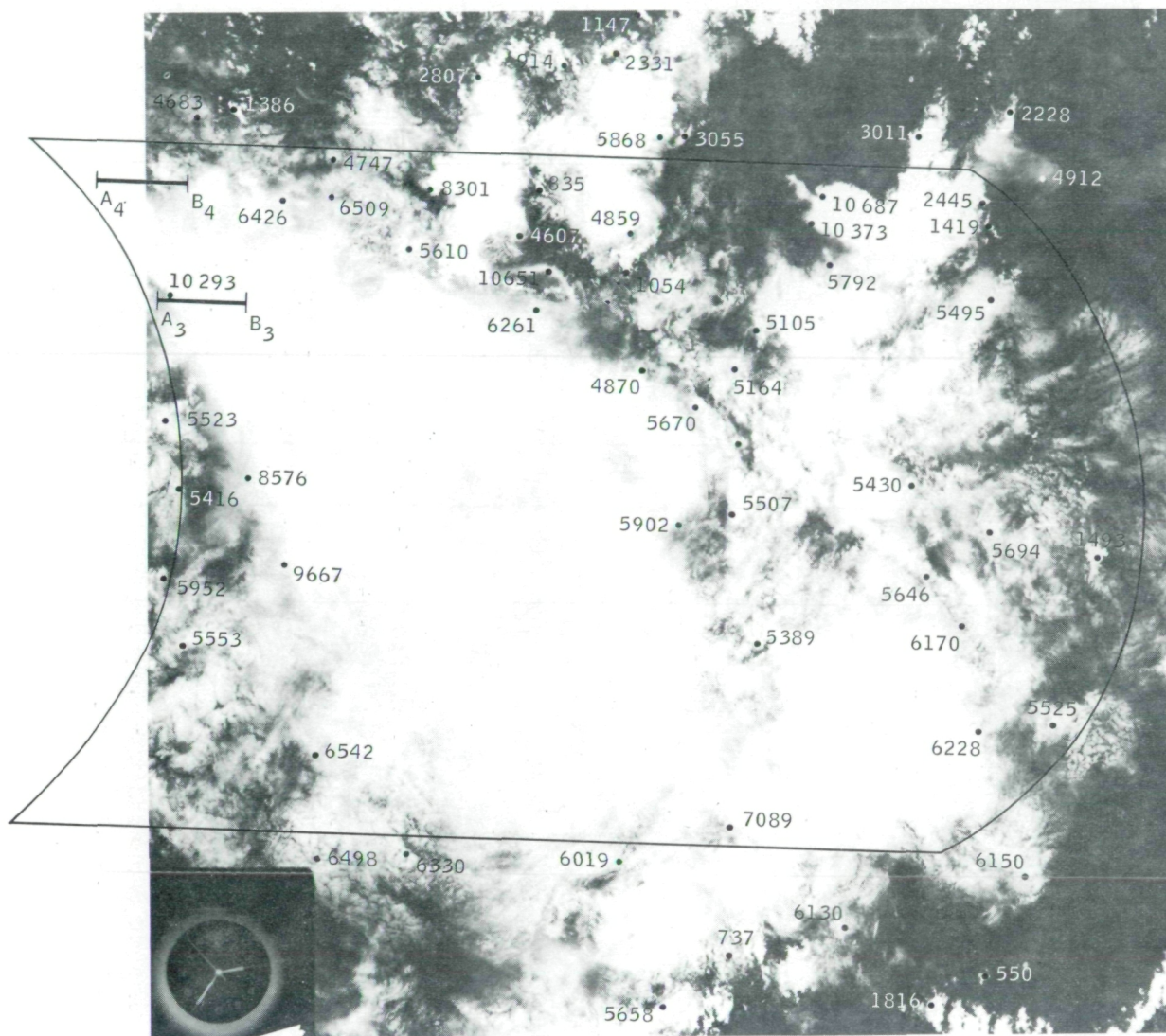
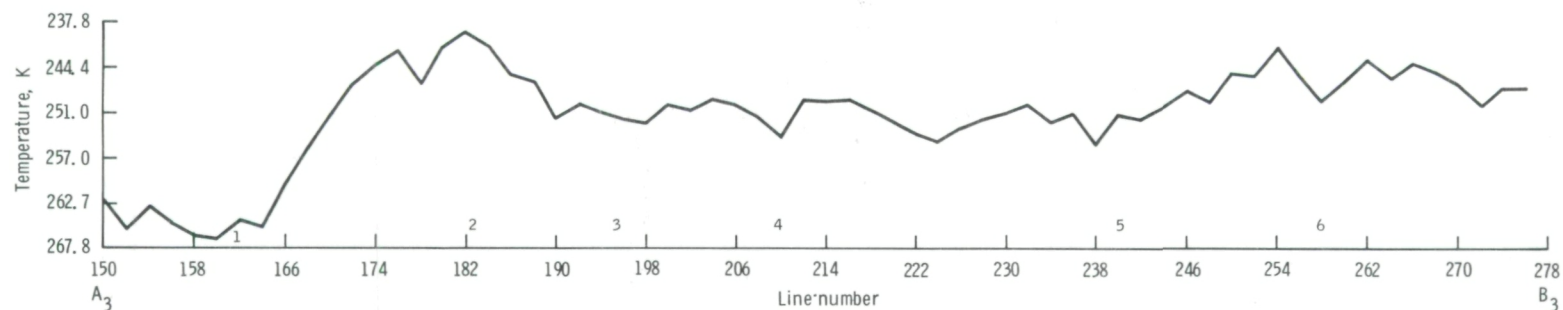
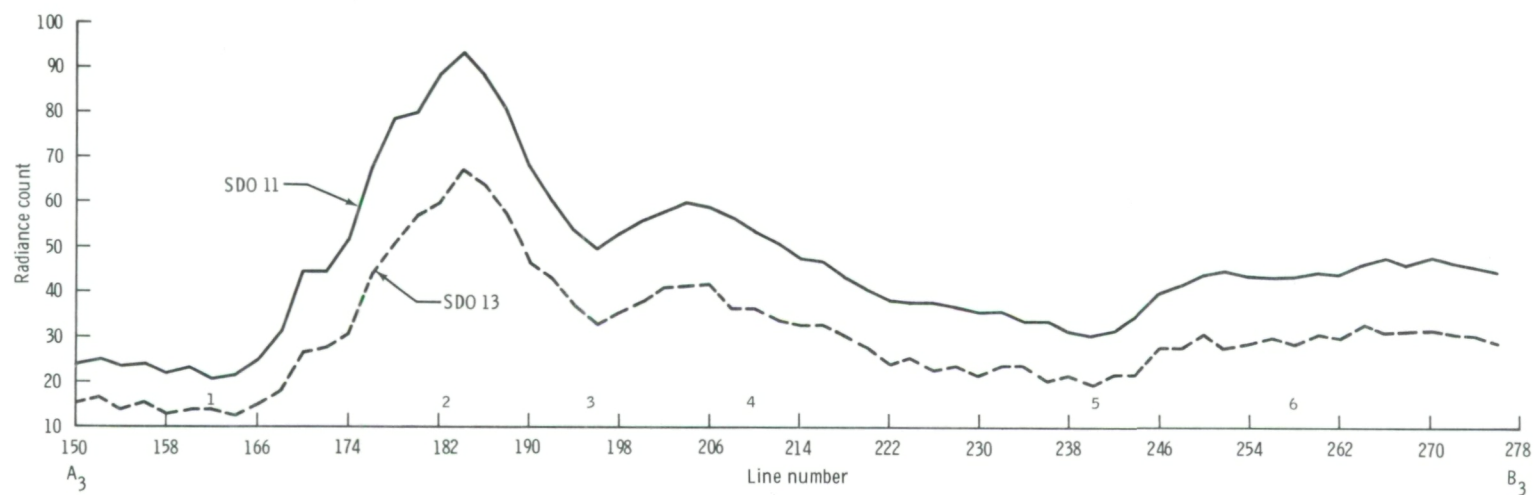


Figure 9-15.- S190B photograph of Borneo thunderstorm on December 9, 1973 (SL4-91-233). Cloud-top altitudes are shown in meters. The S192 coverage is denoted by the outline. Transects 3 and 4 are shown.

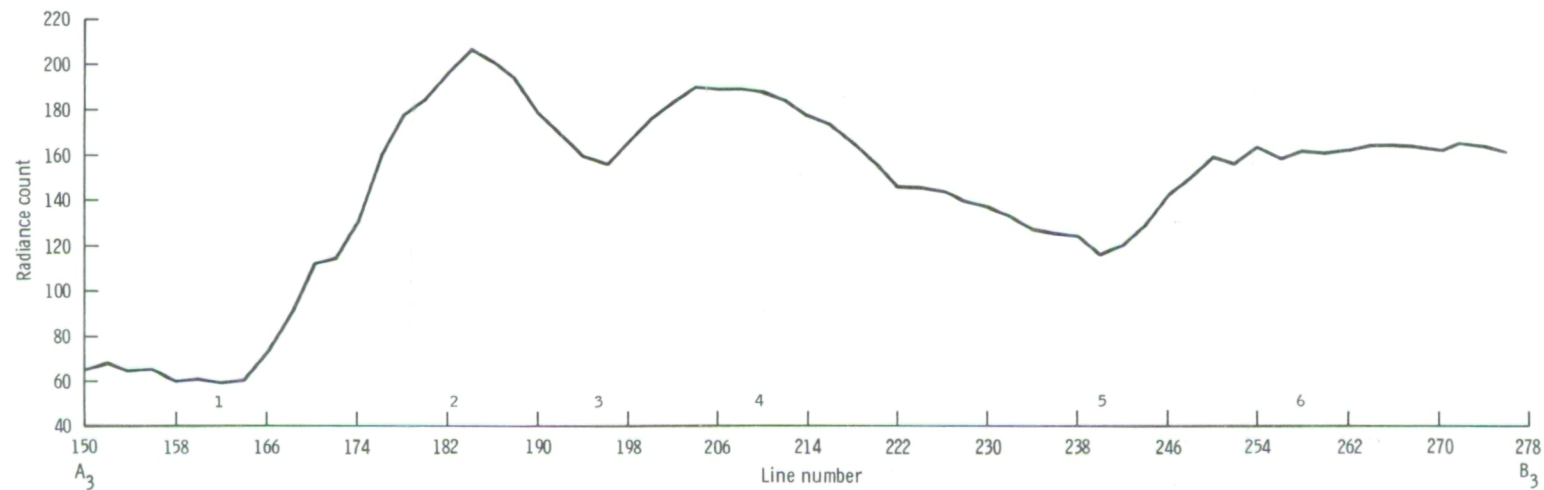


(a) SDO 21.

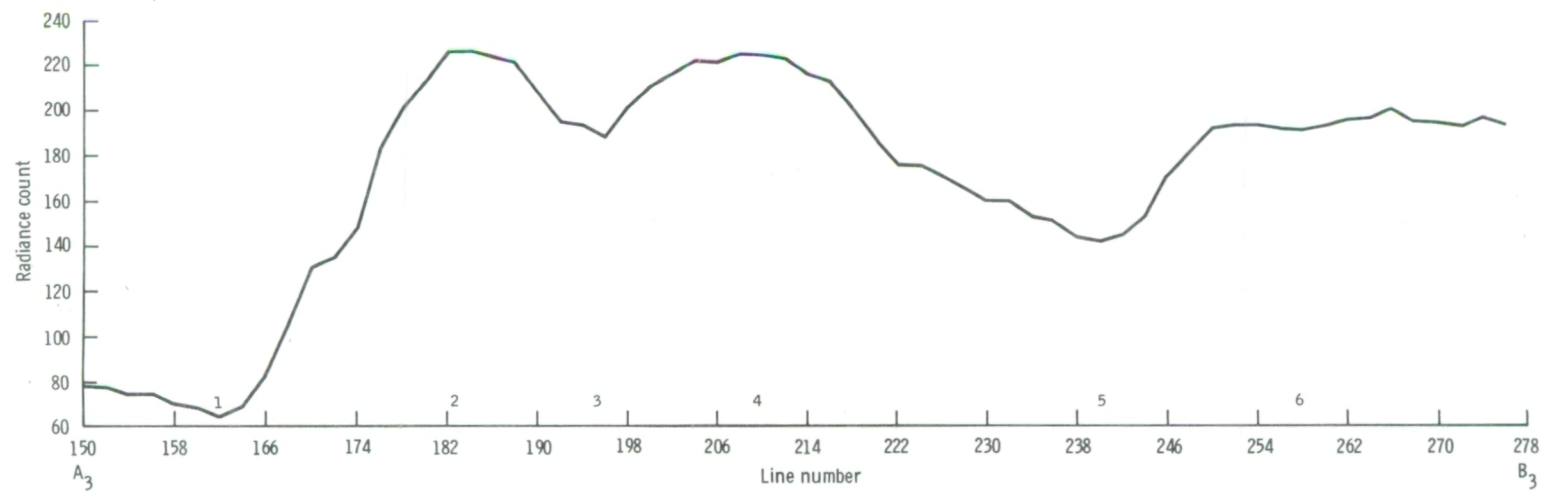


(b) SDO's 11 and 13.

Figure 9-16.- Plot of transect 3 radiance counts for the December 9, 1973,
Borneo thunderstorm.

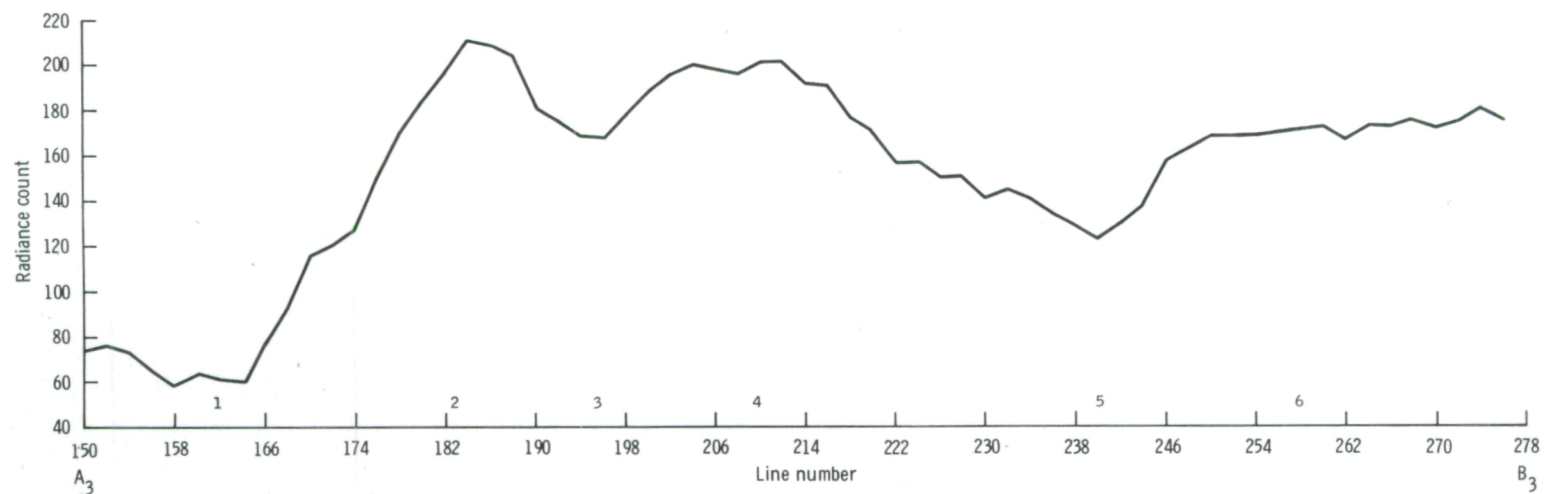


(c) SDO 17.

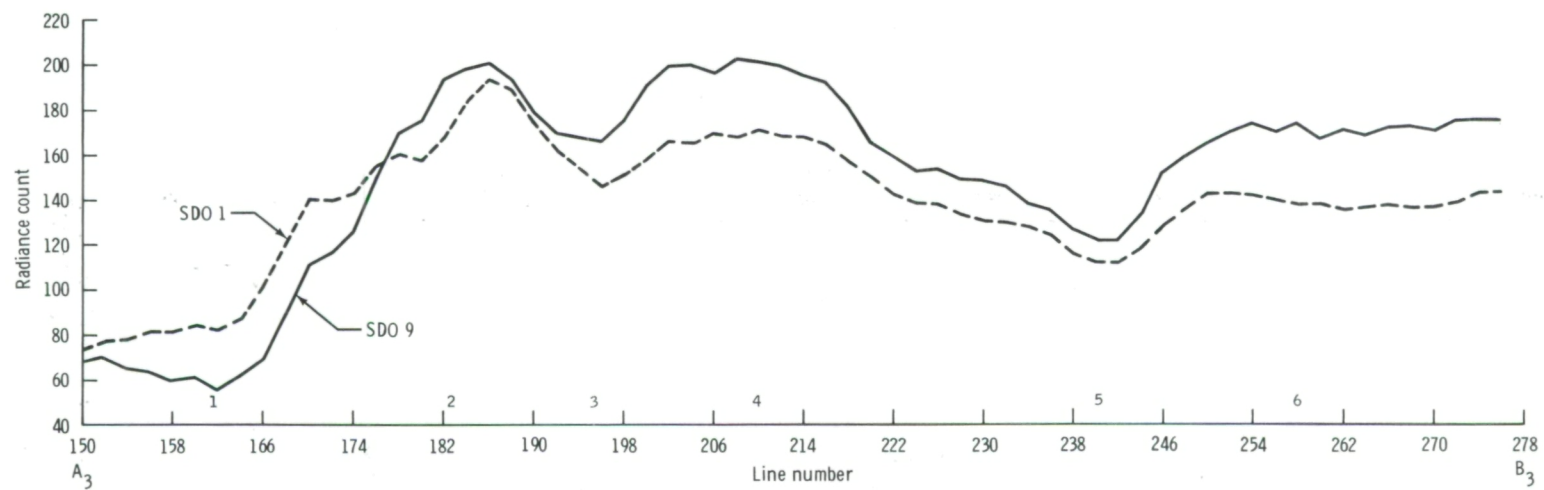


(d) SDO 20.

Figure 9-16.- Continued.



(e) SDO 19.



(f) SDO's 1 and 9.

Figure 9-16.- Concluded.

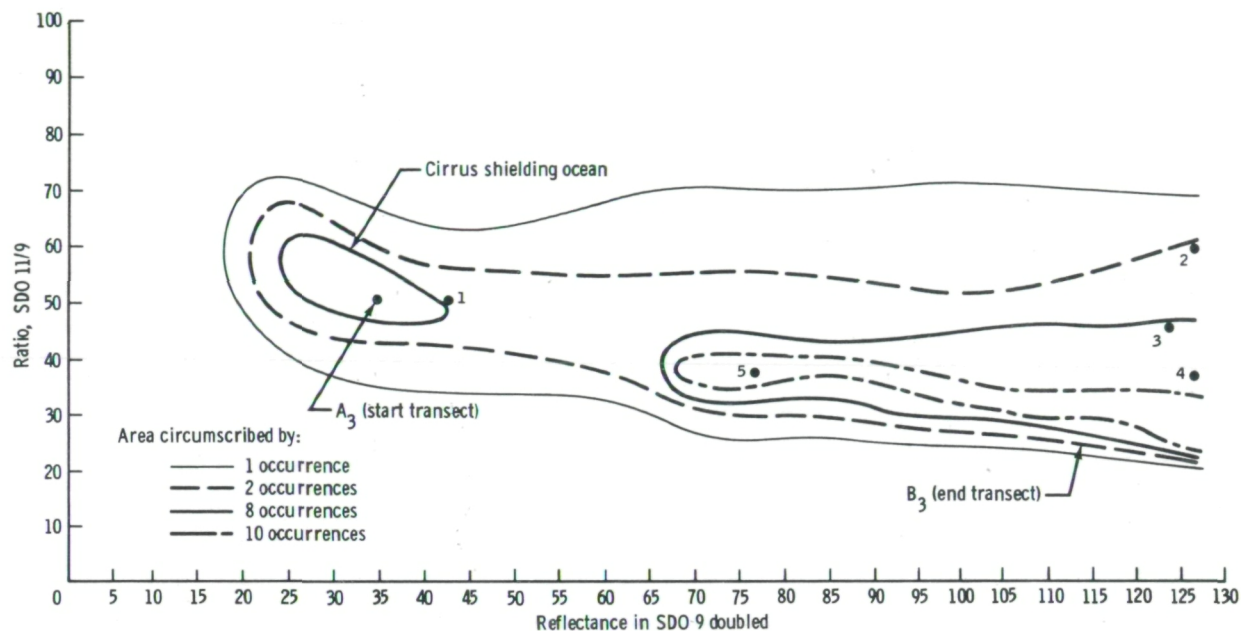


Figure 9-17.- Histogram of transect 3 for the December 9, 1973, Borneo thunderstorm, comparing the ratio of SDO 11/9 to the reflectance in SDO 9 doubled. The numbered points refer to the points marked on the abscissa scale of figure 9-16.

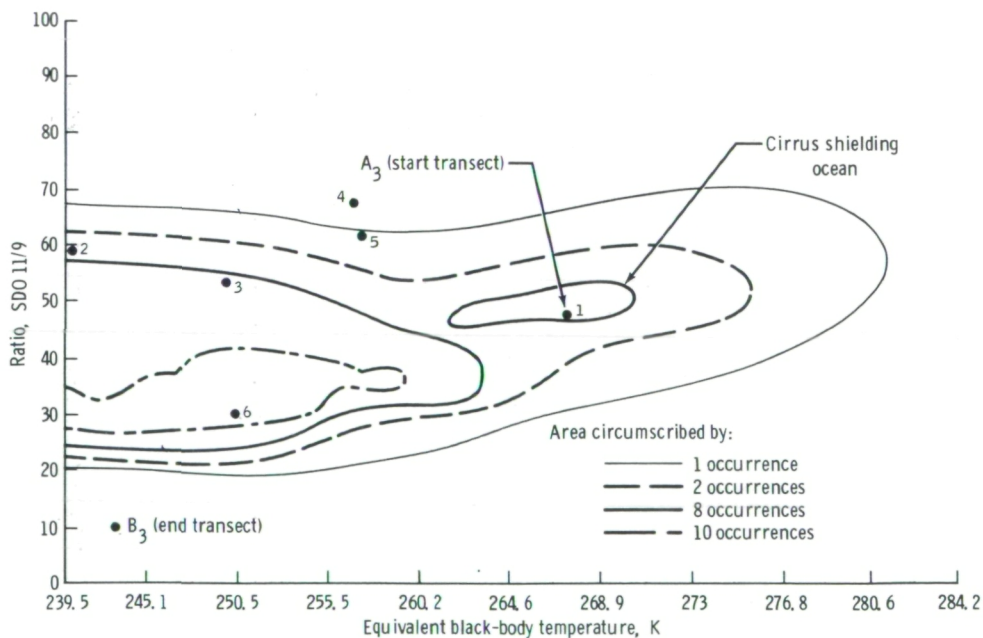
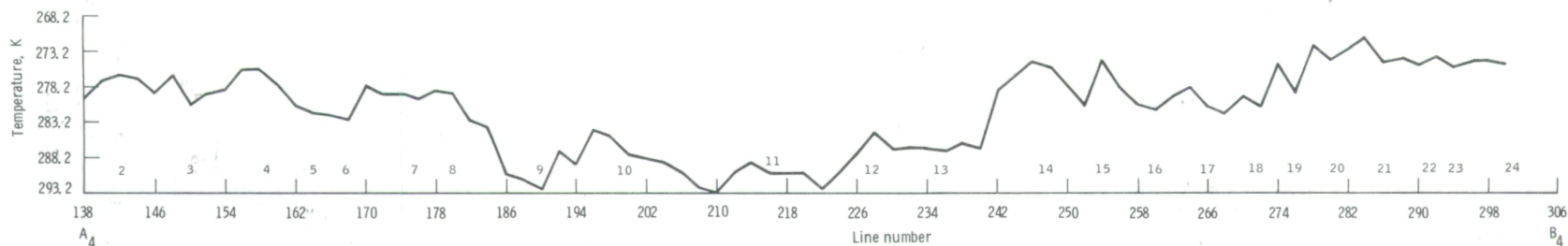
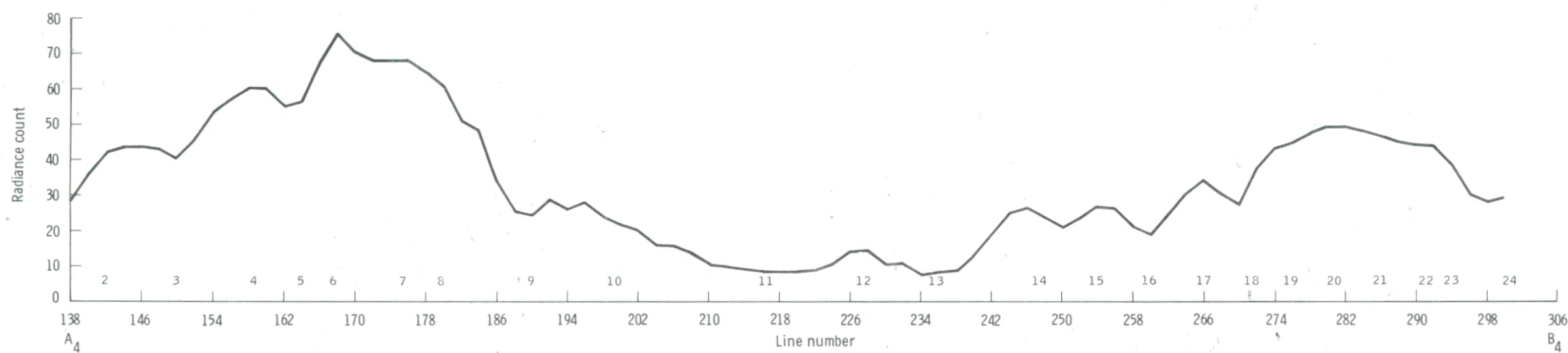


Figure 9-18.- Histogram of transect 3 for the December 9, 1973, Borneo thunderstorm, comparing the SDO 11/9 ratio to the equivalent black-body temperature. The numbered points refer to the points marked on the abscissa scale of figure 9-16.

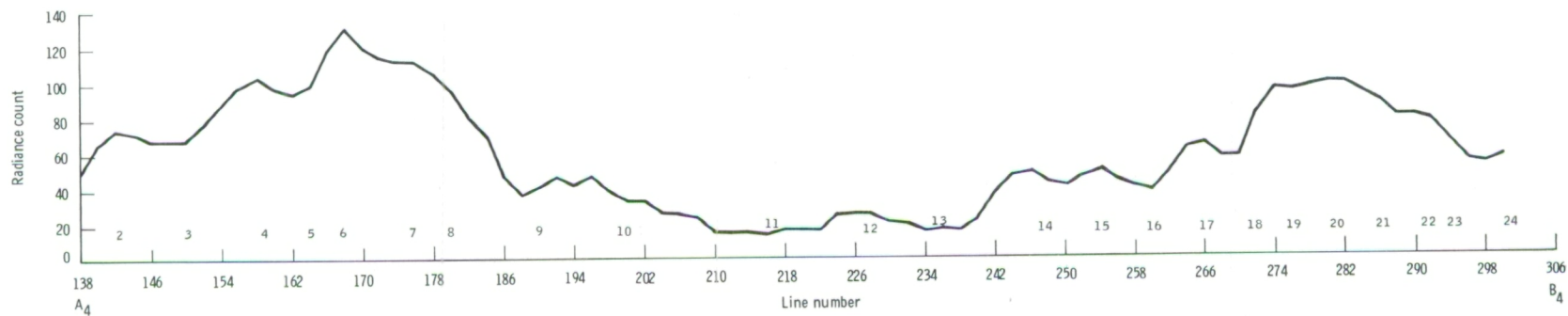


(a) SDO 21.

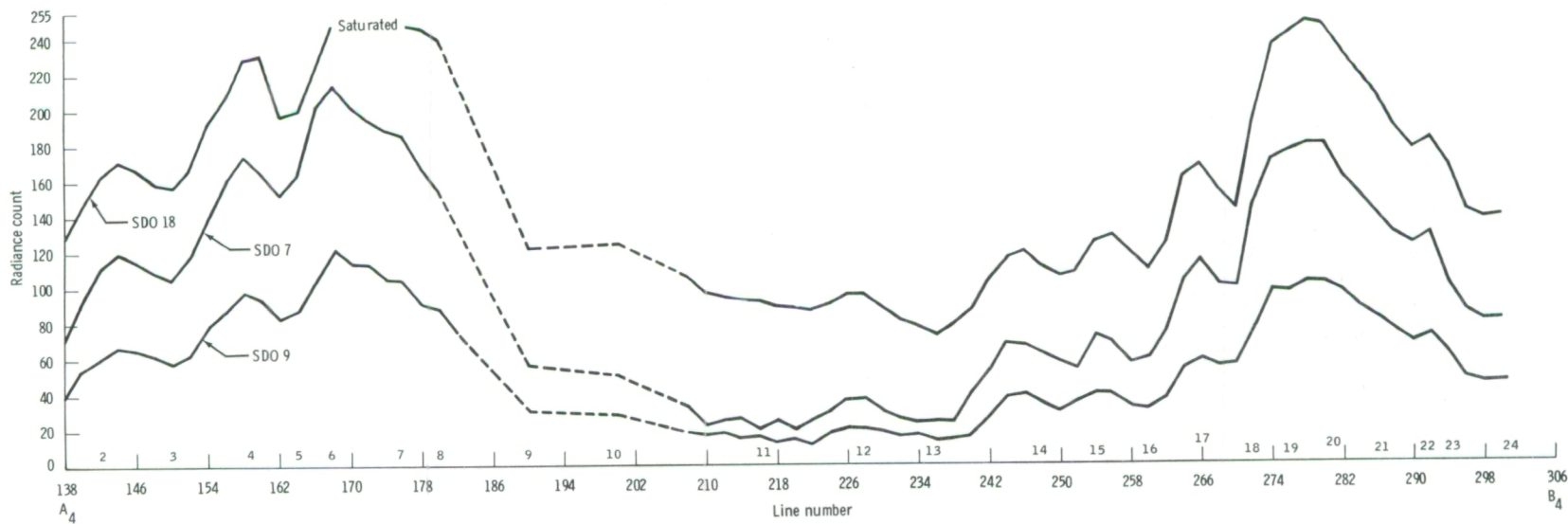


(b) SDO 11.

Figure 9-19.- Plot of transect 4 radiance counts for the December 9, 1973,
Borneo thunderstorm.



(c) SDO 17.



(d) SDO's 7, 9, and 18.

Figure 9-19.- Concluded.

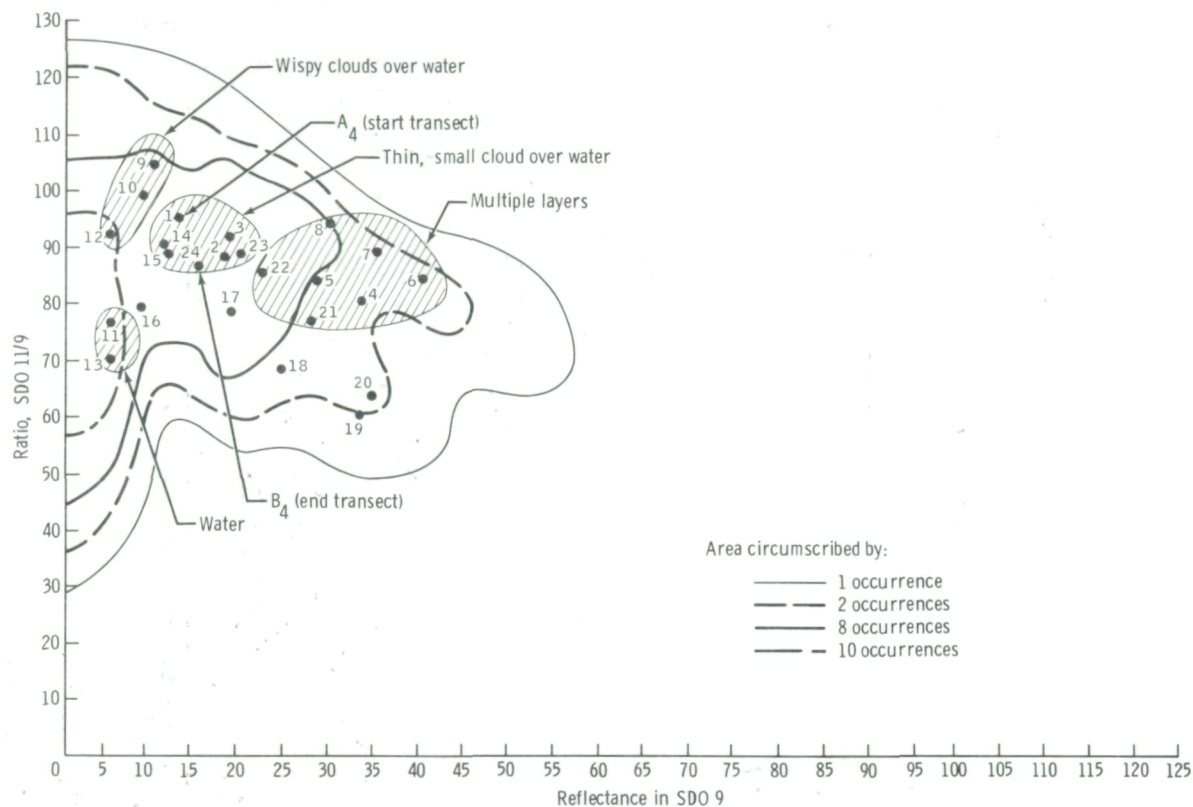


Figure 9-20.- Histogram of transect 4 for the December 9, 1973, Borneo thunderstorm, comparing the ratio of SDO 11/9 to the reflectance in SDO 9. The numbered points refer to the points marked on the abscissa scale of figure 9-19.

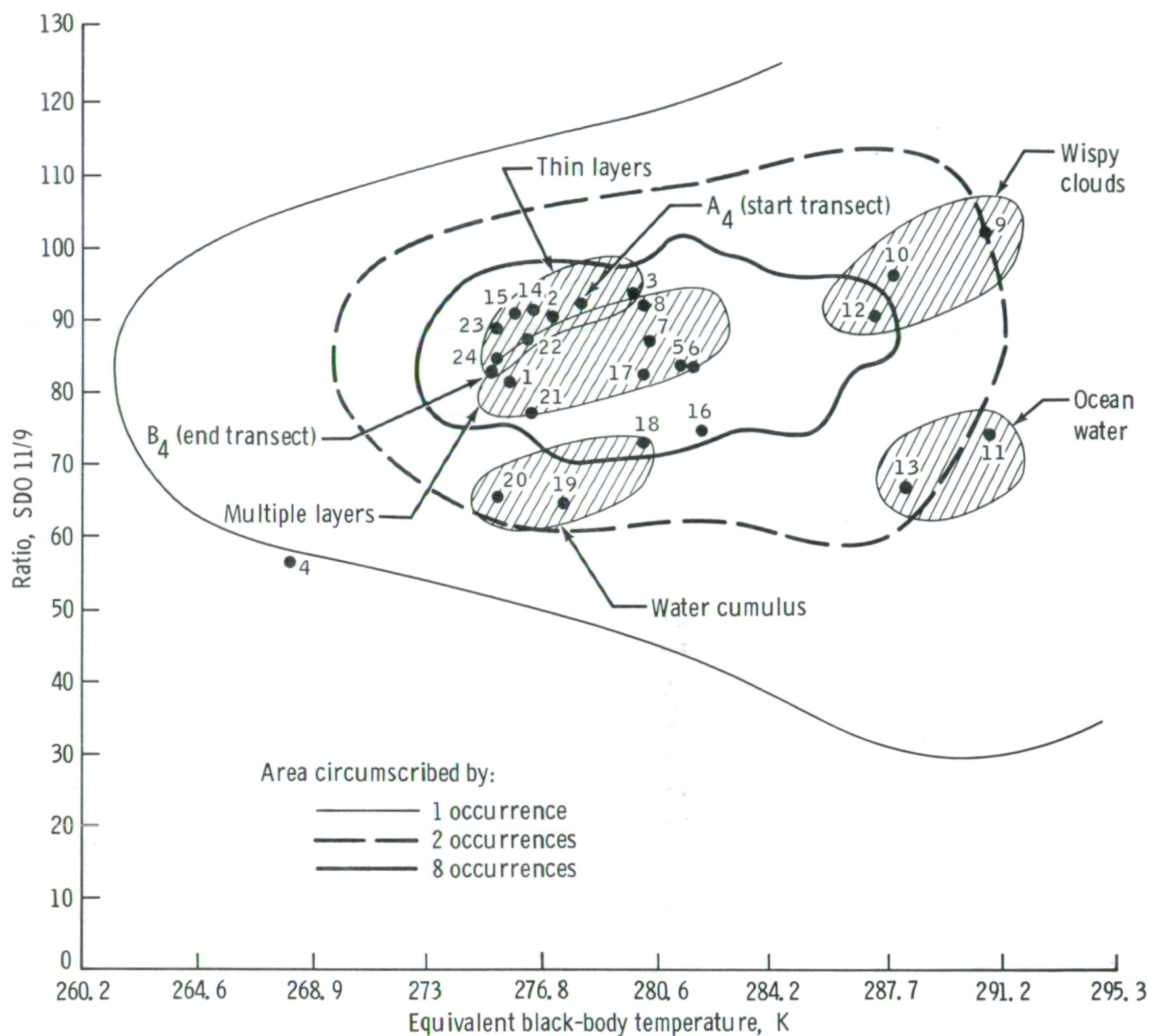


Figure 9-21.- Histogram of transect 4 for the December 9, 1973, Borneo thunderstorm, comparing the SDO 11/9 ratio to the equivalent black-body temperature. The numbered points refer to the points on the abscissa scale of figure 9-19.

10. REMOTE SENSING OF ATMOSPHERIC WATER VAPOR

David E. Pitts,^a J. T. Lee,^b and W. Johnson^c

Data collected by the Skylab Earth resources experiments package (EREP) on the June 11, 1973, pass were studied to determine if atmospheric water vapor could be identified by satellite remote sensing. Both the S192 multispectral scanner and the S191 spectrometer were used.

S192 ANALYSIS

Figure 10-1 shows the S192 imagery for the June 11, 1973, EREP pass over Oklahoma and Texas.¹ This composite image has not been corrected (i.e., data not line straightened) and, therefore, some distortion is evident in the scene due to the conical scan of the S192. The image was made by assigning sensor data output (SDO) 19 (0.88 to 1.09 micrometers) to the red gun, SDO 20 (1.0 to 1.24 micrometers) to the green gun, and the inverse of SDO 21 (9.7 to 13 micrometers) thermal channel to the blue gun of the screening and filming equipment on the Earth Observations Division data analysis station at the Lyndon B. Johnson Space Center (JSC). All parts of the image were generated with the statistics from the area bounded by lines 60 to 66 (used to set the gain and bias) to allow comparison from one area to another. With this arrangement the colors in the image can be interpreted as follows:

<u>Color</u>	<u>Meaning</u>
Blue	Cold, low SDO 19, low SDO 20
White	Cold, high SDO 19, high SDO 20
Red	Warm, high SDO 19, low SDO 20
Yellow	Warm, equal SDO 19, SDO 20
Green	Warm, low SDO 19, high SDO 20
Purple	Cold, high SDO 19, low SDO 20

^aNASA Lyndon B. Johnson Space Center, Houston, Tex.

^bNational Severe Storms Laboratory, Norman, Okla.

^cLockheed Electronics Company, Houston, Tex.

¹EREP pass 8 started at latitude 36°52'10.6" N, longitude 102°18'38.63" W and ended at latitude 32°47'36.24" N, longitude 96°32'11.84" W.

Water vapor has strong absorption lines at 0.9419 and 1.135 micrometers, which can decrease the intensity of SDO 19 and SDO 20. The true response of the S192 was a function of the alinement of the optics as adjusted by the Skylab crew before each EREP pass. Because SDO 20 always appears lower in intensity than SDO 19 (i.e., no green in the image), the investigators believe that the bandpasses were shifted so as to cause SDO 19 to be less affected by the water vapor than SDO 20. This appears corroborated by the image in figure 10-1. The Earth surface is red and the cumulus clouds are yellow, thus indicating less water vapor above the clouds.

The land surface of the panhandle of Texas (lines 1 to 7) should appear more yellow because about 2.25 centimeters precipitable water exists in the area, and the land surface near Dallas-Forth Worth (lines 48 to 60) should have a more red appearance, due to more water vapor in the atmosphere (4.5 centimeters). These precipitable water amounts were derived from the average of the 7 a.m. central daylight time (c.d.t.) and 7 p.m. c.d.t. radiosonde soundings from Amarillo and Greater Southwest Airport, respectively. A sounding taken at 10:17 a.m. c.d.t. at Fort Sill was almost coincidental with the Skylab overpass time of 10:18 a.m. c.d.t. and was 35 kilometers northeast of the center of the groundtrack (line 30 in fig. 10-1), and gave 3.05 centimeters precipitable water. Indeed it does appear that the area of lines 1 to 7 is more yellow in appearance than the area around line 60. However, some of the change results from changing background reflectance and not water vapor changes. Because the statistics were taken over an area with clouds, and with large amounts of water vapor, the gain on the green gun was set very low in order to keep the high green intensity over the clouds and the low green intensity over the land surface on scale. Therefore some of the difference in the water channel is masked (or compressed). Field patterns are evident in the image; therefore, it is apparent that some variations from red to yellow are caused by differences in reflectance between SDO 19 and SDO 20, which are in turn caused by differences in land use.

Stucky (section 8) determined that the cumulus cloud bases were at 335 meters over Lake Altus (between lines 19 and 20). This agrees well with using cloud shadows to determine the altitude of the cloud tops. According to the Fort Sill sounding, there is about 0.58 centimeter of water vapor between the surface and 360 meters. Thus, the yellow color on the cumulus clouds represents about 2.15 centimeters of water vapor. This is less than the lowest amount measured over Amarillo, corroborating that the area of lines 1 to 7 would not appear as yellow as the cumulus clouds. The reflectance of the cirrus clouds (ice crystals) is low in the near-infrared wavelengths, thus causing them to appear blue in figure 10-1. Clouds composed of liquid water droplets have higher reflectance in the near-infrared wavelengths and, therefore, appear white. This color would then be indicative of an active growing cell, whereas either cirrus, mature thunderstorms, or decaying thunderstorms would appear blue. Thus, white could be used as a key for thunderstorms that might produce tornadoes, and blue would indicate thunderstorms less likely to produce tornadoes.

Both Lake Altus (lines 19 and 20) and Little Elm Reservoir (at line 60) show traces of the blue indicator of cirrus. It is more apparent over the lakes than over the land, because the low reflectance in the near-infrared region in SDO 19 and SDO 20 causes the red and green intensity to be very low.

The area of the tape between lines 67 and 68 (fig. 10-1) has been used to construct a two-dimensional histogram, which is shown in figure 10-2. The ratio of SDO 20 and SDO 19 was used on the ordinate axis and SDO 21 counts, which are related to equivalent black-body temperature, were used on the abscissa. The contours represent the number of occurrences of each pair of ordinate and abscissa values. Pitts et al. (ref. 10-1) have shown that precipitable water P can be expressed as a function of the ratio of a water vapor channel and a nearby clear channel:

$$P = \frac{\left[-\frac{1}{K} \ln \left(\frac{I_{\text{SDO 20}}}{I_{\text{SDO 19}}} c \right) \right]^{\frac{1}{x}}}{\sec \theta_S + \sec \theta_L} \quad (10-1)$$

where c , $-\frac{1}{K}$, and $\frac{1}{x}$ are constants

I = radiance in $\frac{W}{cm^2 \cdot \mu m \cdot sr}$

θ_S = solar zenith angle = 43.91° for June 11

θ_L = angle off vertical for S192 conical scanner = 5.5°

The Fort Sill radiosonde for 10:17 a.m. c.d.t. used with the preceding equation (assuming $x = 1/2$ (ref. 10-2), $c = 1$, and $K = 0.2$) gives the radiosonde profile shown in figure 10-2, assuming that a cloud has an equivalent black-body temperature very nearly the same as its environment. The variance of the cold targets (i.e., high clouds) appears lower than the warm targets (low clouds and Earth surface).

When images of the ratio (SDO 20/SDO 19) were constructed, it was found that the east side of the image (looking into the solar vector) consistently had about 10 percent higher values than the southwest side (looking across the solar vector). All targets - clouds, cloud shadows, and Earth surface - exhibited this characteristic, so it is unlikely that anisotropic reflections of soils and rocks are the cause. Therefore the scanner is thought to have a scan angle effect in both channels that is small when the channels are analyzed separately but has a covariance so that the ratio amplifies the effect. Thus, in figure 10-2 the high values of the ratio originate from the east side of the image and the low values originate from the southwest side of the image. The most probable reason for the lower variance of the ratio at temperatures colder than 282 K is that the high clouds occur in only one part of the scene. This scan angle effect is not apparent for S192 data from August 8 or other days.

analyzed. No scan angle effect was reported in the data quality analysis performed at JSC².

S191 ANALYSIS

In order to assess whether ratioing two channels (one over a water vapor channel and one over a clear band) could allow the determination of water vapor (precipitable water), the 0.94-micrometer water band and the 1.0-micrometer clear band of S191 were calibrated. Calculations of atmospheric transmission were made using compressed water vapor lines and a 10-layer atmospheric transmission model (ref. 10-3) over the range of 0.91 to 0.97 micrometer. These data were integrated and normalized with the response function R_λ for S191, which is

$$R_\lambda \approx \exp\left[-5.0 \times 10^3 (\lambda - 0.94)^2\right]$$

where λ = wavelength in micrometers

$$\bar{T} = \frac{\int_{0.91\mu\text{m}}^{0.97\mu\text{m}} R_\lambda I_\lambda T_\lambda d\lambda}{\int_{0.91\mu\text{m}}^{0.97\mu\text{m}} R_\lambda I_\lambda d\lambda} \quad (10-2)$$

where I_λ = solar intensity

T_λ = atmospheric transmission function

\bar{T} = average transmission for the 0.94-micrometer water vapor band

The average transmission \bar{T} was calculated for a variety of atmospheric conditions by using actual radiosonde data (ref. 10-4) that represent extreme

²Engvall, John, EREP S192 Data Quality Monitoring Report for June 11, 1973 (REPT 159-02-08, January 23, 1975).

conditions in water vapor, temperature, and pressure during 1 year in the contiguous United States. These data are

<u>Precipitable water Pm, cm</u>	<u>\bar{T}</u>
10.28	0.2497
5.851	0.3501
4.790	0.3909
3.377	0.4685
1.278	0.6024
0.131	0.8061

These data are well represented by the curve fit

$$\bar{T} \approx \exp \left[-k (Pm)^x \right]$$

where, for this case, $x = 0.5568$ and $k = 0.3938$. It is assumed that the ratio of intensity (I) measured by SI91 at the two wavelengths times a constant is a measure of \bar{T} (ref. 10-3)

$$\bar{T} = \frac{c \frac{I_{0.94 \mu m}}{I_{1.0 \mu m}}}{I_{1.0 \mu m}}$$

Thus, giving a measure of total water vapor in the Sun-target-spacecraft path

$$Pm = \left[\frac{-1}{k} \ln \left(\frac{I_{0.94} c}{I_{1.0}} \right) \right]^{\frac{1}{x}} \quad (10-3)$$

If the solar zenith angle θ_S and the zenith look angle θ_L are considered, with the curvature of the Earth being neglected, the total distance transversed relative to the vertical single path distance is

$$\frac{Z \sec \theta_S + Z \sec \theta_L}{Z}$$

where Z is the vertical distance. Therefore, the airmass m is $m = \sec \theta_S + \sec \theta_L$ and the precipitable water is

$$P = \frac{\left[\frac{-1}{k} \ln \left(\frac{I_{.94} c}{I_{1.0}} \right) \right]^{\frac{1}{x}}}{\sec \theta_S + \sec \theta_L}$$

Assuming that the water reflectance and incident solar intensity are the same at both wavelengths, then $c = 1$ and the precipitable water over Lake Thunderbird is calculated to be 0.97 ± 0.35 centimeters, whereas the radiosonde from Norman, Oklahoma, only a few kilometers away, at the same local time gave 2.58 centimeters.

If the data are normalized by $c = 0.61$, one gets 2.71 ± 0.55 centimeters, which agrees well with the radiosonde-derived value. With this procedure, the other targets in central Oklahoma gave the following results. (The confidence limits are ± 1 standard deviation.) The locale is shown in figure 10-3.

<u>Target</u>	<u>P, cm</u>	<u>No. of data</u>
Lake Thunderbird	2.71 ± 0.55	14
Fort Cobb Reservoir	3.20 ± 0.36	14
Lake Overholzer	3.24 ± 0.33	9
Lake Hefner	2.71 ± 0.24	10
Agricultural fields (Bailey turnpike and South Canadian River)	3.58 ± 0.20	10
Norman, Okla., radiosonde (10:17 a.m. c.d.t.)	2.58	

Tests were also conducted using this technique for the August 8, 1977, pass over a thunderstorm over the Gulf of Mexico. Unfortunately, the S191 data for this day were provided at different wavelengths than for the June 11 case, 0.945 and 0.99 micrometer, and this difference prevented using this as an independent test of constants derived using the June 11 data. Setting $c = 0.42$ for these new wavelengths gave

<u>Target</u>	<u>P, cm</u>	<u>No. of data</u>
Fields between cumulus	4.51 ± 0.32	8
Cumulonimbus tops (14 km)	1.20 ± 0.46	6

These numbers compare favorably with the precipitable water from the 1 a.m. c.d.t. soundings from Lake Charles, Louisiana, and Victoria, Texas, 4.93 and 4.69 centimeters, respectively.

These data were taken at various angles ranging from 9° left to 5° right and from 9° forward to 26° aft of the spacecraft. No evidence of anisotropic reflections from the Earth surface was noted.

REFERENCES

- 10-1. Pitts, D. E.; Dillinger, Alyce E.; and McAllum, William E.: Measurement of Atmospheric Precipitable Water Using a Solar Radiometer. NASA TM X-58129, 1974.
- 10-2. Gates, David M.; and Harrop, Walter J.: Infrared Transmission of the Atmosphere to Solar Radiation. App. Optics, vol. 2, no. 9, Sept. 1963, pp. 887-898.
- 10-3. Pitts, D. E.; Barnett, T. L.; et al.: Atmospheric Transmission Computer Program CP. NASA TM X-58137, 1974.
- 10-4. Jeske, K. W.: Extreme Atmosphere Models, 1973, Based on Radiosonde Data. NASA TM X-58112, 1974.

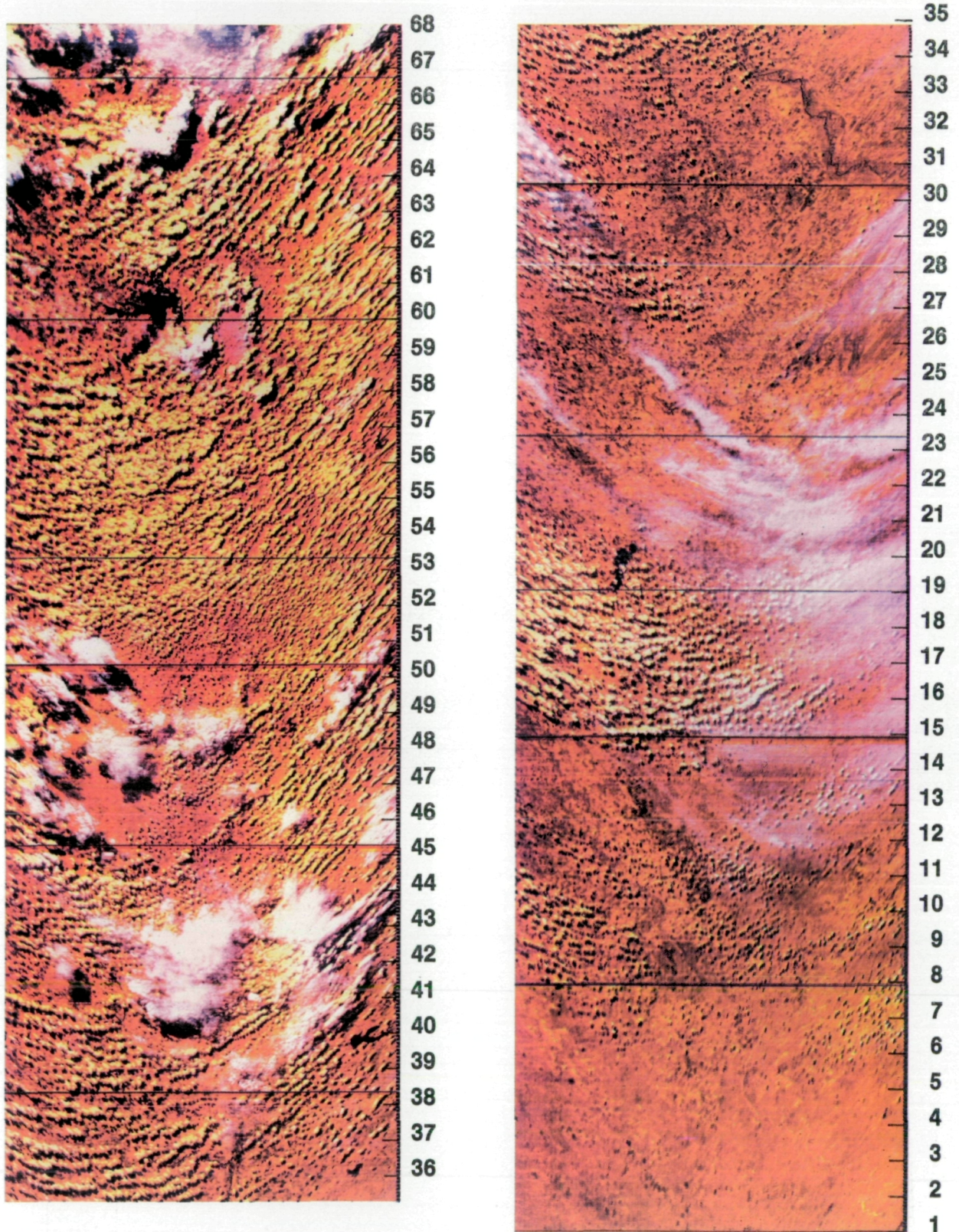


Figure 10-1.- Composite image of the June 11, 1973, pass over Oklahoma and Texas. Scan lines are shown on the right.

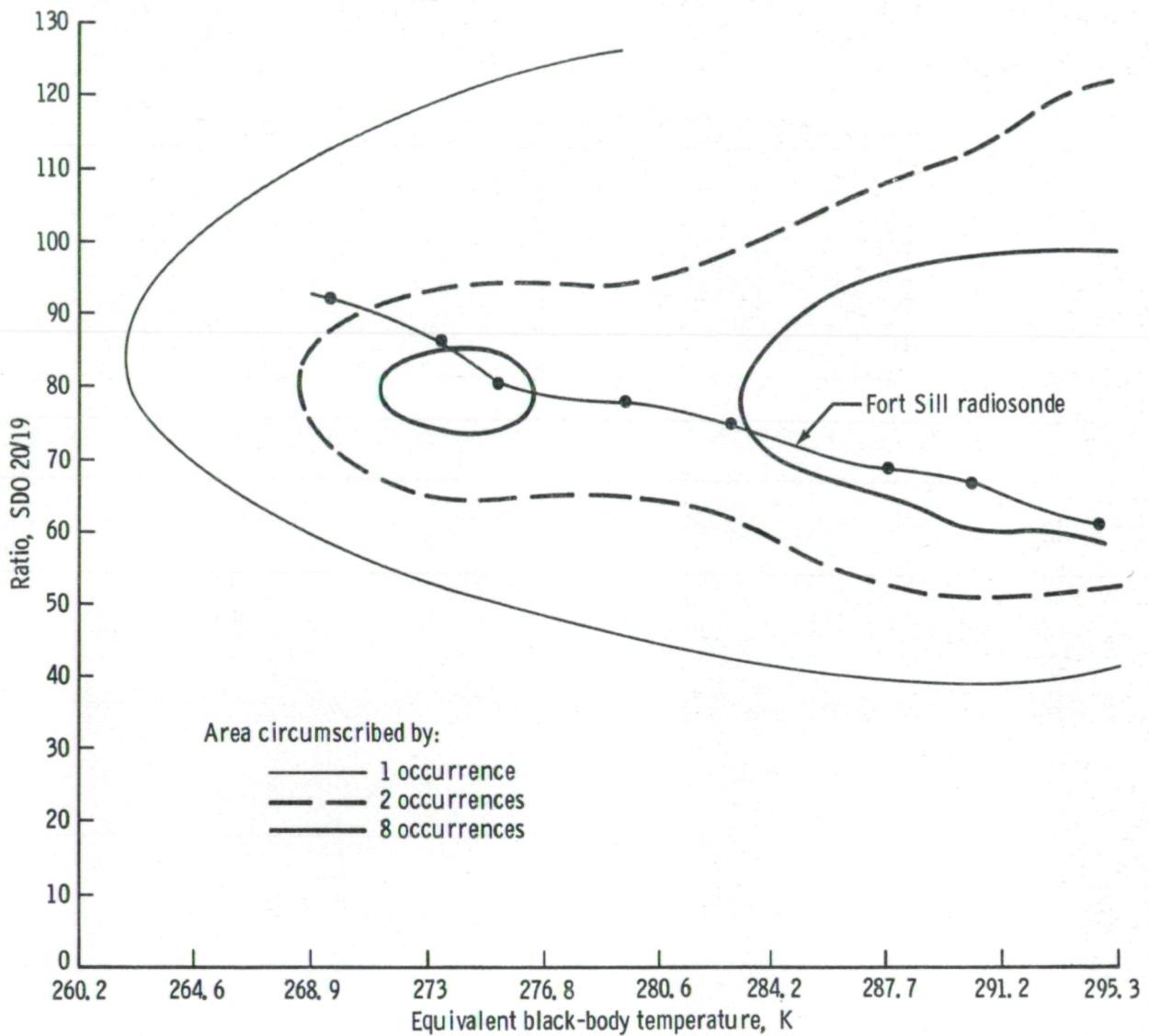


Figure 10-2.- Histogram of the June 11, 1973, S192 data over the area between lines 67 and 68 in figure 10-1.

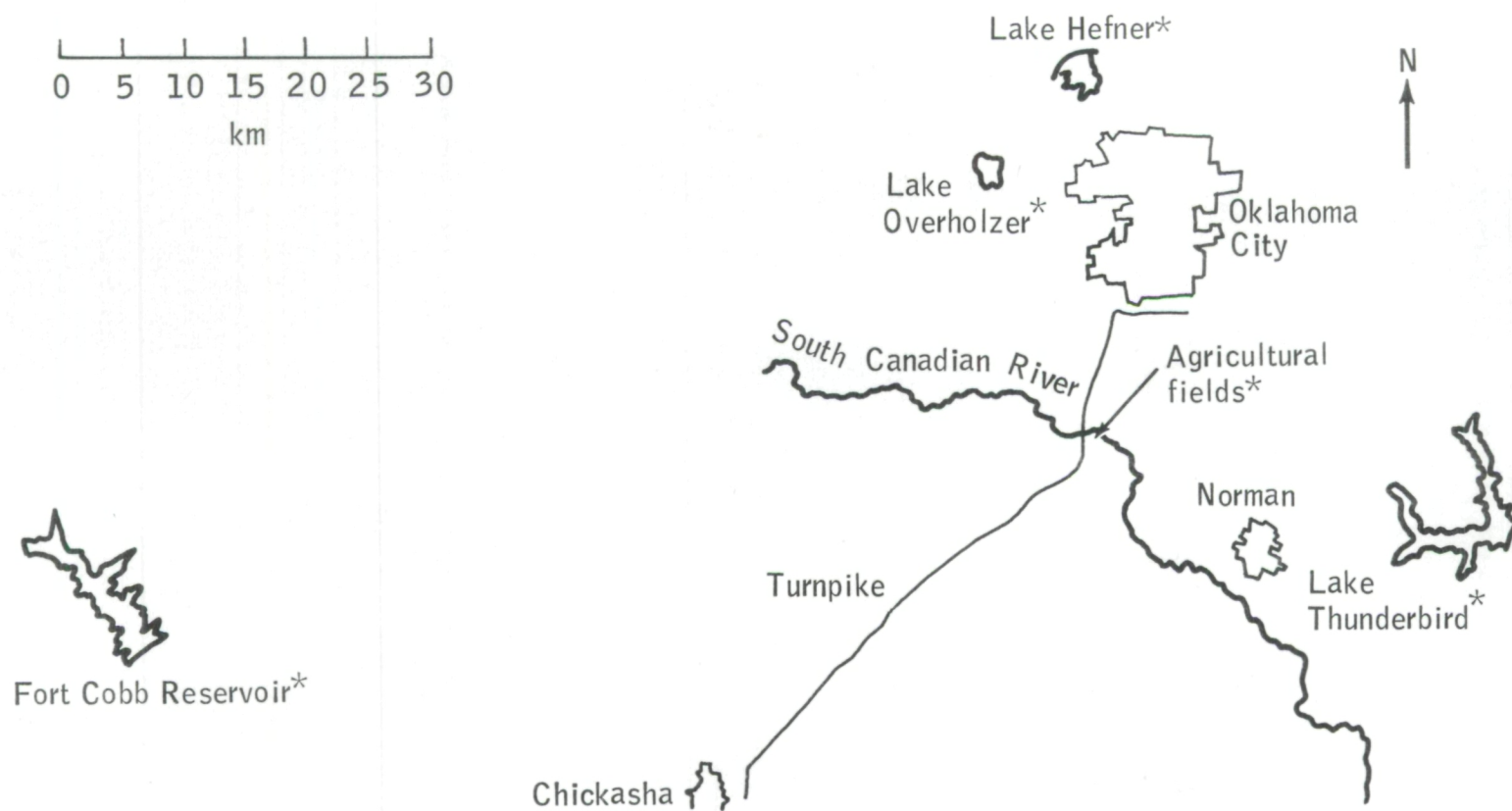


Figure 10-3.- Geographical area of S191 analysis in central Oklahoma. The points marked with asterisks are test sites.

1. Report No. NASA TM 58184		2. Government Accession No.		3. Recipient's Catalog No.	
4. Title and Subtitle SEVERE STORM ENVIRONMENTS A SKYLAB EREP FINAL REPORT				5. Report Date August 1978	
				6. Performing Organization Code JSC-11094	
7. Author(s) David E. Pitts, JSC, Yoshikazu Sasaki, University of Oklahoma, and J. T. Lee, National Severe Storms Laboratory, Compilers				8. Performing Organization Report No.	
9. Performing Organization Name and Address Lyndon B. Johnson Space Center Houston, Texas 77058				10. Work Unit No. 658-89-00-00-72	
				11. Contract or Grant No.	
12. Sponsoring Agency Name and Address National Aeronautics and Space Administration Washington, D.C. 20546				13. Type of Report and Period Covered Technical Memorandum	
				14. Sponsoring Agency Code	
15. Supplementary Notes					
16. Abstract A final report is given on the severe storm environments experiment that used the Skylab Earth resources experiments package. Investigators discuss their findings relative to derived water temperatures, temperature and water vapor profiles, soil moisture measurements, severe storm cloud-top characteristics, and the use of whole-sky photographs for positioning clouds. An overall description and results of the experiment are included.					
17. Key Words (Suggested by Author(s)) Earth resources Radiometers Cloud cover Soil moisture Storms (meteorology) Brightness Meteorology temperature Weather forecasting Multispectral band scanners				18. Distribution Statement STAR Subject Category: 43 (Earth Resources)	
19. Security Classif. (of this report) Unclassified		20. Security Classif. (of this page) Unclassified		21. No. of Pages 143	
				22. Price* \$6.00	